Supporting Information

Synthesis of Hofmann-based metal-organic frameworks incorporating a bis-pyrazole linker for various gas separations

Brooke L. Matthews,[a,b] Nathan C. Harvey-Reid,*[a,b] Elnaz Jangodaz,[b,c] Victoria-Jayne Scott,[b,c] Matthew I. J. Polson,[a] Ashakiran Maibam,[d,e,f] Ravichandar Babarao,[d,g] Shane G. Telfer,[b,c] and Paul E. Kruger*[a,b]

a. School of Physical and Chemical Sciences, University of Canterbury, Christchurch 8140, New Zealand

b. MacDiarmid Institute for Advanced Materials and Nanotechnology

c. Institute of Fundamental Sciences, Massey University, Palmerston North 4442, New Zealand

d. School of Science, Centre for Advanced Materials, and Industrial Chemistry (CAMIC), RMIT University, Melbourne, VIC, 3001, Australia.

e. Physical and Materials Division, CSIR-National Chemical Laboratory, Pune 411008, India

f. Academy of Scientific and Innovative Research (AcSIR), Ghaziabad 201002, India

g. CSIRO Future Industries-Manufacturing Business Unit, Clayton, VIC, 3169, Australia

Synthesis, Materials and Methods

General

All reagents and solvents used were of reagent grade unless otherwise stated and did not require further purification and only distilled water was used. ^{1}H and ^{13}C NMR measurements were carried out on an Agilent 400 NMR spectrometer operating at 400 MHz for ^{1}H and 101 MHz for ^{13}C. Chemical shift values are given in parts per million (ppm). Infrared measurements were carried out using a Bruker ALPHA Platinum ATR FT-IR spectrometer measuring in the range 4000-450 cm^{-1}. TG analyses were performed on Alphatech SDT-Q600 device with an alumina pan and dinitrogen as balance and sample gas at a temperature increase rate of 10 °C/min. The powder material was finely ground and homogenised.

Ligand Synthesis:

4,4'-methylenebis(3,5-dimethylpyrazole) **(H_2mdp)** was prepared following a literature method.[1]

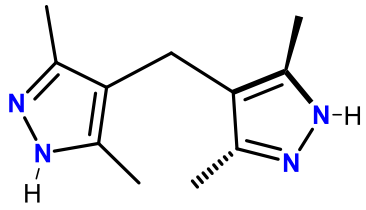

H_2mdp

Single crystal synthesis:

Synthesis of [Co(H_2mdp)(Ni(CN)$_4$)]

A 4 mL water solution of $K_2[Ni(CN)_4]\cdot_n H_2O$ (10 mg, 0.04 mmol) was prepared and carefully transferred test tube of 10 cm length and 1 cm diameter. An 8 mL buffer solution of methanol: H_2O (2:1) was carefully layered above the first solution, creating a defined layer between the two. Finally, a 4 mL methanol solution of H_2mdp (9 mg, 0.04 mmol) and $Co(NO_3)_2\cdot 6H_2O$ (12 mg, 0.04 mmol) was layered on top of the buffer solution creating a third layer. The test-tube was sealed and left to stand. X-ray quality orange plate crystals formed on the sides of the vial after one week.

Synthesis of [Fe(H_2mdp)(Ni(CN)$_4$)]

An identical procedure as above was followed except $Fe(SO_4)_2 \cdot 7H_2O$ (12 mg, 0.04 mmol) was used in place of $Co(NO_3)_2 \cdot 6H_2O$ and layered on top of the buffer solution to create the third layer. The test-tube was sealed and left to stand. X-ray quality yellow plate crystals formed on the sides of the vial after a couple of days.

Bulk micro-crystalline powder synthesis:

Synthesis of [Co(H_2mdp)(Ni(CN)$_4$)]

H_2mdp (45 mg, 0.20 mmol) and $Co(NO_3)_2 \cdot 6H_2O$ (60 mg, 0.20 mmol) were dissolved in 10 mL MeOH and added to a stirring solution of $K_2[Ni(CN)_4] \cdot {}_nH_2O$ was dissolved in 5 mL H_2O, yielding a pale pink powder. The reaction mixture was stirred an additional 3 hours at room temperature, and then left to settle. The solvent was decanted and replaced with fresh methanol several times over a period of three days prior to isolation through filtration and further characterisation.

Synthesis of [Fe(H_2mdp)(Ni(CN)$_4$)]

Synthesis of **[Fe(H_2mdp)(Ni(CN)$_4$)]** followed the same procedure as **[Co(H_2mdp)(Ni(CN)$_4$)]**, except that $Fe(SO_4)_2 \cdot 7H_2O$ (58 mg, 0.20 mmol) was used instead of $Co(NO_3)_2 \cdot 6H_2O$, yielding a pale-yellow powder.

X-ray diffraction

Single crystal X-ray diffraction for **[Co(H_2mdp)(Ni(CN)$_4$)]** and **[Fe(H_2mdp)(Ni(CN)$_4$)]** was carried out on an Agilent Supernova with an Atlas CCD area detector using graphite-monochromatized Cu-Kα (λ = 1.54184 Å) radiation at 120 K (see Table S1).

Data indexing and reduction were conducted using CrysAlisPro software. Structures were solved using Intrinsic Phasing with SHELXS[2] and refined using Least Squares minimisation procedures with SHELXL[3] within the program OLEX-2.[4] All non-hydrogen atoms on the frameworks were refined anisotropically. Graphical representations of crystallographic data were prepared using the OLEX-2 and Mercury software packages.

Powder X-ray diffraction (PXRD) analysis for **[Co(H_2mdp)(Ni(CN)$_4$)]** and **[Fe(H_2mdp)(Ni(CN)$_4$)]** was conducted using a Rigaku Smartlab 3 kW diffractometer with a D/teX ID detector at room

temperature. The diffractometer was operated at 40 kV and 30 mA and Cu Kα radiation (λ = 1.540598 Å). A 10 mm length limiting slit, 5° entry and exit Soller slits and a Kβ filter were used. Samples were prepared by grinding crystals into a fine powder and packing on a 20 mm x 20 mm square indent of a glass holder. The height of the sample was aligned to a flat sample of 0 mm thickness and the data was collected from 3°-50° (2θ) with the step size of 0.0168° and a scan time of 10 °/min. The data were analysed using integrated X-ray powder diffraction software (PDXL 2; Version 2.8.1.1). Simulated powder X-ray diffraction pattern was generated from the single crystal data using CCDC Mercury.[5]

Table S1. Single crystal X-ray data for **[Co(H_2mdp)(Ni(CN)$_4$)]** and **[Fe(H_2mdp)(Ni(CN)$_4$)].**

Identification code	**[Co(H_2mdp)(Ni(CN)$_4$)]**	**[Fe(H_2mdp)(Ni(CN)$_4$)]**
Empirical formula	$C_{15}H_{24}CoN_8NiO_4$	$C_{15}H_{24}FeN_8NiO_5$
Formula weight	498.06	510.947
Temperature/K	120.00(12)	120.0(4)
Crystal system	tetragonal	tetragonal
Space group	P4/nnc	I4/mmm
a/Å	14.3689(5)	14.4482(3)
b/Å	14.3689(5)	14.4482(3)
c/Å	21.6026(11)	21.7145(8)
α/°	90	90
β/°	90	90
γ/°	90	90
Volume/Å^3	4460.2(4)	4532.9(2)
Z	8	8
ρ_{calc}g/cm^3	1.483	1.497
μ/mm^{-1}	7.197	6.534
F(000)	1992.0	2048
Crystal size/mm^3	0.094 × 0.061 × 0.036	0.107 × 0.094 × 0.046
Radiation	Cu Kα (λ = 1.54184)	Cu Kα (λ = 1.54184)
2Θ range for data collection/°	3.694 to 73.409	4.33 to 77.66
Index ranges	-13 ≤ h ≤ 14, -17 ≤ k ≤ 16, -25 ≤ l ≤ 26	-7 ≤ h ≤ 17, -17 ≤ k ≤ 18, -27 ≤ l ≤ 26
Reflections collected	7815	7180
Independent reflections	2213 [R_{int} = 0.0558, R_{sigma} = 0.0476]	1375 [R_{int} = 0.1029, R_{sigma} = 0.0687]
Data/restraints/parameters	2213/0/165	1375/218/179
Goodness-of-fit on F^2	1.053	1.0257
Final R indexes [I>=2σ (I)]	R_1 = 0.0552, wR_2 = 0.1476	R_1 = 0.0564, wR_2 = 0.1613
Final R indexes [all data]	R_1 = 0.0839, wR_2 = 0.1721	R_1 = 0.0738, wR_2 = 0.1746
Largest diff. peak/hole / e Å^{-3}	0.889/-0.563	0.6105/-0.8965

Gas sorption measurements

Gas adsorption isotherms for **[Co(H$_2$mdp)(Ni(CN)$_4$)]** and **[Fe(H$_2$mdp)(Ni(CN)$_4$)]** were measured with a volumetric adsorption apparatus (Quantachrome Autosorb-iQ2). Ultra-high purity gases were used as received from BOC Gases. The as-synthesized samples were washed with dry acetone several times and 100-200 mg were transferred into a pre-dried and weighed sample tube and heated at rate of 10 °C/min to a temperature of 130 °C under a dynamic vacuum at 10^{-6} Torr then held for 20 hours. Accurate sample masses were calculated using degassed samples after the sample tube was backfilled with nitrogen.

Heat of adsorption (Q_{st})

Isosteric heat of adsorption$_2$ (Q_{st}) values were calculated from isotherms measured at 273 and 293 K for all measured gases. The isotherms were first fit to a viral equation:

$$\ln P = \ln N + \frac{1}{T}\sum_{i=0}^{m} a_i N^i + \sum_{i=0}^{m} b_i N^i \qquad s1$$

Where N is the amount of gas adsorbed at the pressure P, a and b are virial coefficients, m and n are the number of coefficients required to adequately describe the isotherm. To calculate Q_{st}, the fitting parameters from the above equation were input into the following equation:

$$Q_{st} = -R\sum_{i=0}^{m} a_i N^i \qquad s2$$

IAST selectivity calculations

Mixed gas adsorption isotherms and gas selectivities for different binary gas mixtures at 298 K were calculated based on the ideal adsorbed solution theory (IAST) proposed by Myers and Prausnitz[6]. To predict the adsorption performance of **[Co(H$_2$mdp)(Ni(CN)$_4$)]** and **[Fe(H$_2$mdp)(Ni(CN)$_4$)]** toward the separation of binary mixed gases, the single-component adsorption isotherms were first fit to a Dual Site Langmuir model or Single Site Langmuir model, as below:

$$q = \frac{q_1 b_1 P}{1 + b_1 P} + \frac{q_2 b_2 P}{1 + b_2 P} \; (Dual\ Site\ Langmuir\ Model) \qquad s3$$

$$q = \frac{q_1 b_1 P}{1 + b_1 P} \ (Single\ Site\ Langmuir\ Model) \qquad s4$$

Where q is the uptake of a gas; P is the equilibrium pressure and q_1, b_1, q_2 and b_2 are constants. These parameters were used subsequently to carry out the IAST calculations.

Dynamic column breakthrough measurements

Breakthrough experiments were performed in a stainless-steel fixed bed packed with approximately 0.5-1 g of **[Co(H_2mdp)(Ni(CN)$_4$)]** or **[Fe(H_2mdp)(Ni(CN)$_4$)]** powder. Prior to the breakthrough experiment, the fixed bed was heated at 120 °C under a flow of He for complete activation. The different gas mixtures (C_2H_2/CO_2-C_2H_2/CH_4-C_2H_2/CO_2/CH_4-C_3H_6/C_3H_8) were introduced and the effluent gas was monitored by mass spectrometry.

Dynamic breakthrough experiments for the mixture were performed under He as carrier gas, in which C_2H_2-CO_2-He (25/25/50 and 5/45/50, V/V), C_2H_2-CH_4-He (25/25/50 and 5/45/50, V/V), C_3H_6-C_3H_8-He (25/25/50 and 5/45/50, V/V), C_2H_2-CO_2-CH_4-He (16. 6/16.6/16.6/50, V/V), mixtures were introduced as feeds to flow over a column with a total flow rate of 6 mL/min at 293 K and 1 bar.

DFT calculations

Location of gases:

The initial location of CO_2, C_2 and C_3 gases in **[M(H_2mdp)(Ni(CN)$_4$)]** HUMs structures were obtained from the classical simulated annealing technique based on classical force field as implemented in sorption module in *Materials Studio*.[7] The framework atoms are kept frozen during the simulation and in each simulation, a single gas molecule is placed inside the simulation box that is composed of multiple unit cells so that the dimension along each direction is at least twice the cutoff radius. The interactions of gas – MOF frameworks were modelled as a combination of pairwise site-site Lennard-Jones (LJ) and Coulombic potentials. The LJ potential parameters of both the framework atoms and the gas molecules are adopted from the Universal force field (UFF).[8] In the simulated annealing method, the temperature was lowered stepwise, allowing the gas molecule to reach a desirable configuration based on configurational-biased NVT Monte Carlo simulation moves such as rotation, translation, and repositioning with preset probabilities of occurrence. This process of heating and cooling the system was repeated in several heating cycles to find the local minima. Forty heating cycles were performed where the maximum temperature and the final temperature were 10^5 K and 100 K, respectively. The lowest energy final configuration obtained from simulated annealing is chosen to be initial location for further DFT binding energy calculations.

DFT calculations

Periodic geometric optimization and the static binding energies for each of CO_2, C_2 and C_3 gases, in **[M(H_2mdp)(Ni(CN)$_4$)]** HUM structures were calculated using density functional theory (DFT) as implemented in the software package VASP 5.4.4.[9] It is well-known that standard DFT methods based on generalized gradient approximation do not fully account for the long-range dispersion interactions between the framework and the bound adsorbates. To accurately estimate static binding energies for each benzene with the framework, we implemented dispersion corrections using DFT-D3 method.[10] Electron exchange and correlation were described using the generalized gradient approximation of Perdew, Burke, and Ernzerhof (PBE)[11] and the projector-augmented wave potentials were used to treat core and valence electrons.[12] In all cases, we used a plane-wave kinetic energy cutoff of 550 eV depending on the system size and a Gamma-point mesh (2 x 2 x 1) for sampling the Brillouin

zone. The ionic coordinates and the lattice parameters were fully relaxed until the Hellman-Feynman ionic forces were less than 0.02 eV/Å.

Interaction Energies

Static interaction energies (ΔE) at 0 K in vacuum were calculated using the following expression:

$$\Delta E = E_{MOF+gas} - E_{MOF} - E_{gas}$$

where E_X refers, respectively, to the total energies of the MOF + gas complex, the MOF alone, and the gas respectively.

Supplementary figures

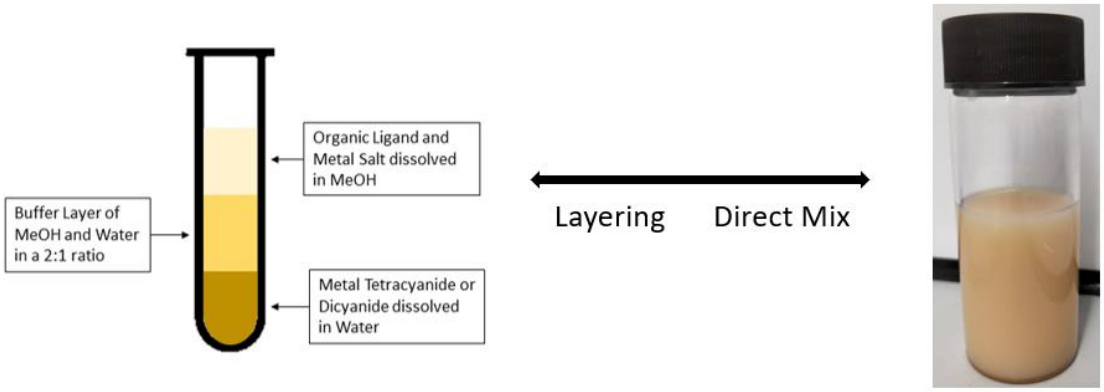

Figure S1. Illustration of synthesis of **[M(H₂mdp)(Ni(CN)₄)]** (M= Co, Fe) through layering (left) and direct mix (right) methods.

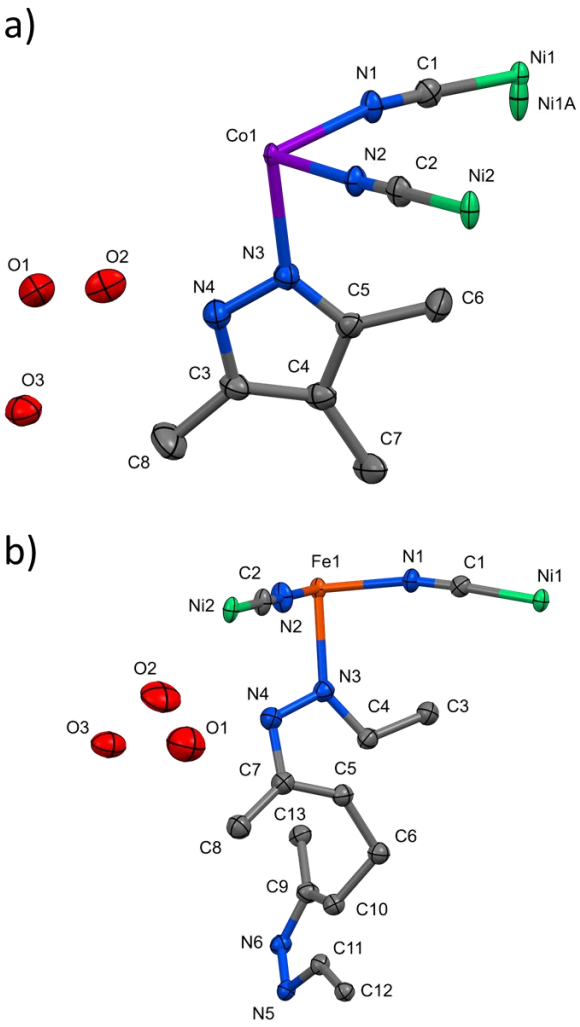

Figure S2. Asymmetric units of a) **[Co(H₂mdp)(Ni(CN)₄)]** and b) **[Fe(H₂mdp)(Ni(CN)₄)]**, displayed with a 50% thermal ellipsoid probability.

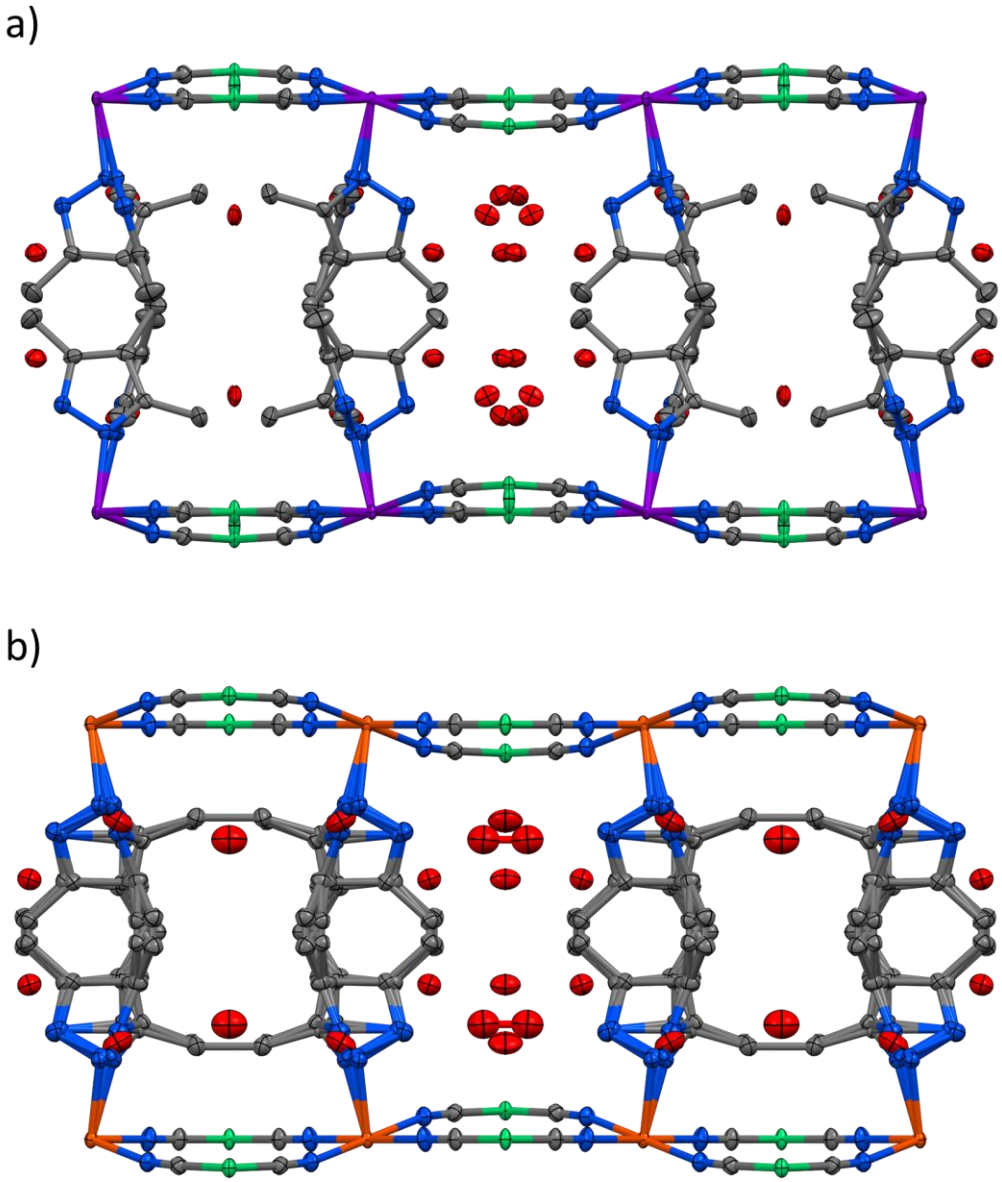

Figure S3. Crystal packing of a) **[Co(H$_2$mdp)(Ni(CN)$_4$)]** and b) **[Fe(H$_2$mdp)(Ni(CN)$_4$)]**along the crystallographic a-axis, displayed with a 50% thermal ellipsoid probability. Fig. S3 highlights disorder present within the H$_2$mdp ligand within the **[Fe(H$_2$mdp)(Ni(CN)$_4$)]** crystal.

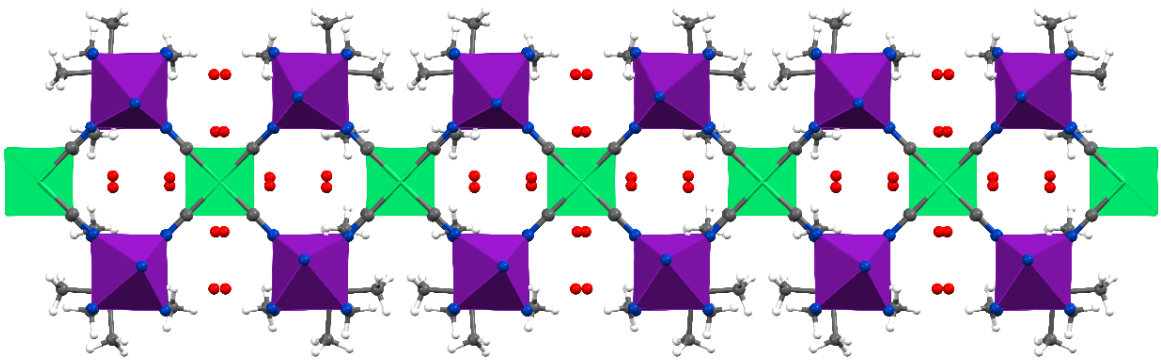

Figure S4. Crystal packing of **[Co(H$_2$mdp)(Ni(CN)$_4$)]** along the crystallographic c-axis.

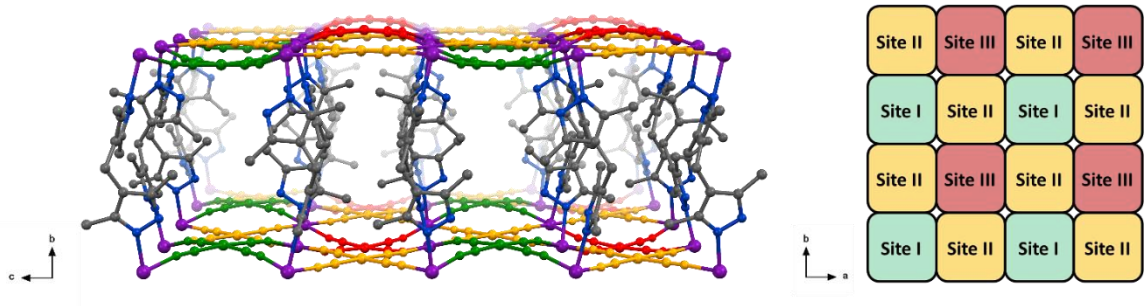

Figure S5. Packing diagram (left) and schematic representation (right) of the arrangement of the three different sites within the pores the **[M(H₂mdp)(Ni(CN)₄)]** frameworks. The same colour coding has been used in each *i.e.,* green (site I), gold (site II) and pink (site III).

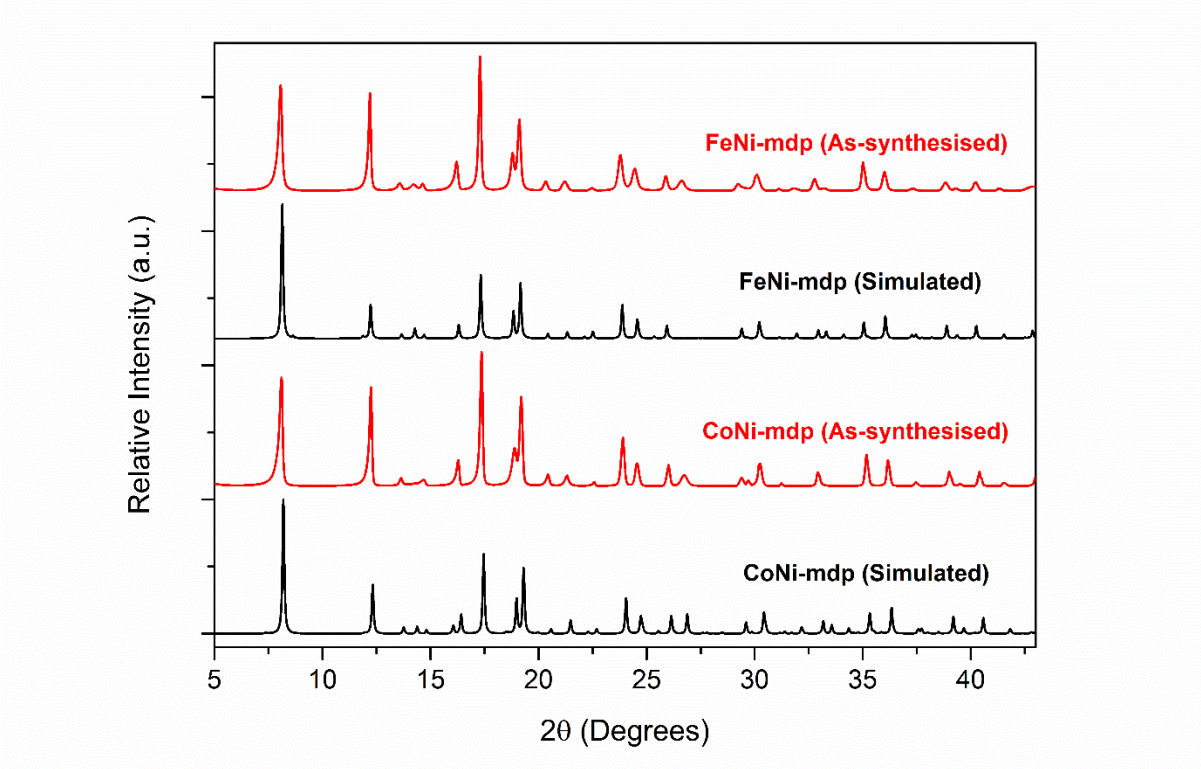

Figure S6. Comparison of PXRD profiles for the simulated (derived from SCXRD) and the as-synthesised microcrystalline batch samples prepared by direct mix for **[Co(H₂mdp)(Ni(CN)₄)]** and **[Fe(H₂mdp)(Ni(CN)₄)]**.

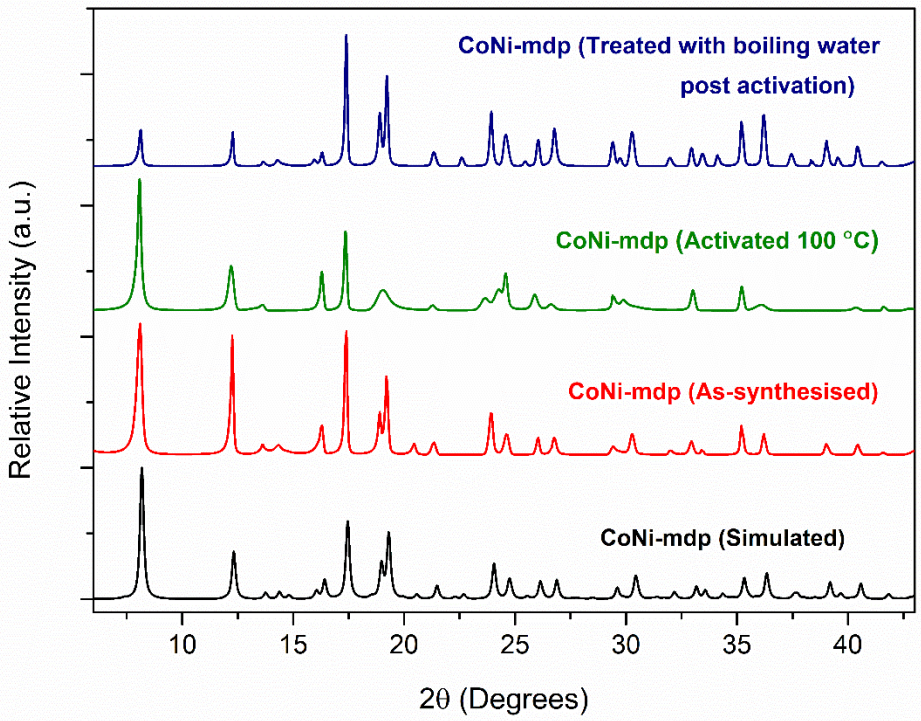

Figure S7. Comparison of PXRD profiles for the simulated (derived from SCXRD) and the as-synthesised microcrystalline batch samples prepared by direct mix for **[Co(H$_2$mdp)(Ni(CN)$_4$)]** following activation and after treatment with boiling water.

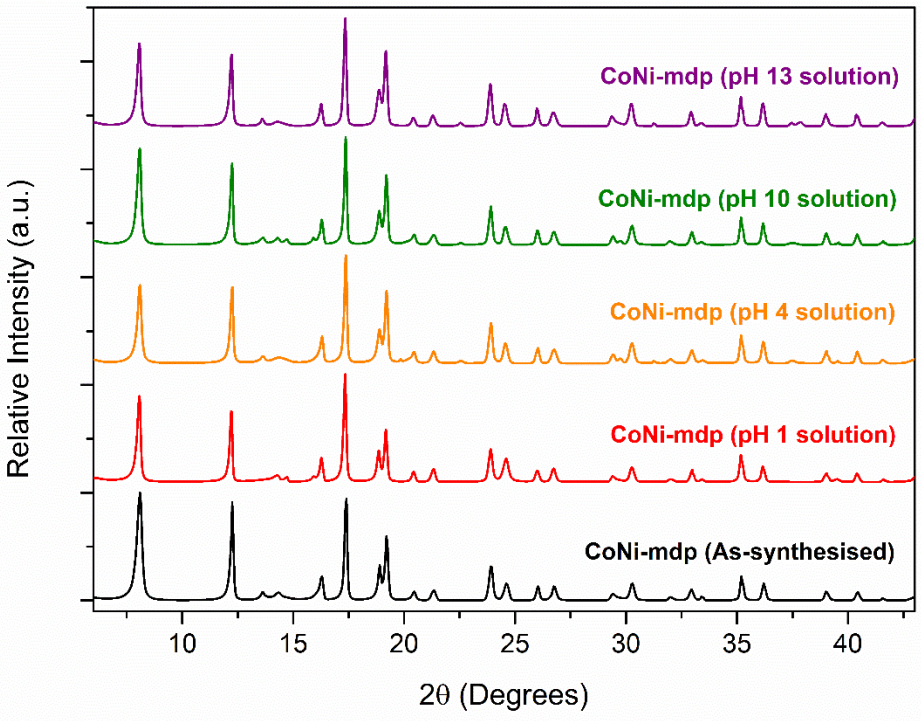

Figure S8. Comparison of PXRD profiles for the simulated (derived from SCXRD) of **[Co(H$_2$mdp)(Ni(CN)$_4$)]** after immersion in solutions of various pHs.

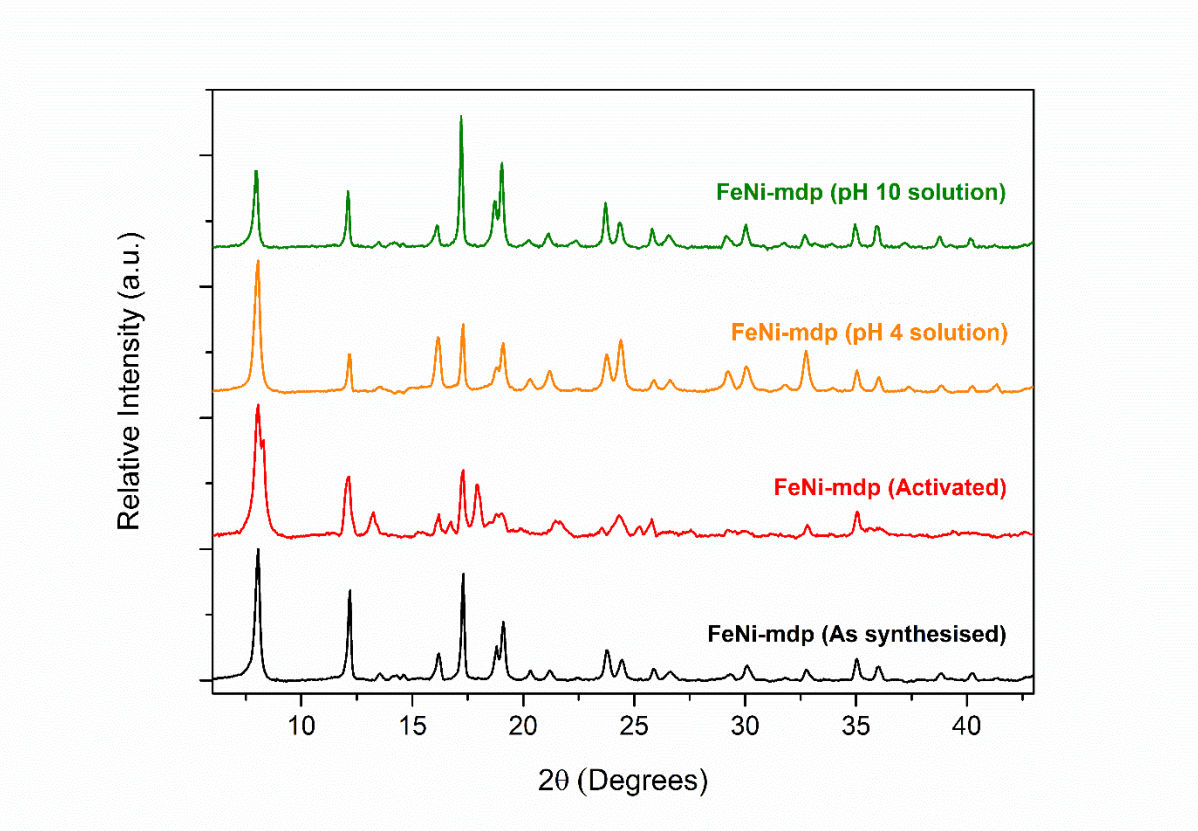

Figure S9. Comparison of PXRD profiles for the simulated (derived from SCXRD) of **[Fe(H$_2$mdp)(Ni(CN)$_4$)]** after immersion in solutions of various pHs.

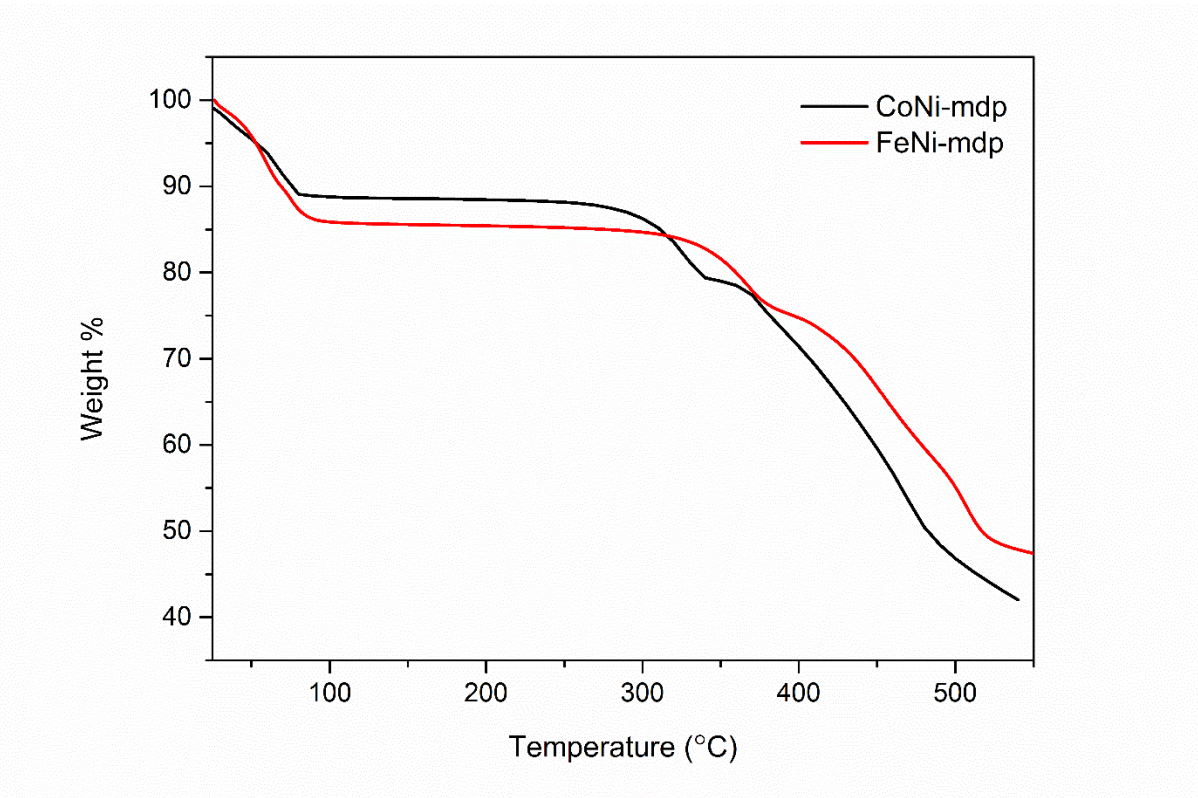

Figure S10. Thermogravimetric profile of **[Co(H$_2$mdp)(Ni(CN)$_4$)]** and **[Fe(H$_2$mdp)(Ni(CN)$_4$)]**. TG analyses performed under N_2 at a heating rate of 10 °C/ min.

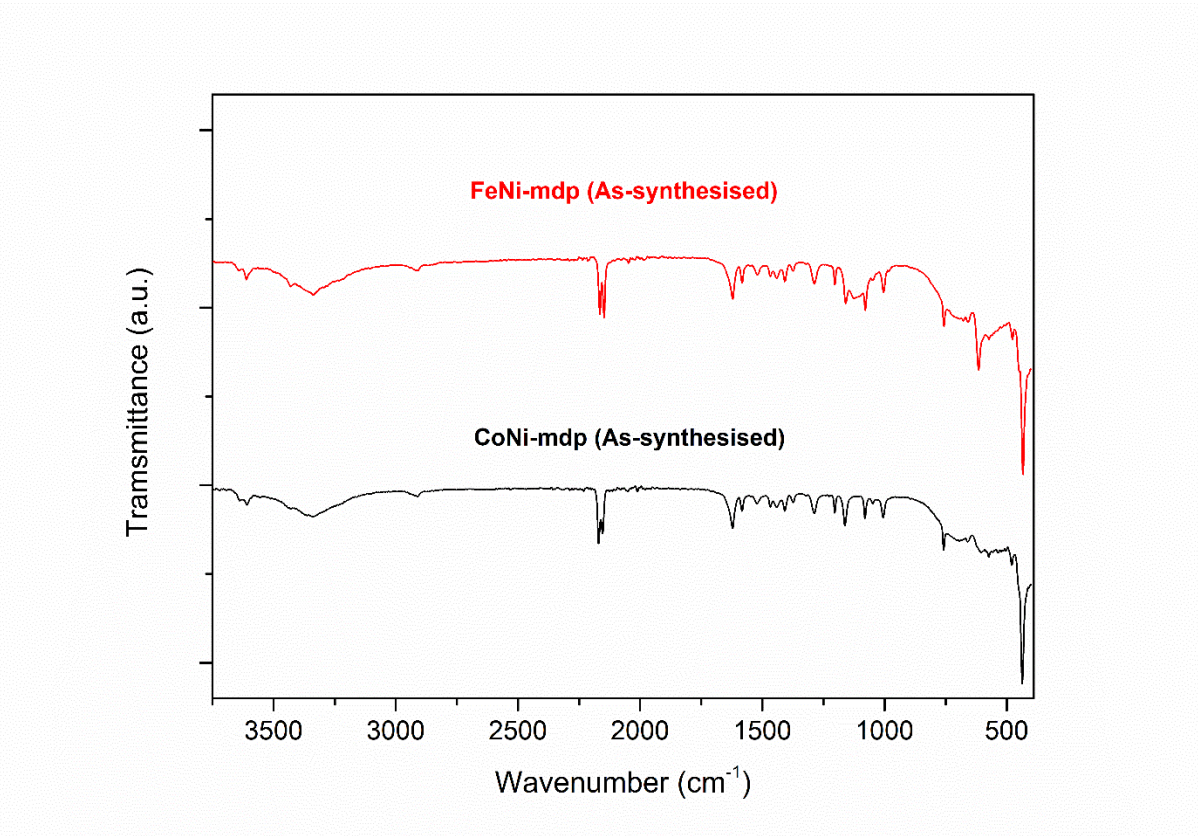

Figure S11. FT-IR spectra of **[Co(H₂mdp)(Ni(CN)₄)]** and **[Fe(H₂mdp)(Ni(CN)₄)]**.

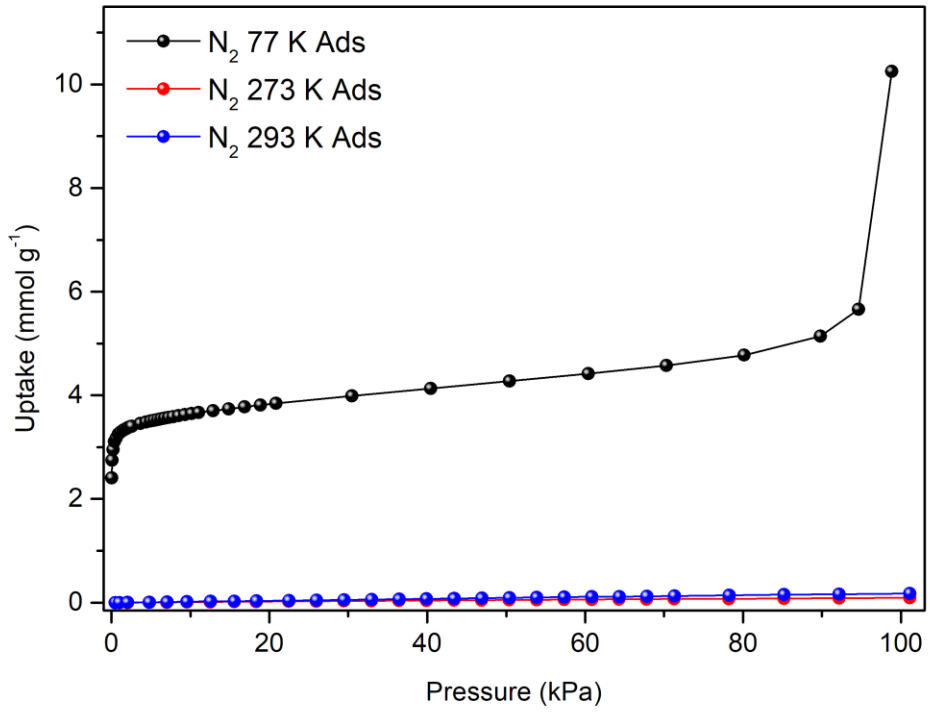

Figure S12. N_2 adsorption isotherms of **[Co(H₂mdp)(Ni(CN)₄)]** at 77 K, 273 K and 293 K.

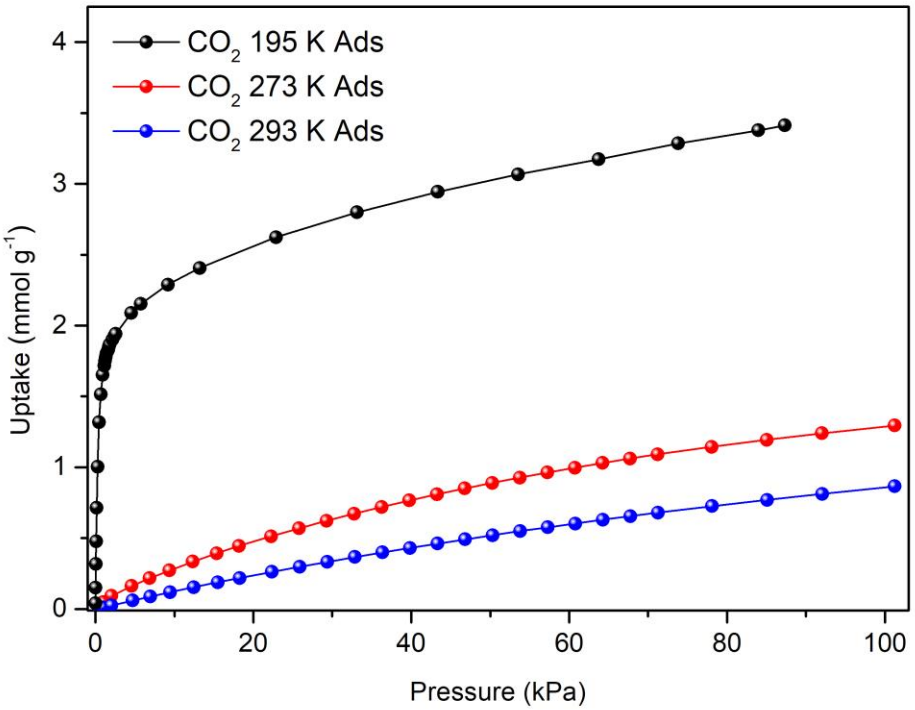

Figure S13. CO_2 adsorption isotherms of **[Co(H₂mdp)(Ni(CN)₄)]** at 195 K, 273 K and 298 K.

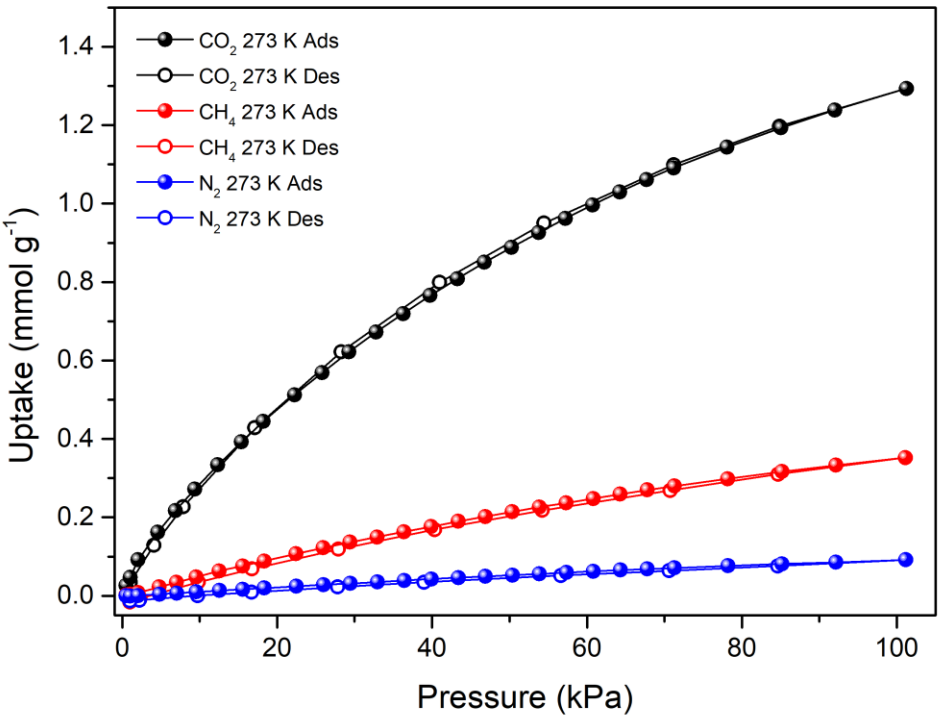

Figure S14. Adsorption isotherms of CO_2, CH_4 and N_2 for **[Co(H₂mdp)(Ni(CN)₄)]** at 273 K.

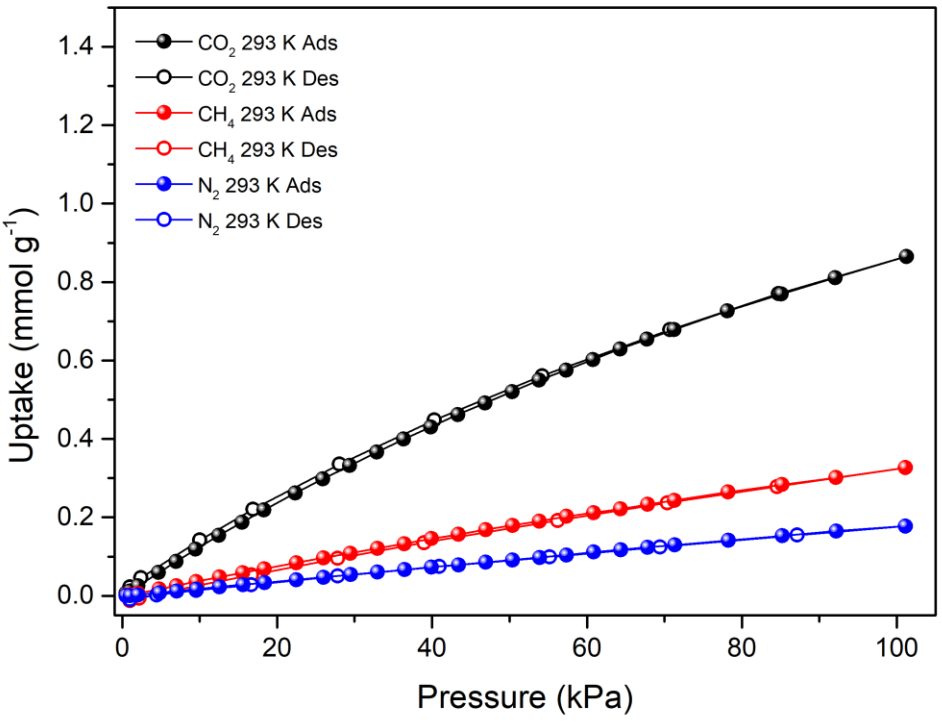

Figure S15. Adsorption isotherms of CO_2, CH_4 and N_2 for **[Co(H₂mdp)(Ni(CN)₄)]** at 293 K.

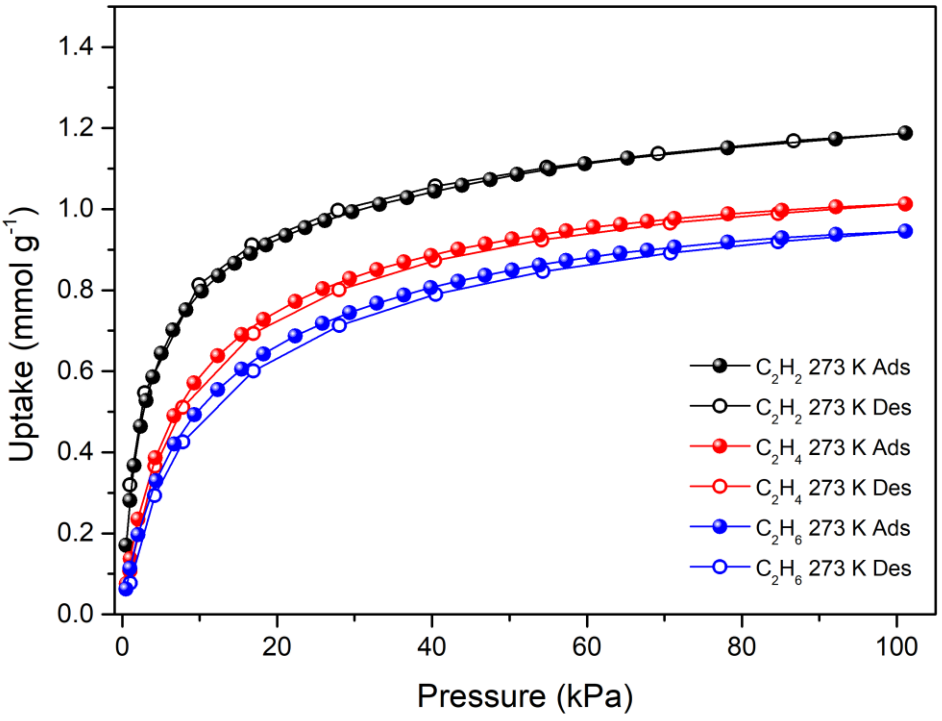

Figure S16. Adsorption isotherms of C_2H_2, C_2H_4 and C_2H_6 for **[Co(H₂mdp)(Ni(CN)₄)]** at 273 K.

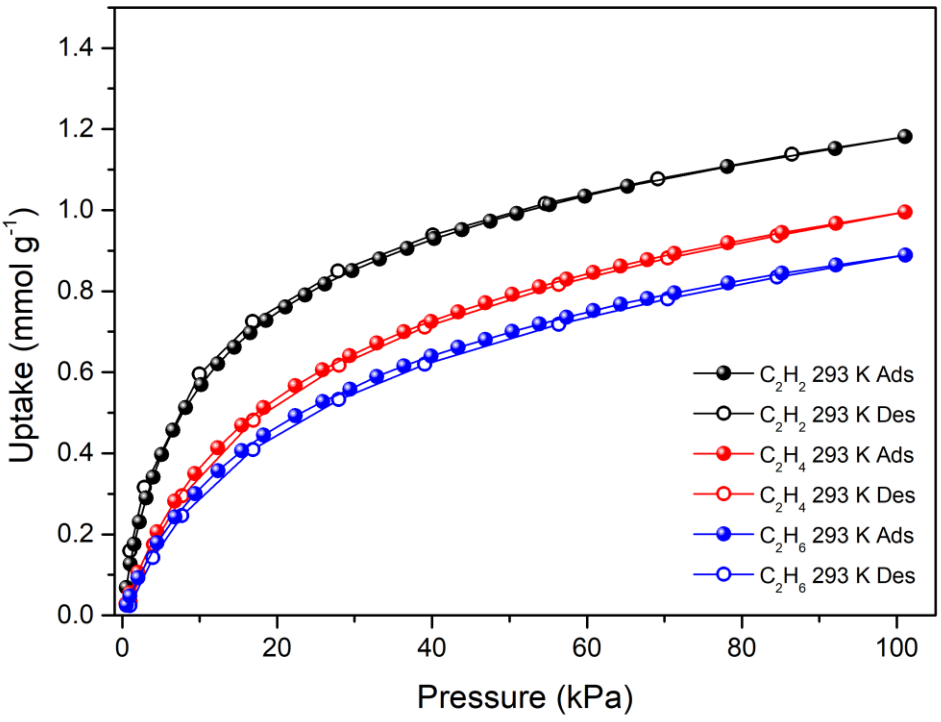

Figure S17. Adsorption isotherms of C_2H_2, C_2H_4 and C_2H_6 for **[Co(H₂mdp)(Ni(CN)₄)]** at 293 K.

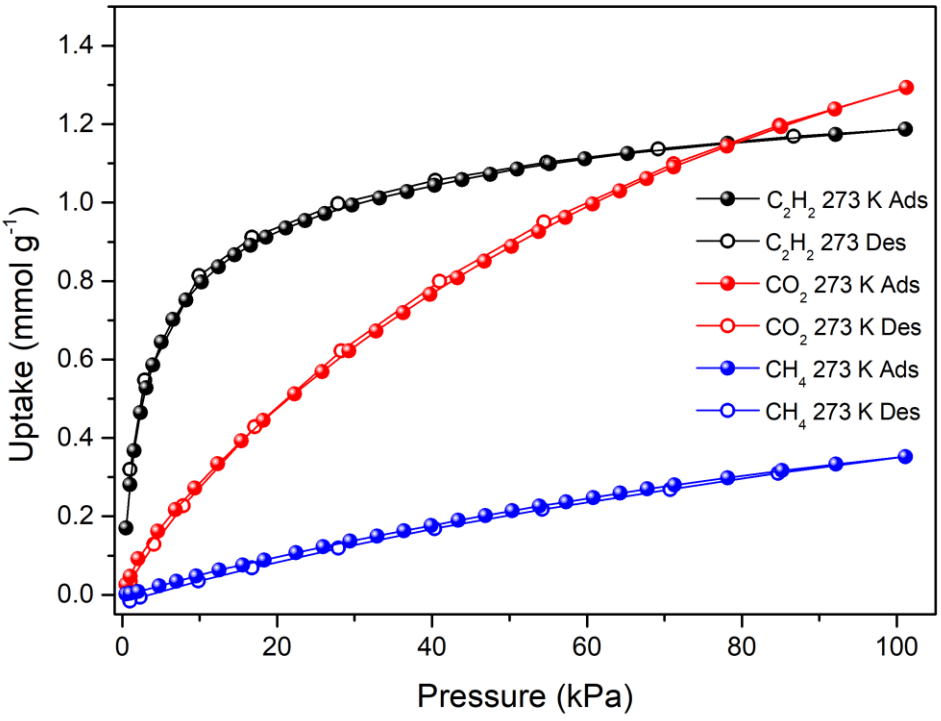

Figure S18. C_2H_2, CO_2 and CH_4 adsorption isotherms for **[Co(H₂mdp)(Ni(CN)₄)]** at 273 K.

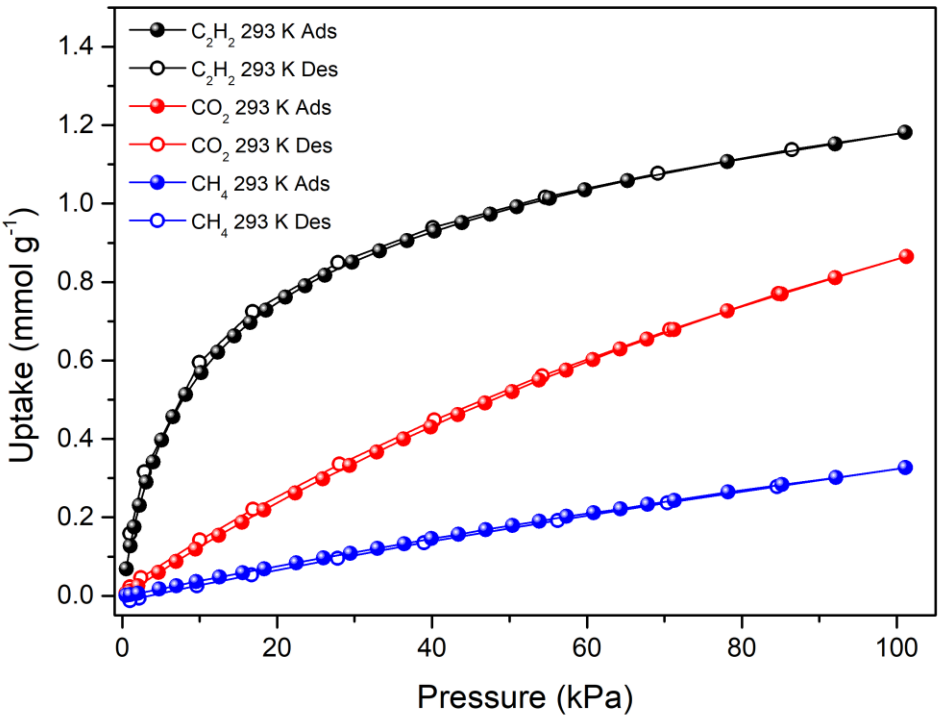

Figure S19. C_2H_2, CO_2 and CH_4 adsorption isotherms for **[Co(H₂mdp)(Ni(CN)₄)]** at 293 K.

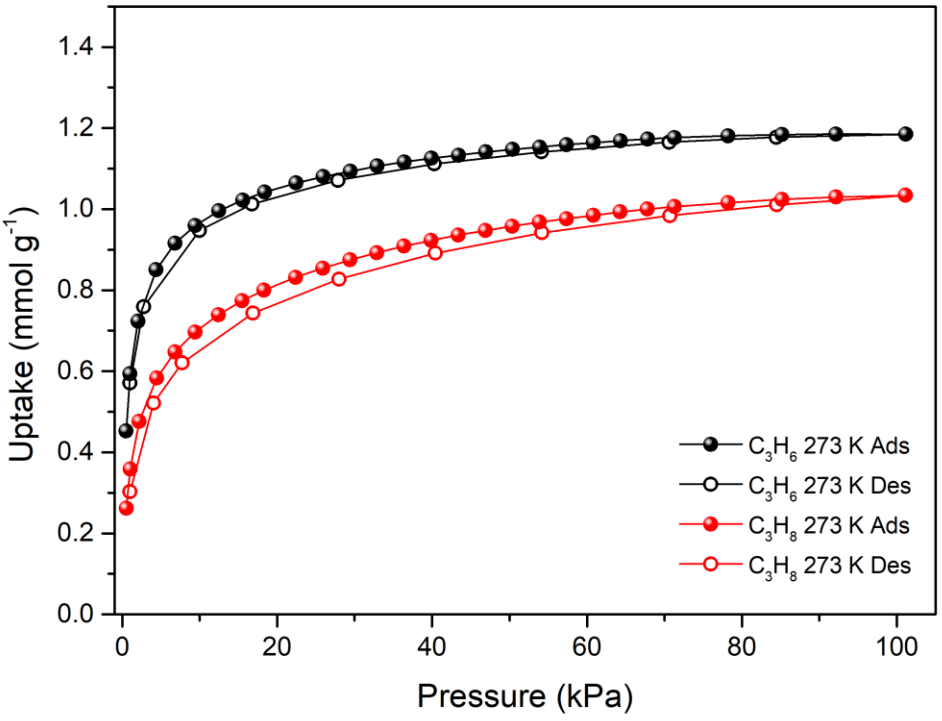

Figure S20. C_3H_6 and C_3H_8 adsorption isotherms for **[Co(H₂mdp)(Ni(CN)₄)]** at 273 K.

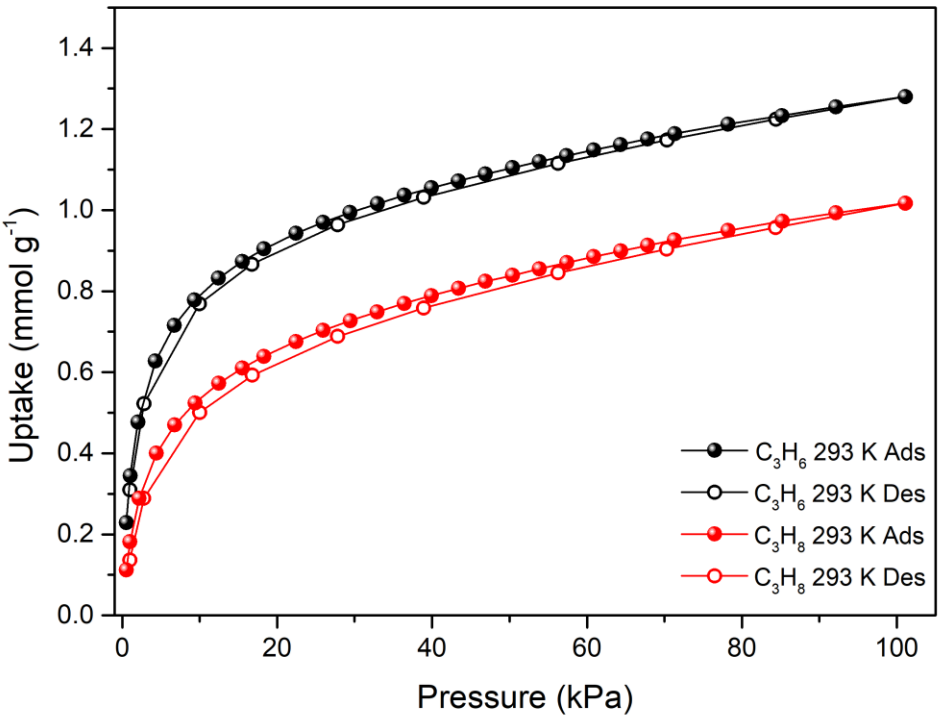

Figure S21. C_3H_6 and C_3H_8 adsorption isotherms for **[Co(H₂mdp)(Ni(CN)₄)]** at 293 K.

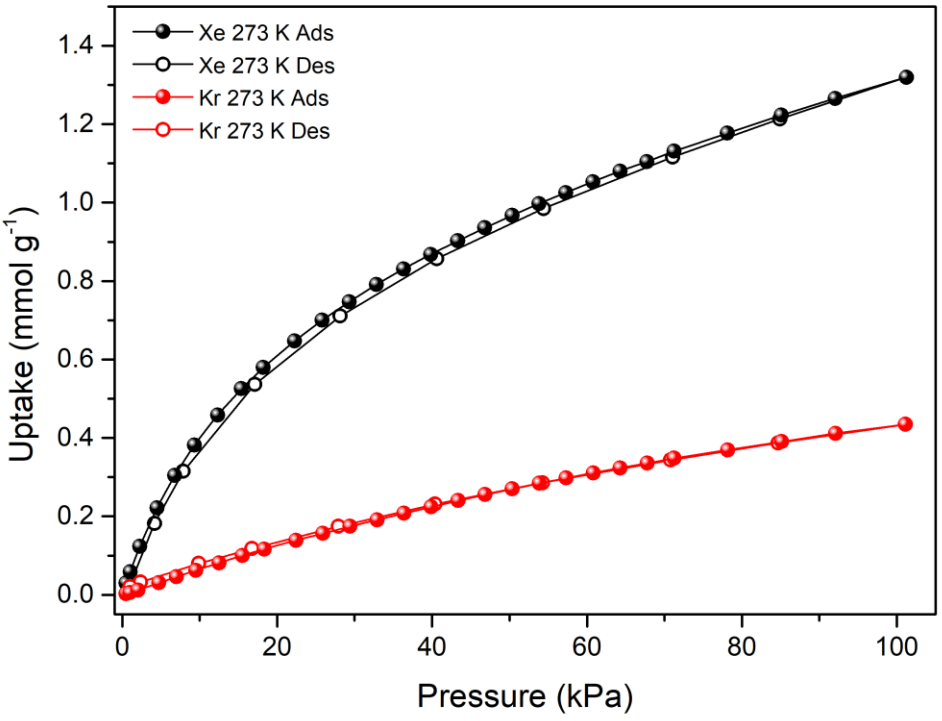

Figure S22. Xe and Kr adsorption isotherms for **[Co(H₂mdp)(Ni(CN)₄)]** at 273 K.

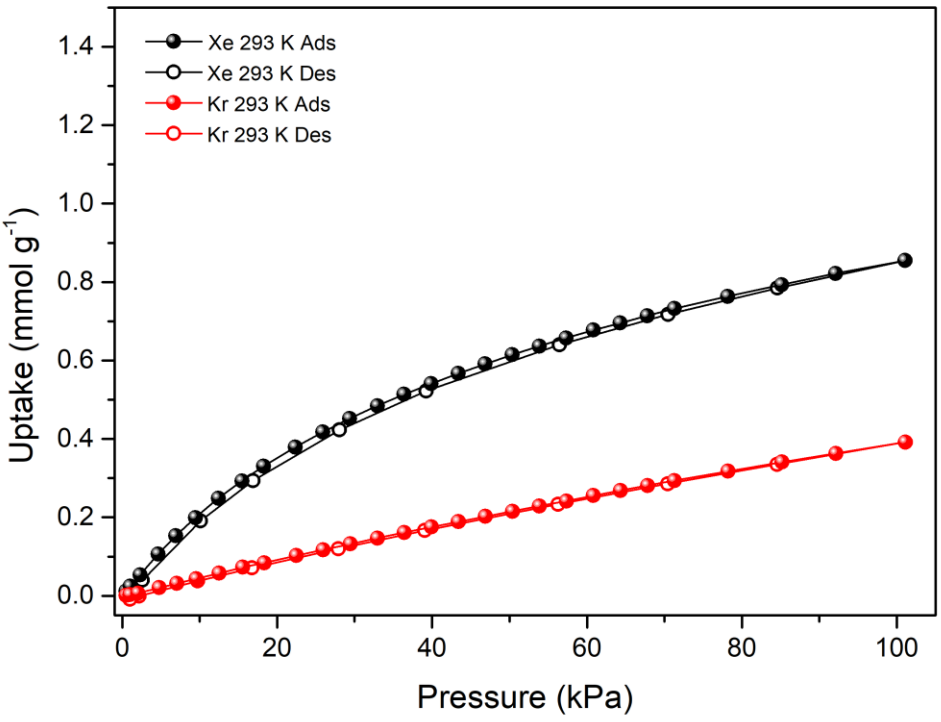

Figure S23. Xe and Kr adsorption isotherms for **[Co(H₂mdp)(Ni(CN)₄)]** at 293 K.

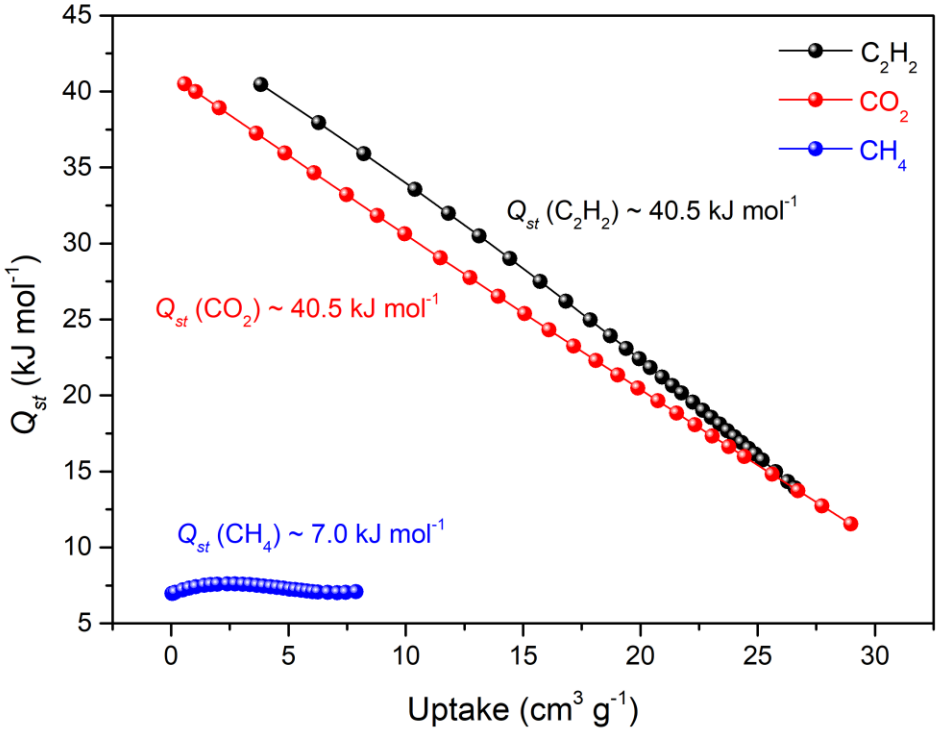

Figure S24. Isosteric heats of adsorption for C_2H_2, CO_2 and CH_4 for **[Co(H₂mdp)(Ni(CN)₄)]**.

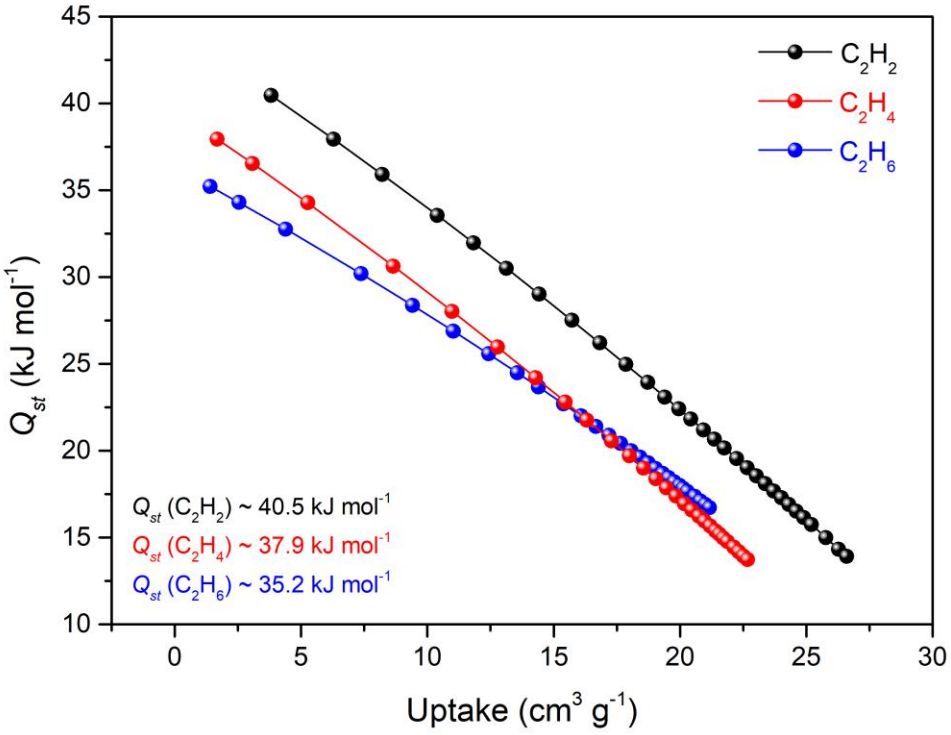

Figure S25. C_2H_2, C_2H_4 and C_2H_6 isosteric heats of adsorption for **[Co(H₂mdp)(Ni(CN)₄)]**.

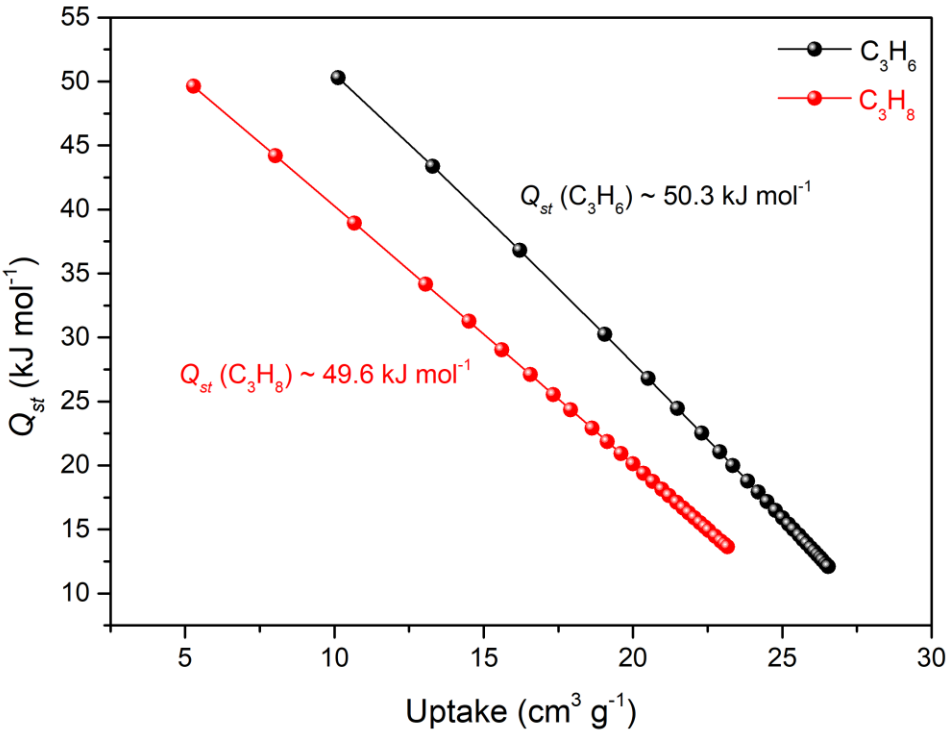

Figure S26. Isosteric heats of adsorption for C_3H_6, and C_3H_8 for **[Co(H₂mdp)(Ni(CN)₄)]**.

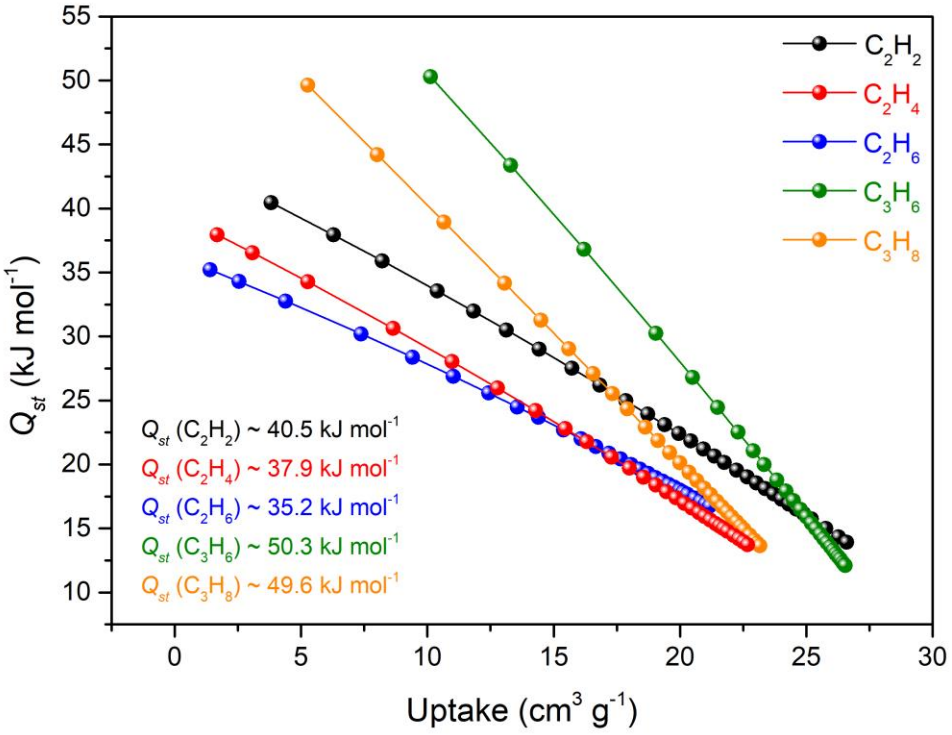

Figure S27. Isosteric heats of adsorption for C2 and C3 gases for **[Co(H₂mdp)(Ni(CN)₄)]**.

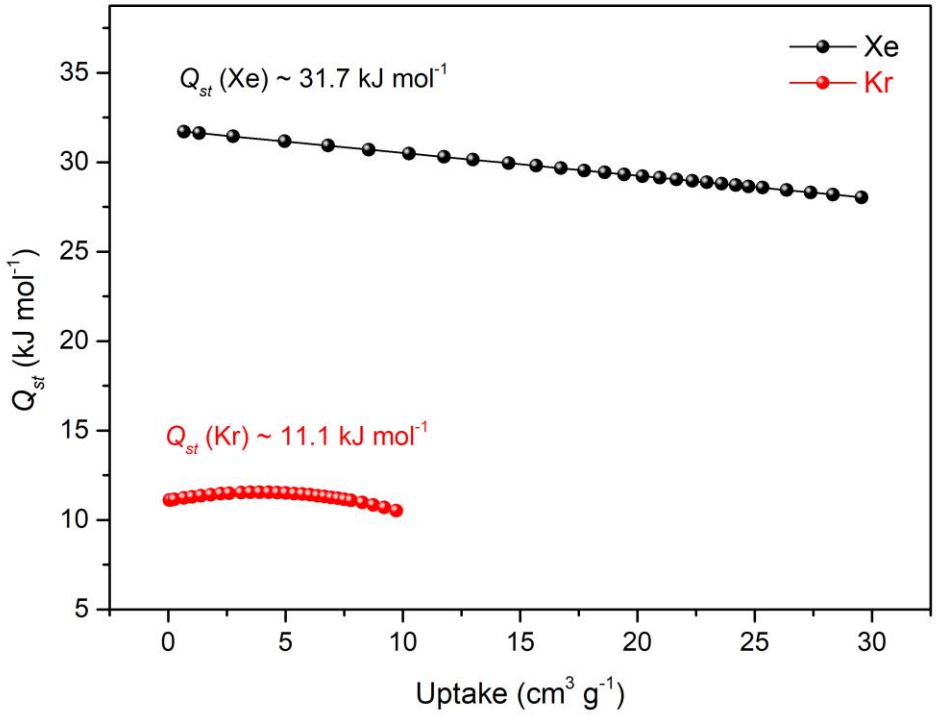

Figure S28. Isosteric heats of adsorption for Xe and Kr for **[Co(H₂mdp)(Ni(CN)₄)]**.

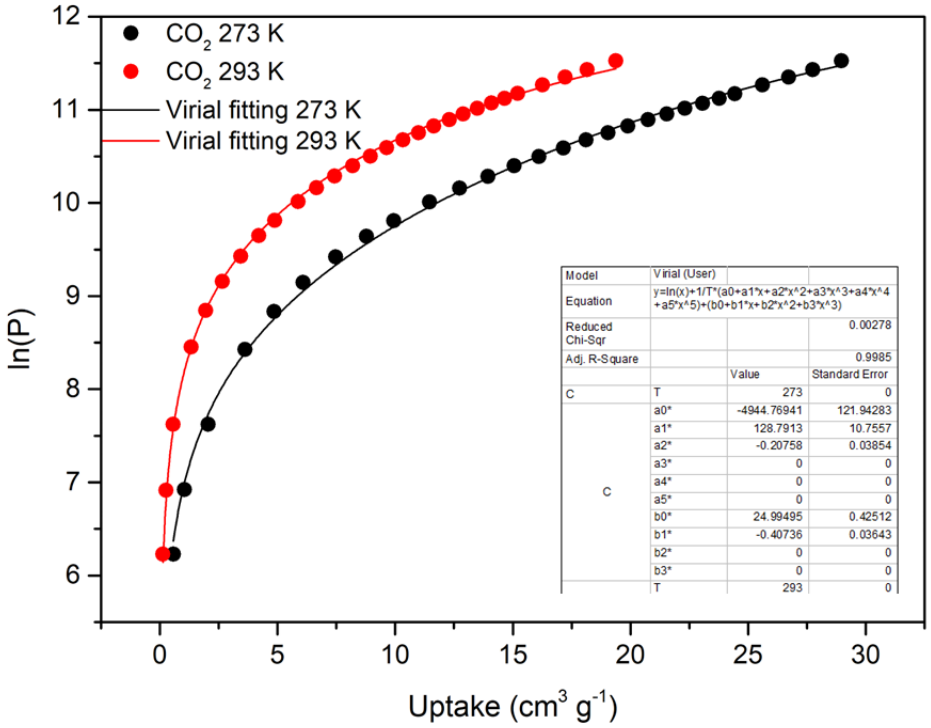

Figure S29. Virial fitting of the CO_2 adsorption isotherms for **[Co(H₂mdp)(Ni(CN)₄)]**.

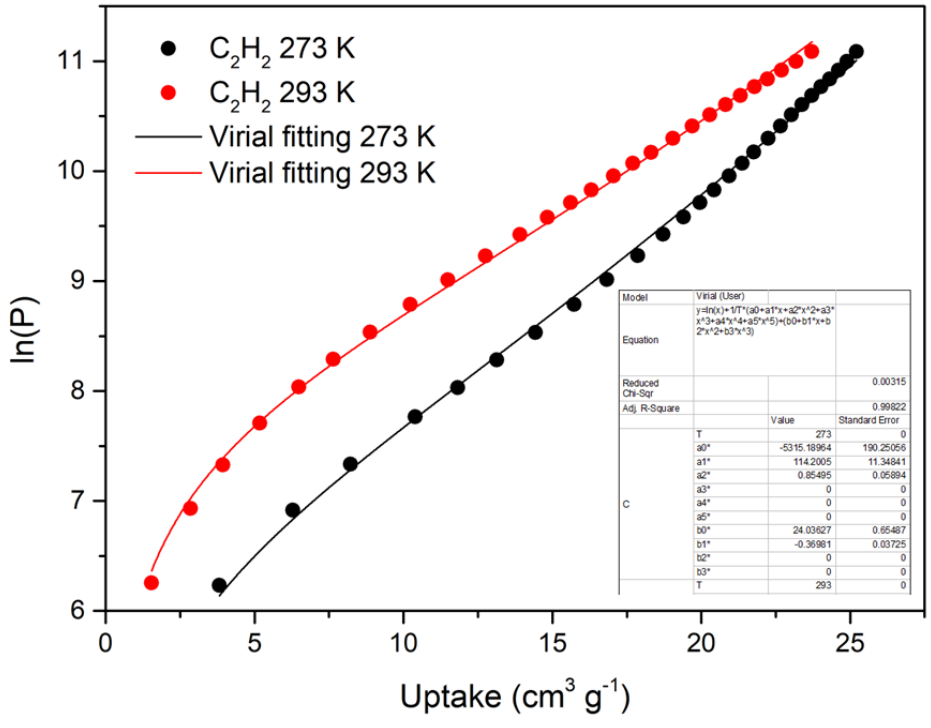

Figure S30. Virial fitting of the C_2H_2 adsorption isotherms for **[Co(H₂mdp)(Ni(CN)₄)]**.

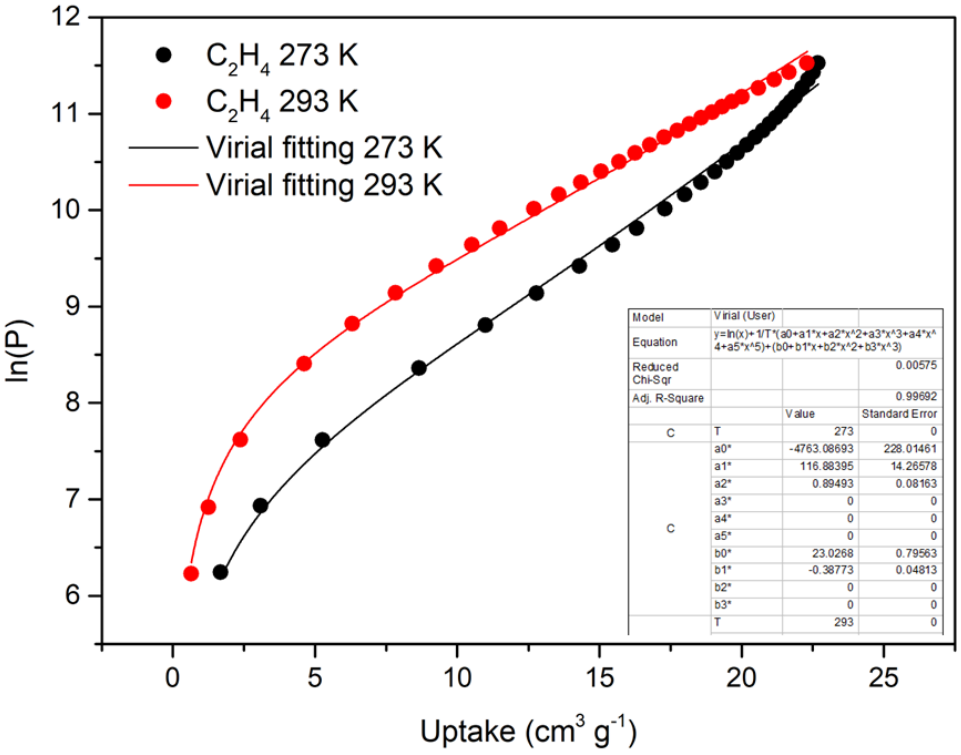

Figure S31. Virial fitting of the C_2H_4 adsorption isotherms for **[Co(H₂mdp)(Ni(CN)₄)]**.

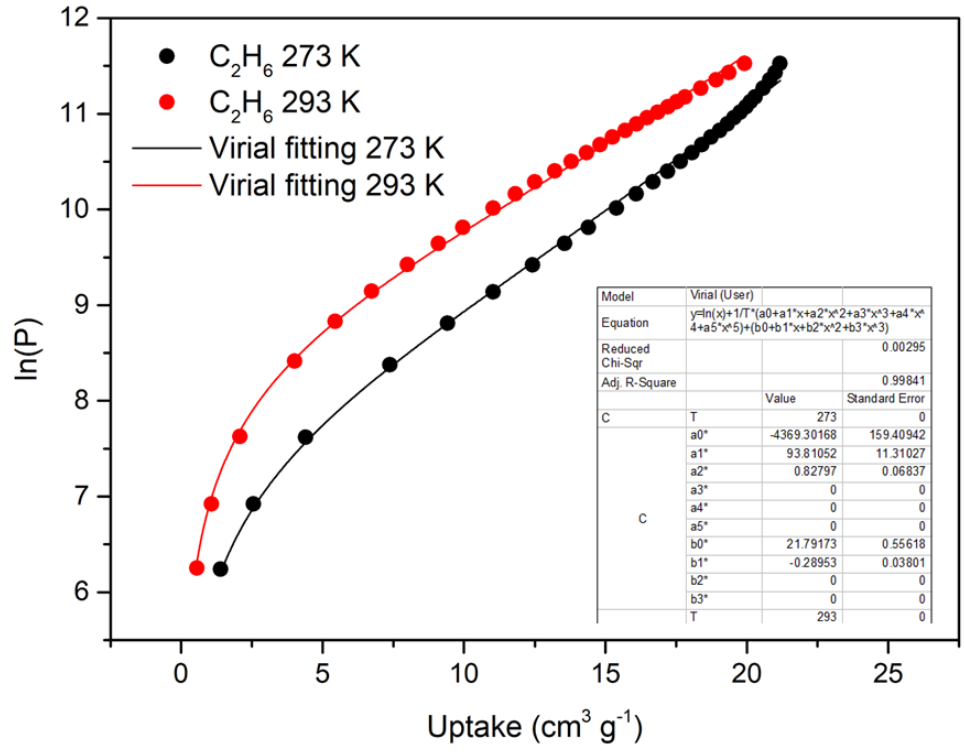

Figure S32. Virial fitting of the C_2H_6 adsorption isotherms for **[Co(H₂mdp)(Ni(CN)₄)]**.

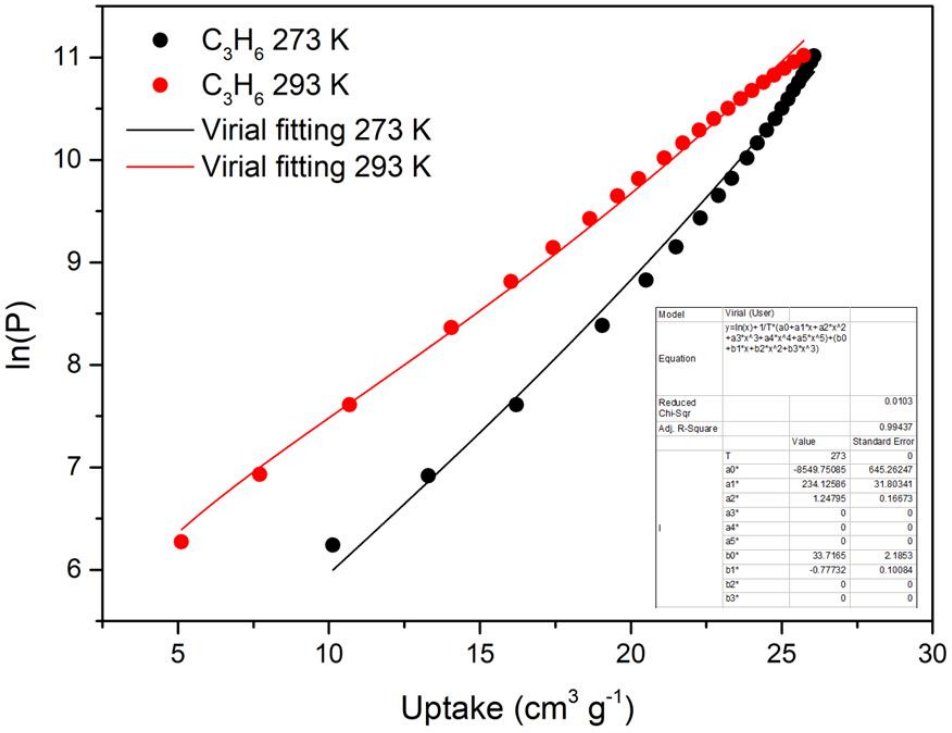

Figure S33. Virial fitting of the C_3H_6 adsorption isotherms for **[Co(H₂mdp)(Ni(CN)₄)]**.

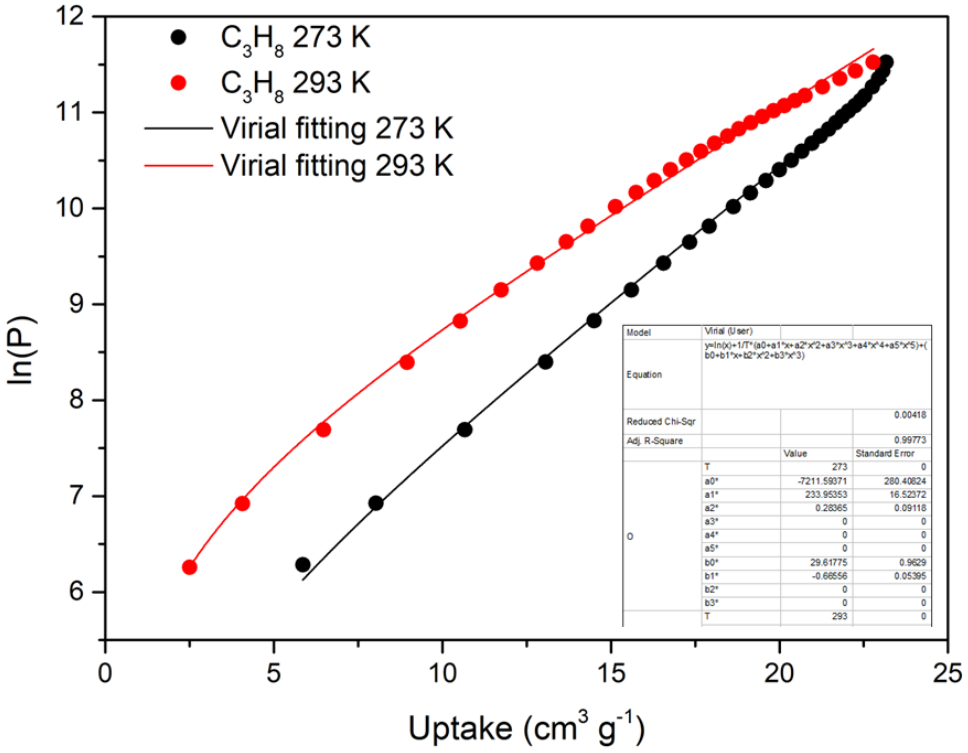

Figure S34. Virial fitting of the C_3H_8 adsorption isotherms for **[Co(H₂mdp)(Ni(CN)₄)]**.

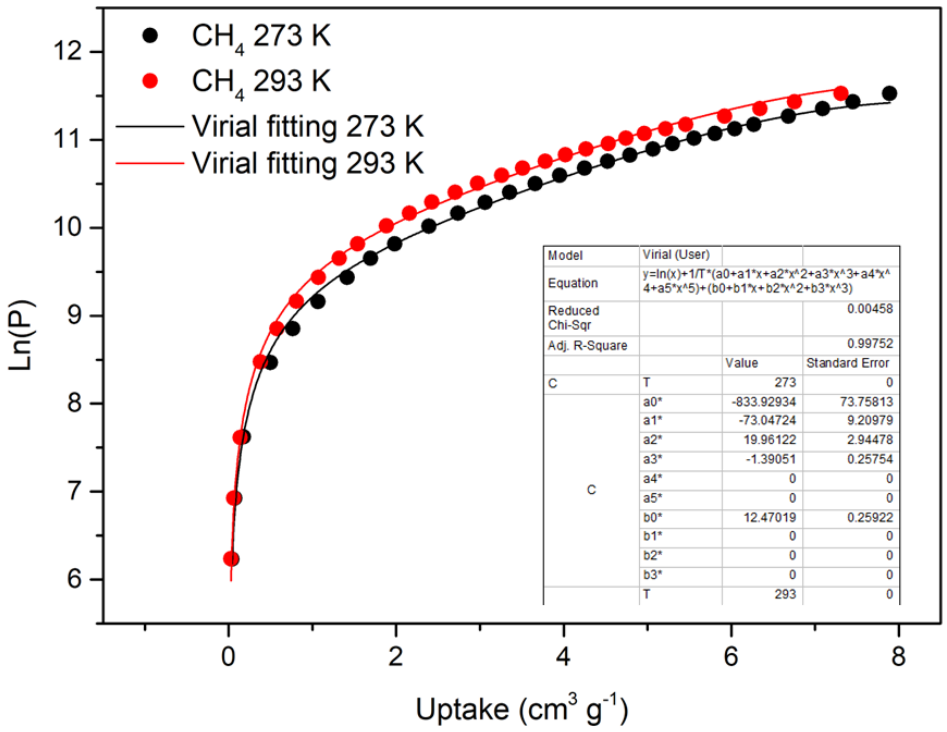

Figure S35. Virial fitting of the CH4 adsorption isotherms for **[Co(H2mdp)(Ni(CN)4)]**.

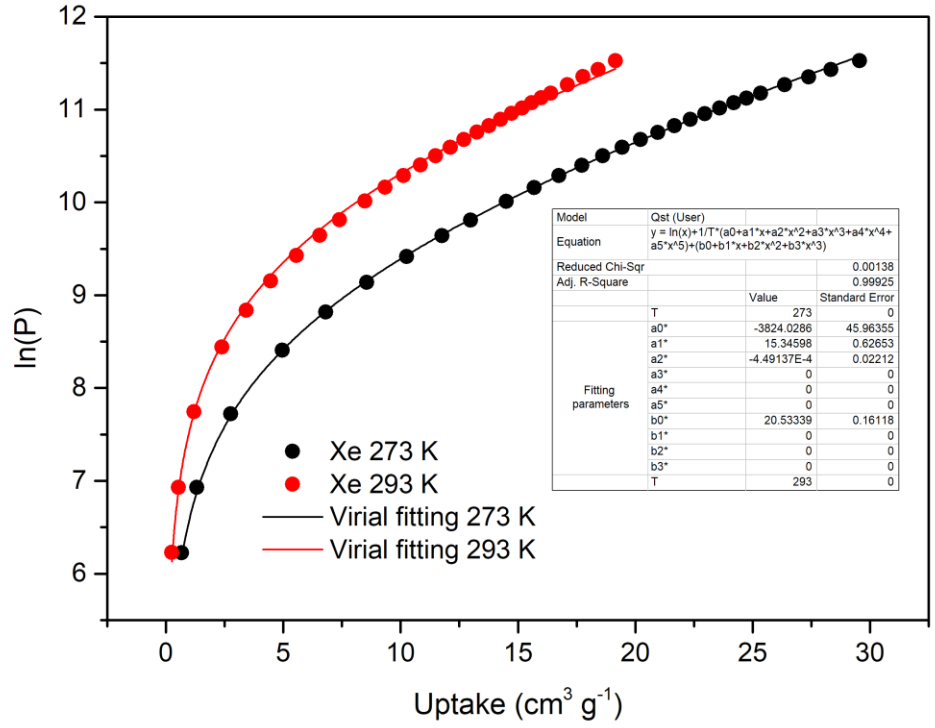

Figure S36. Virial fitting of the Xe adsorption isotherms for **[Co(H$_2$mdp)(Ni(CN)$_4$)]**.

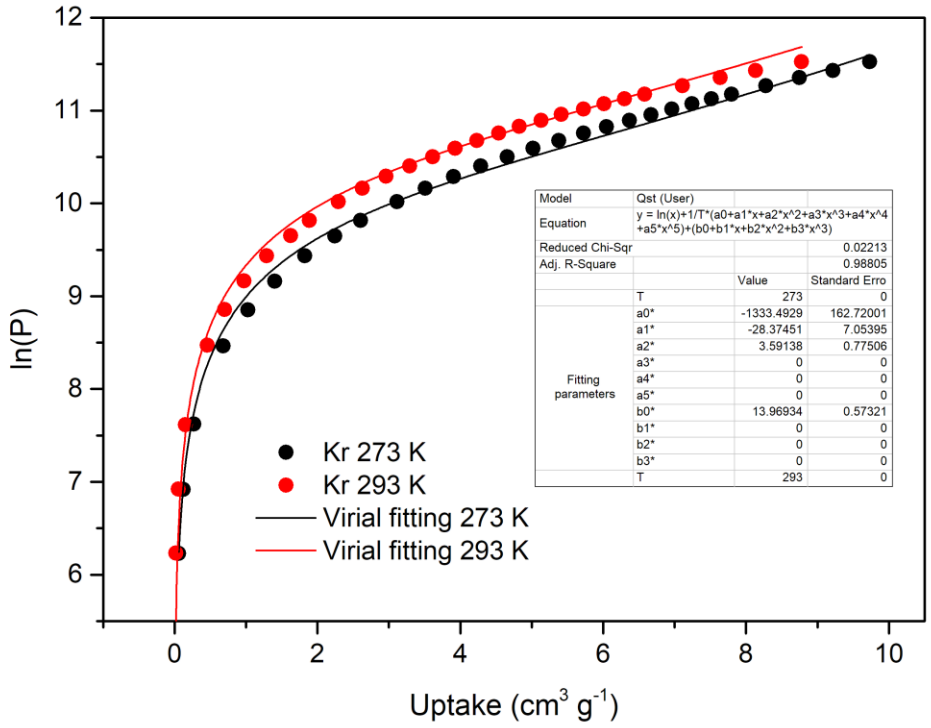

Figure S37. Virial fitting of the Kr adsorption isotherms for **[Co(H₂mdp)(Ni(CN)₄)]**.

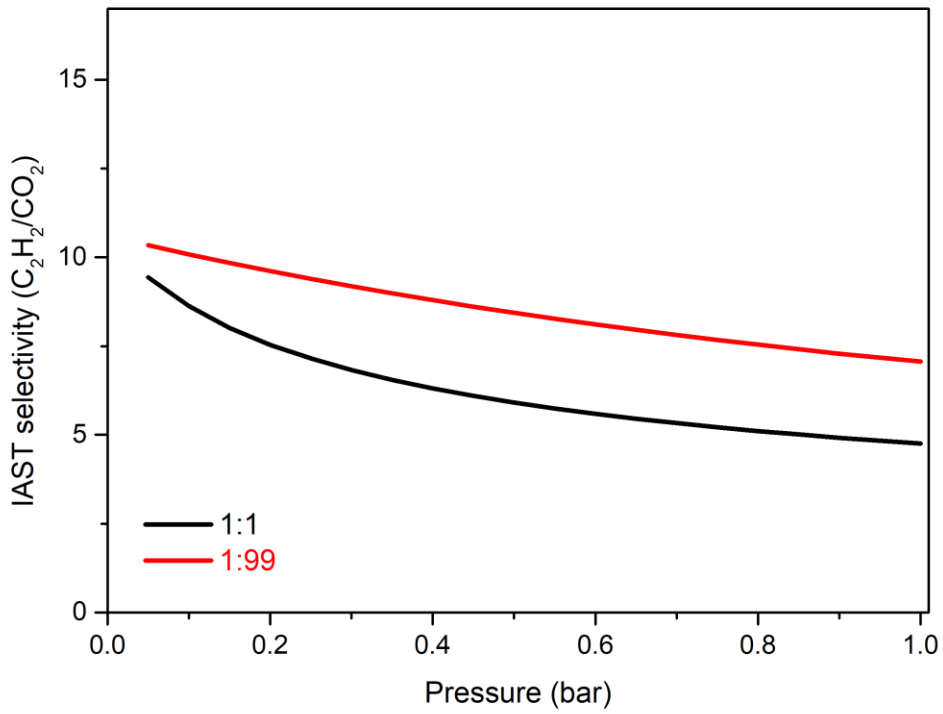

Figure S38. IAST selectivity of C_2H_2 and CO_2 (1:1 and 1:99 gas mixtures), calculated at 1 bar and 293K for **[Co(H₂mdp)(Ni(CN)₄)]**.

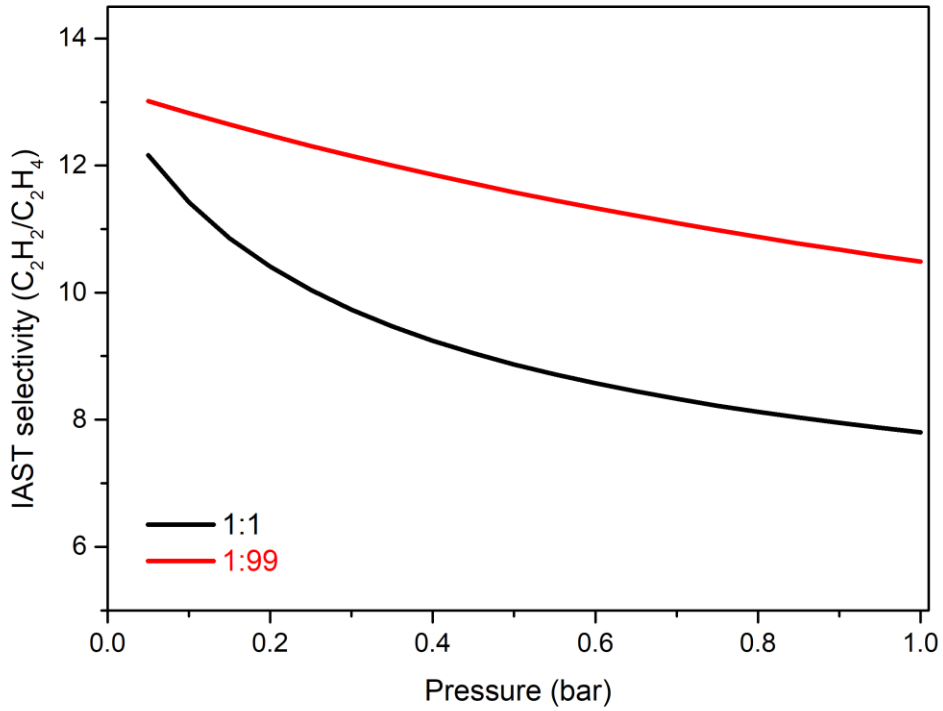

Figure S39. IAST selectivity of C_2H_2 and C_2H_4 (1:1 and 1:99 gas mixtures), calculated at 1 bar and 293K for **[Co(H₂mdp)(Ni(CN)₄)]**.

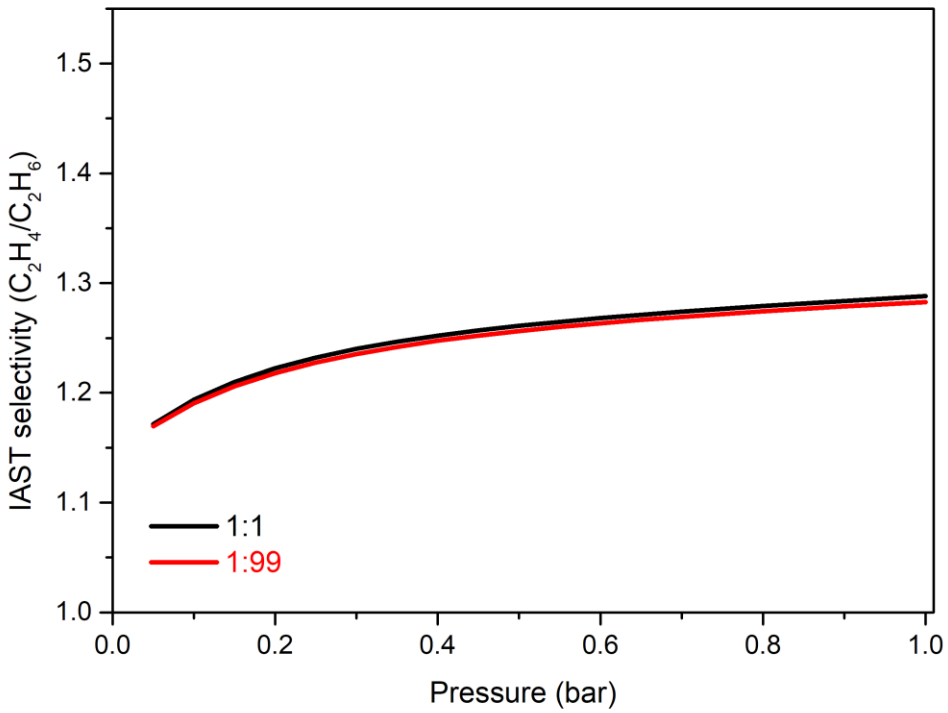

Figure S40. IAST selectivity of C_2H_4 and C_2H_6 (1:1 and 1:99 gas mixtures), calculated at 1 bar and 293K for **[Co(H₂mdp)(Ni(CN)₄)]**.

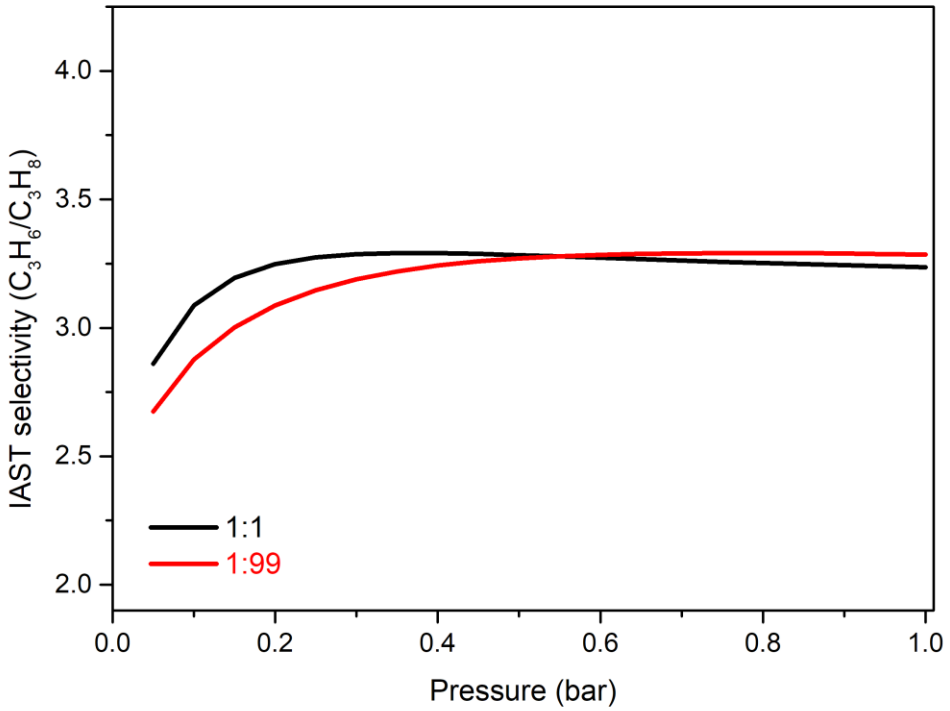

Figure S41. IAST selectivity of C_3H_6 and C_3H_8 (1:1 and 1:99 gas mixtures), calculated at 1 bar and 293K for **[Co(H₂mdp)(Ni(CN)₄)]**.

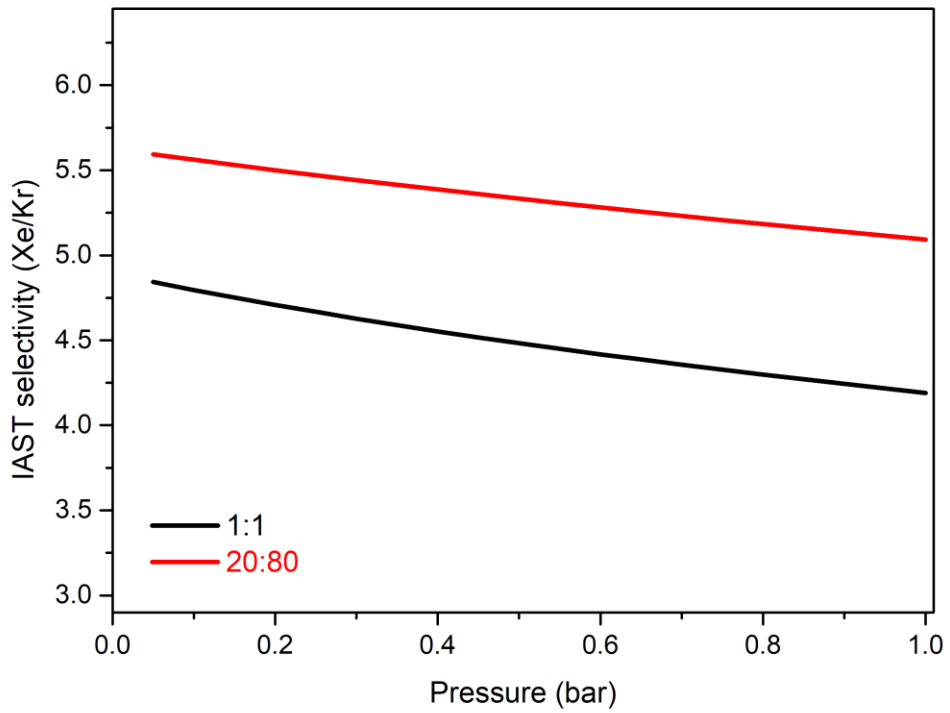

Figure S42. IAST selectivity of Xe and Kr (1:1 and 20:80 gas mixtures), calculated at 1 bar and 293K for **[Co(H₂mdp)(Ni(CN)₄)]**.

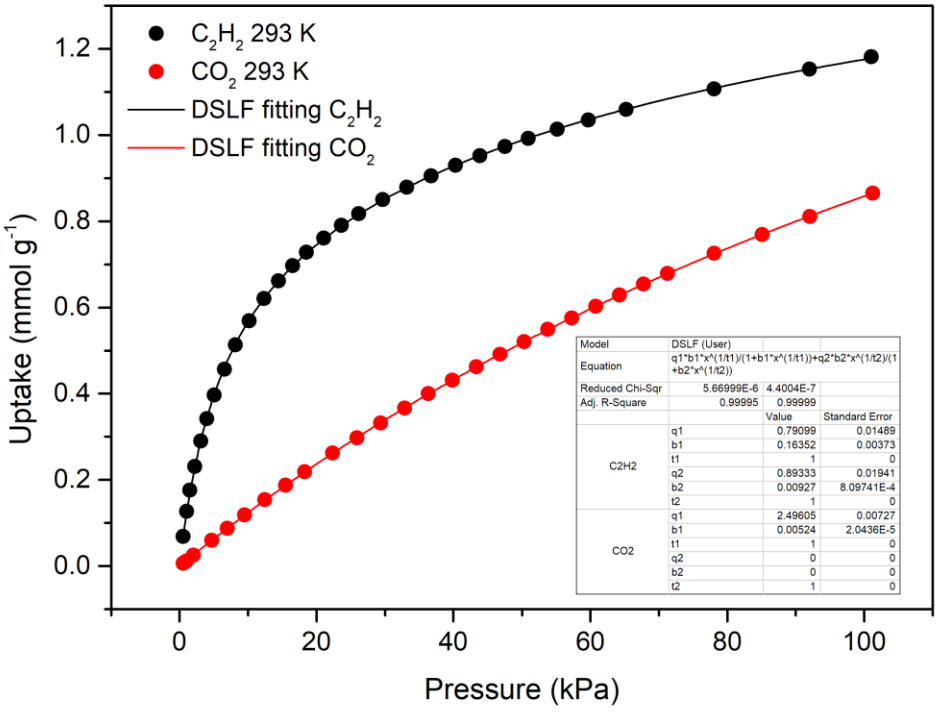

Model	DSLF (User)		
Equation	q1*b1*x^(1/t1)/(1+b1*x^(1/t1))+q2*b2*x^(1/t2)/(1+b2*x^(1/t2))		
Reduced Chi-Sqr	5.66999E-6	4.4004E-7	
Adj. R-Square	0.99995	0.99999	
		Value	Standard Error
C2H2	q1	0.79099	0.01489
	b1	0.16352	0.00373
	t1	1	0
	q2	0.89333	0.01941
	b2	0.00927	8.09741E-4
	t2	1	0
CO2	q1	2.49605	0.00727
	b1	0.00524	2.0436E-5
	t1	1	0
	q2	0	0
	b2	0	0
	t2	1	0

Figure S43. Langmuir fitting parameters of C_2H_2 and CO_2 for **[Co(H₂mdp)(Ni(CN)₄)]**.

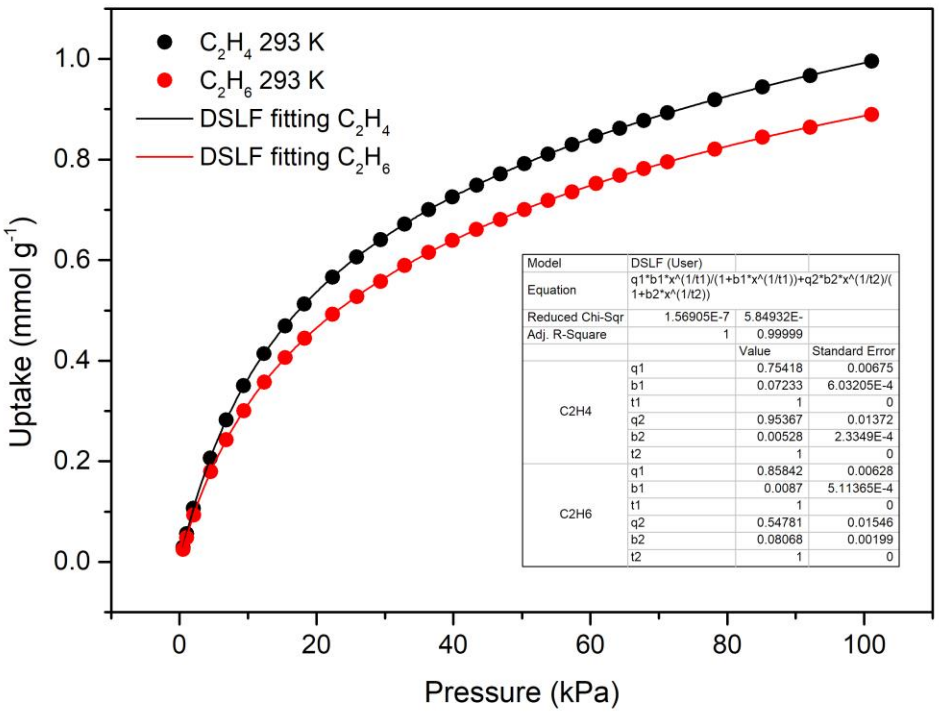

Model	DSLF (User)		
Equation	q1*b1*x^(1/t1)/(1+b1*x^(1/t1))+q2*b2*x^(1/t2)/(1+b2*x^(1/t2))		
Reduced Chi-Sqr	1.56905E-7	5.84932E-	
Adj. R-Square	1	0.99999	
		Value	Standard Error
C2H4	q1	0.75418	0.00675
	b1	0.07233	6.03205E-4
	t1	1	0
	q2	0.95367	0.01372
	b2	0.00528	2.3349E-4
	t2	1	0
C2H6	q1	0.85842	0.00628
	b1	0.0087	5.11365E-4
	t1	1	0
	q2	0.54781	0.01546
	b2	0.08068	0.00199
	t2	1	0

Figure S44. Langmuir fitting parameters of C_2H_4 and C_2H_6 for **[Co(H₂mdp)(Ni(CN)₄)]**.

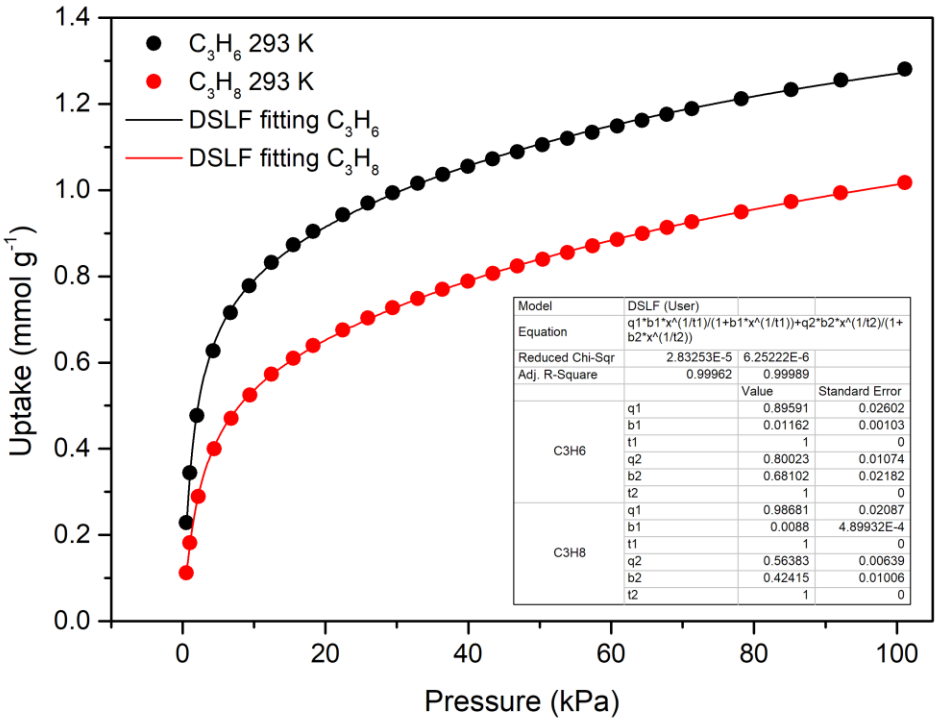

Model	DSLF (User)		
Equation	q1*b1*x^(1/t1)/(1+b1*x^(1/t1))+q2*b2*x^(1/t2)/(1+b2*x^(1/t2))		
Reduced Chi-Sqr	2.83253E-5	6.25222E-6	
Adj. R-Square	0.99962	0.99989	
		Value	Standard Error
C3H6	q1	0.89591	0.02602
	b1	0.01162	0.00103
	t1	1	0
	q2	0.80023	0.01074
	b2	0.68102	0.02182
	t2	1	0
C3H8	q1	0.98681	0.02087
	b1	0.0088	4.89932E-4
	t1	1	0
	q2	0.56383	0.00639
	b2	0.42415	0.01006
	t2	1	0

Figure S45. Langmuir fitting parameters of C_3H_6 and C_3H_8 for **[Co(H₂mdp)(Ni(CN)₄)]**.

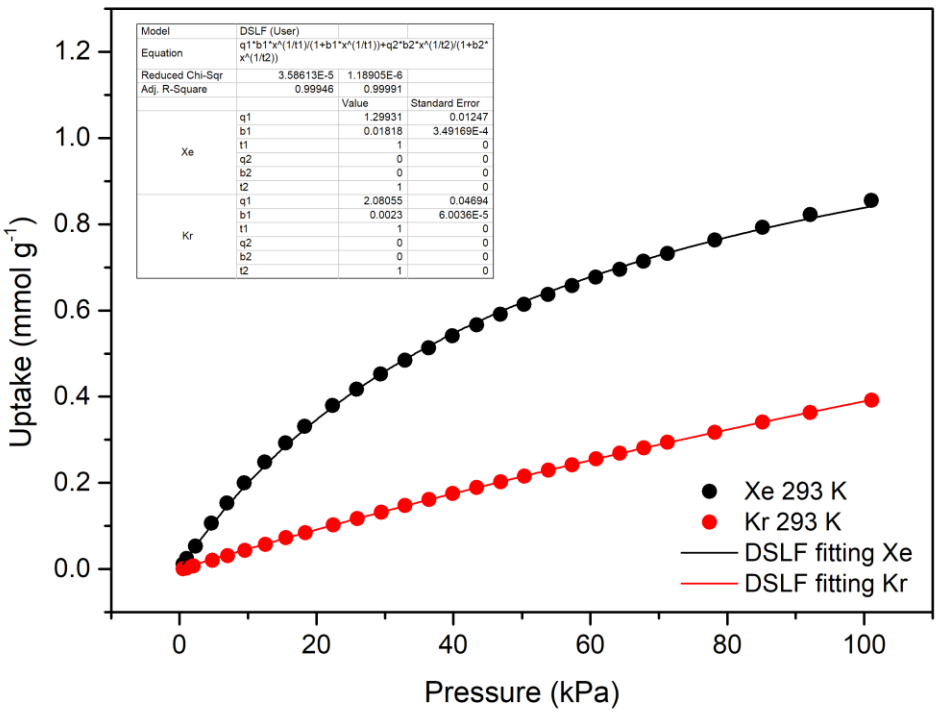

Model	DSLF (User)		
Equation	q1*b1*x^(1/t1)/(1+b1*x^(1/t1))+q2*b2*x^(1/t2)/(1+b2*x^(1/t2))		
Reduced Chi-Sqr	3.58613E-5	1.18905E-6	
Adj. R-Square	0.99946	0.99991	
		Value	Standard Error
Xe	q1	1.29931	0.01247
	b1	0.01818	3.49169E-4
	t1	1	0
	q2	0	0
	b2	0	0
	t2	1	0
Kr	q1	2.08055	0.04694
	b1	0.0023	6.0036E-5
	t1	1	0
	q2	0	0
	b2	0	0
	t2	1	0

Figure S46. Langmuir fitting parameters of Xe and Kr for **[Co(H₂mdp)(Ni(CN)₄)]**.

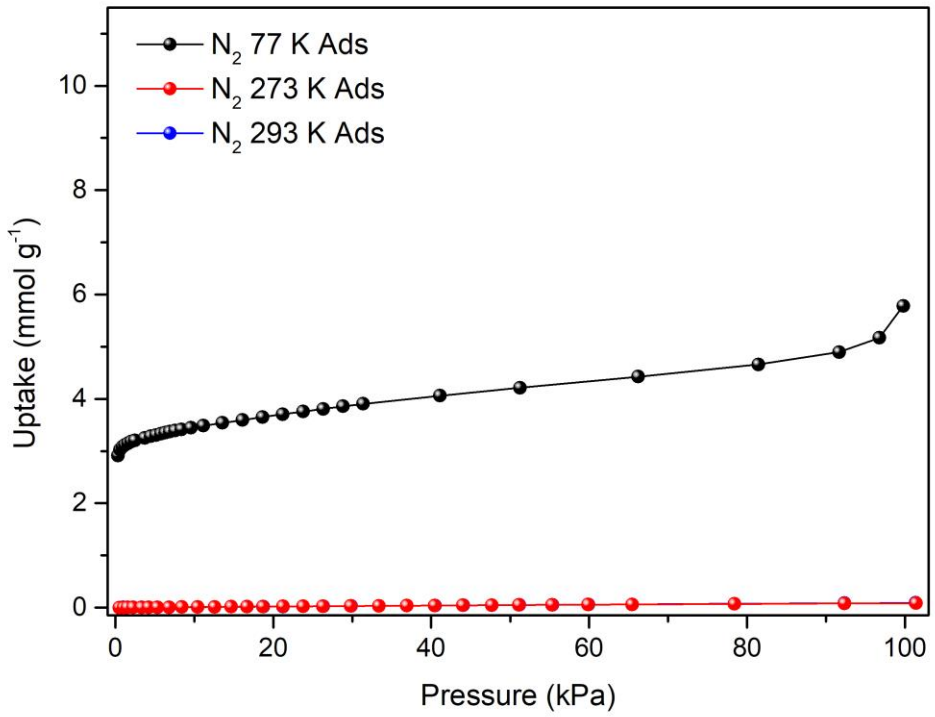

Figure S47. N_2 adsorption isotherms of **[Fe(H₂mdp)(Ni(CN)₄)]** at 77 K, 273 K and 293 K.

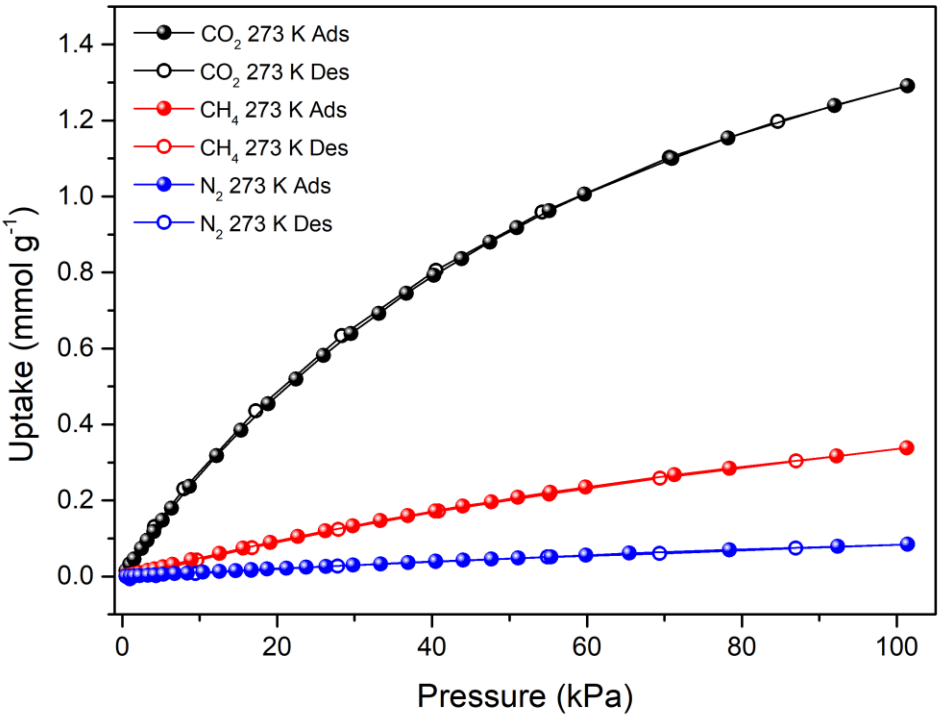

Figure S48. Adsorption isotherms of CO_2, CH_4 and N_2 for **[Fe(H₂mdp)(Ni(CN)₄)]** at 273 K.

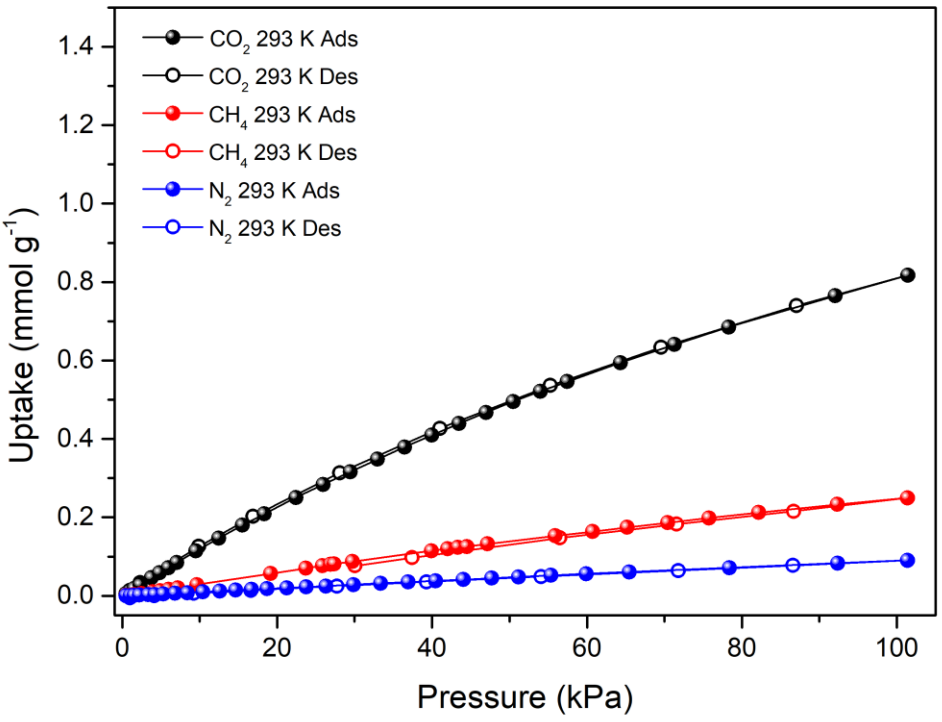

Figure S49. Adsorption isotherms of CO_2, CH_4 and N_2 for **[Fe(H₂mdp)(Ni(CN)₄)]** at 293 K.

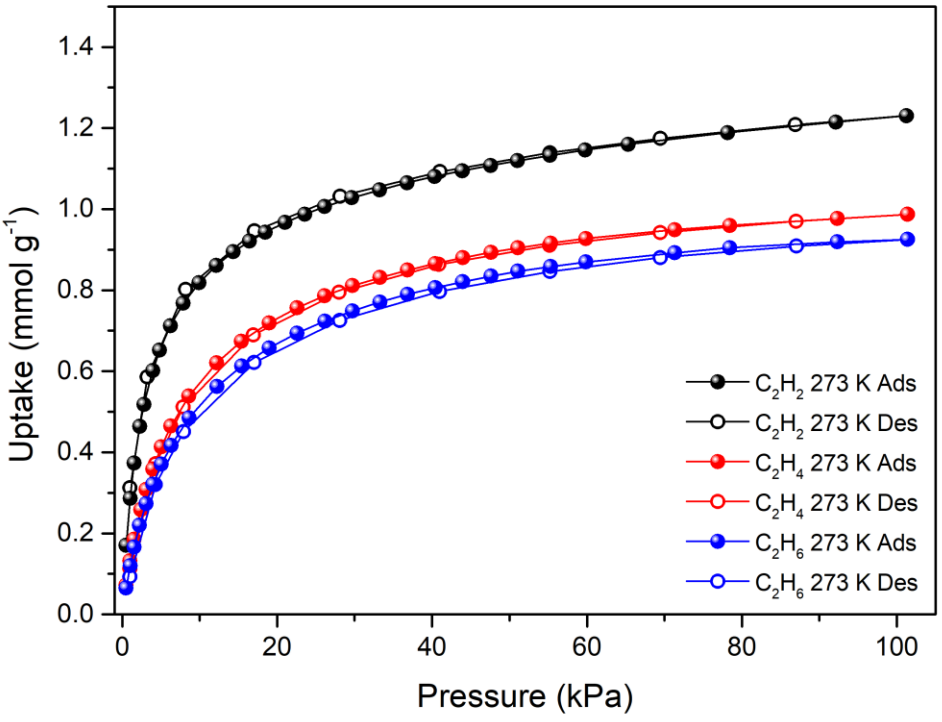

Figure S50. Adsorption isotherms of C_2H_2, C_2H_4 and C_2H_6 for **[Fe(H₂mdp)(Ni(CN)₄)]** at 273 K.

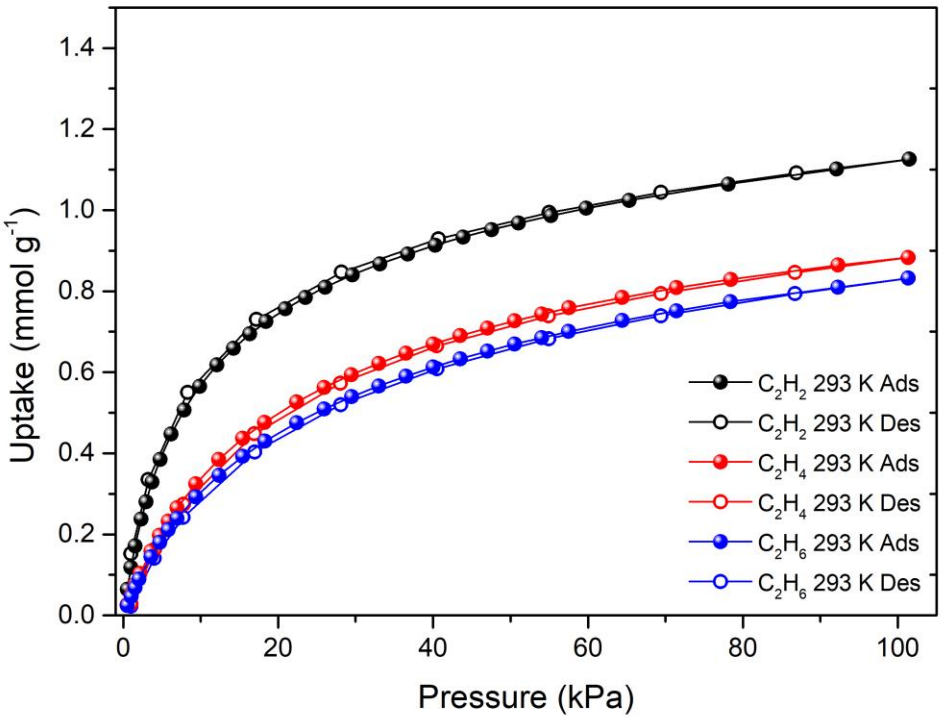

Figure S51. Adsorption isotherms of C_2H_2, C_2H_4 and C_2H_6 for **[Fe(H₂mdp)(Ni(CN)₄)]** at 293 K.

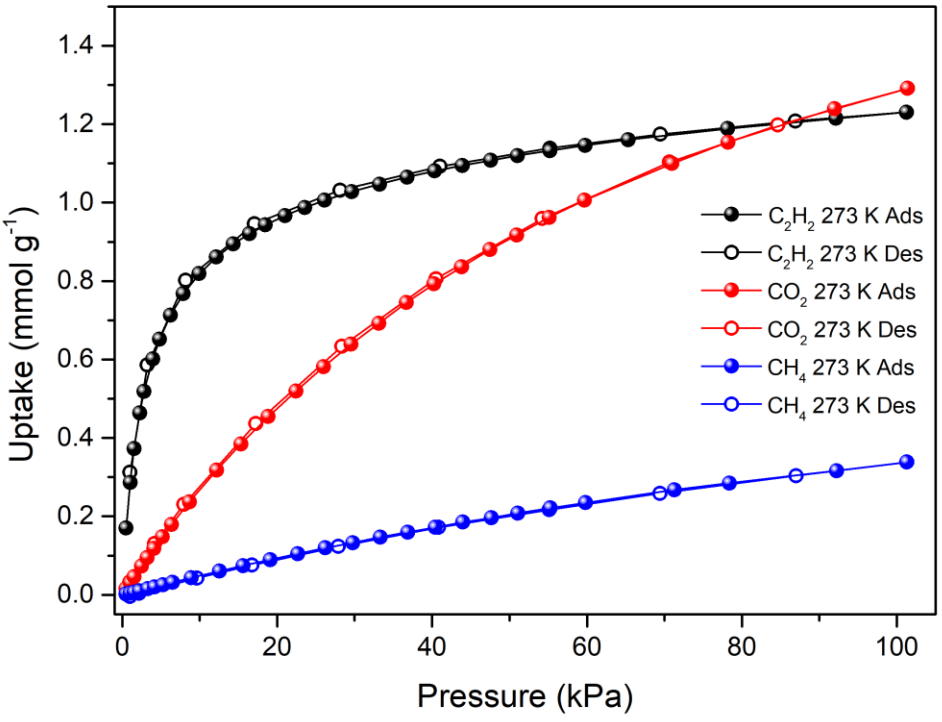

Figure S52. C_2H_2, CO_2 and CH_4 adsorption isotherms for **[Fe(H₂mdp)(Ni(CN)₄)]** at 273 K.

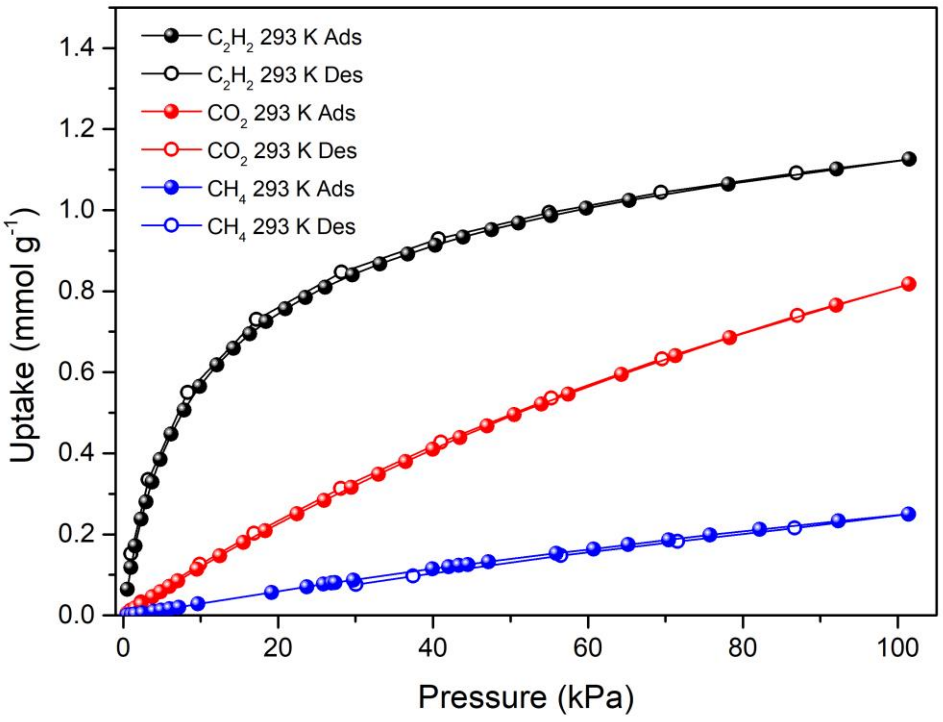

Figure S53. C_2H_2, CO_2 and CH_4 adsorption isotherms for **[Fe(H₂mdp)(Ni(CN)₄)]** at 293 K.

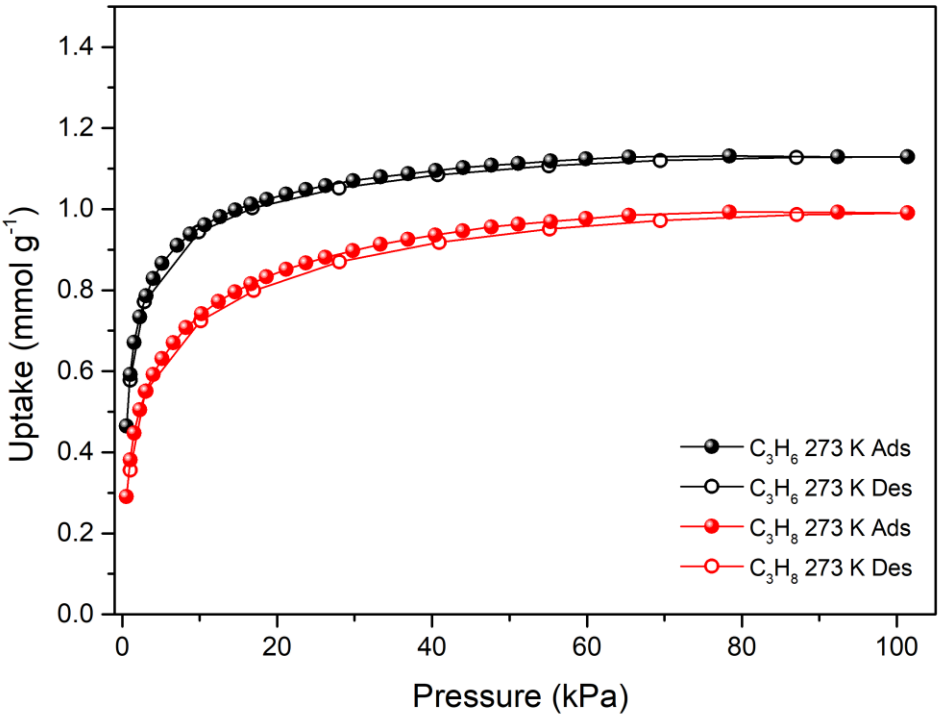

Figure S54. C_3H_6 and C_3H_8 adsorption isotherms for **[Fe(H₂mdp)(Ni(CN)₄)]** at 273 K.

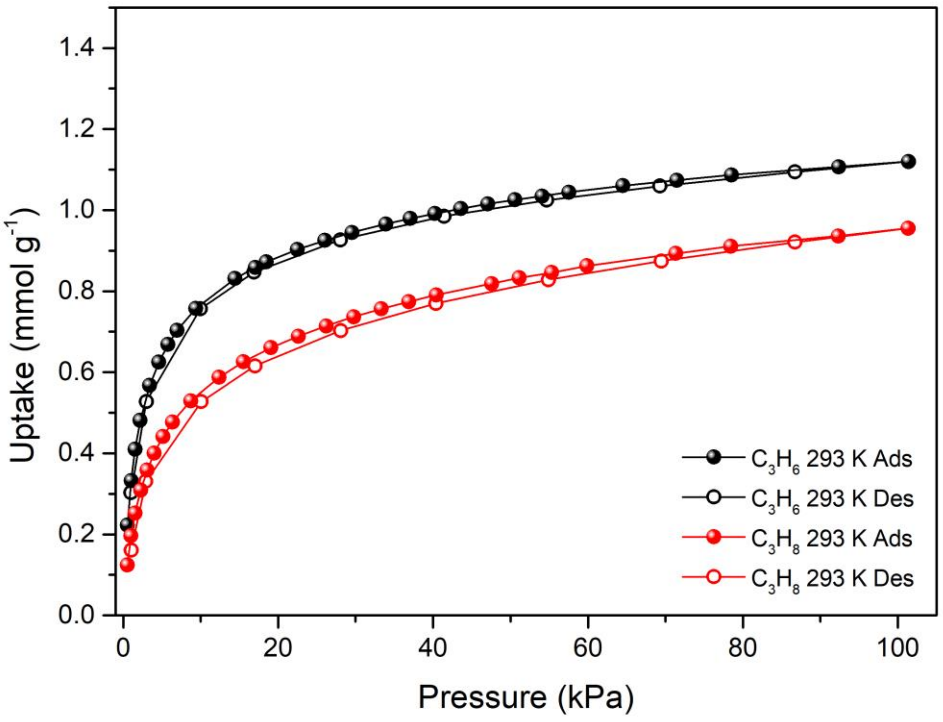

Figure S55. C_3H_6 and C_3H_8 adsorption isotherms for **[Fe(H₂mdp)(Ni(CN)₄)]** at 293 K.

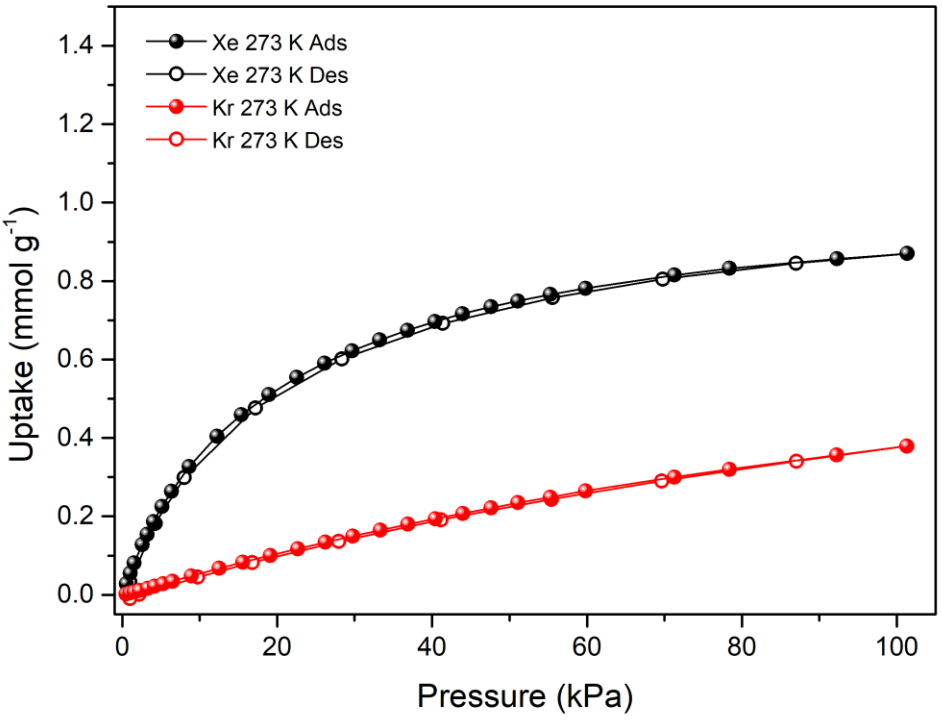

Figure S56. Xe and Kr adsorption isotherms for **[Fe(H₂mdp)(Ni(CN)₄)]** at 273 K.

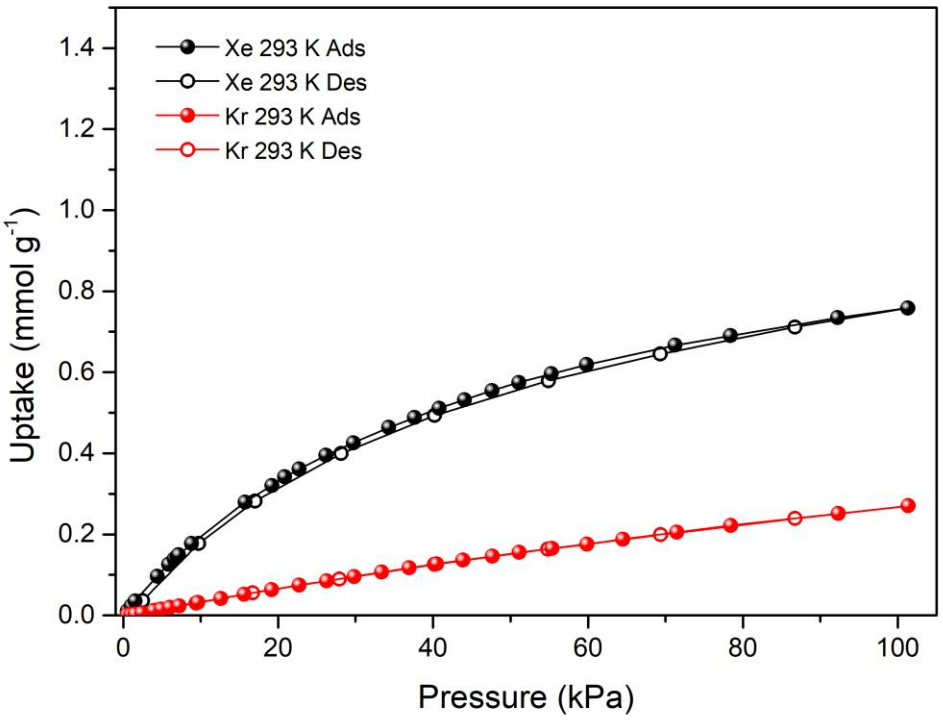

Figure S57. Xe and Kr adsorption isotherms for **[Fe(H₂mdp)(Ni(CN)₄)]** at 293 K.

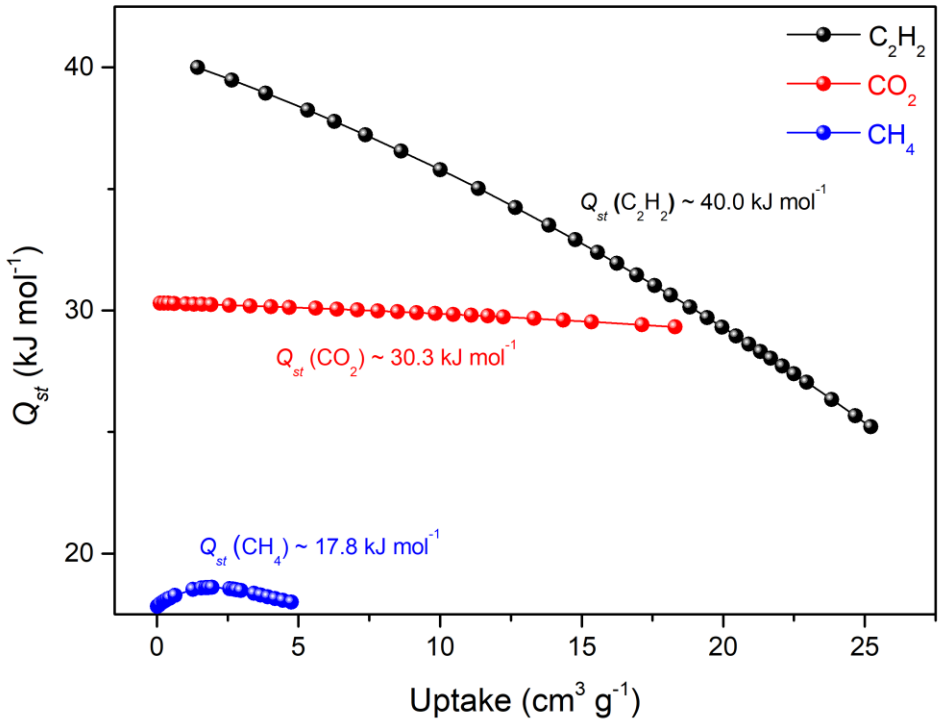

Figure S58. Isosteric heats of adsorption for C_2H_2, CO_2 and CH_4 for **[Fe(H₂mdp)(Ni(CN)₄)]**.

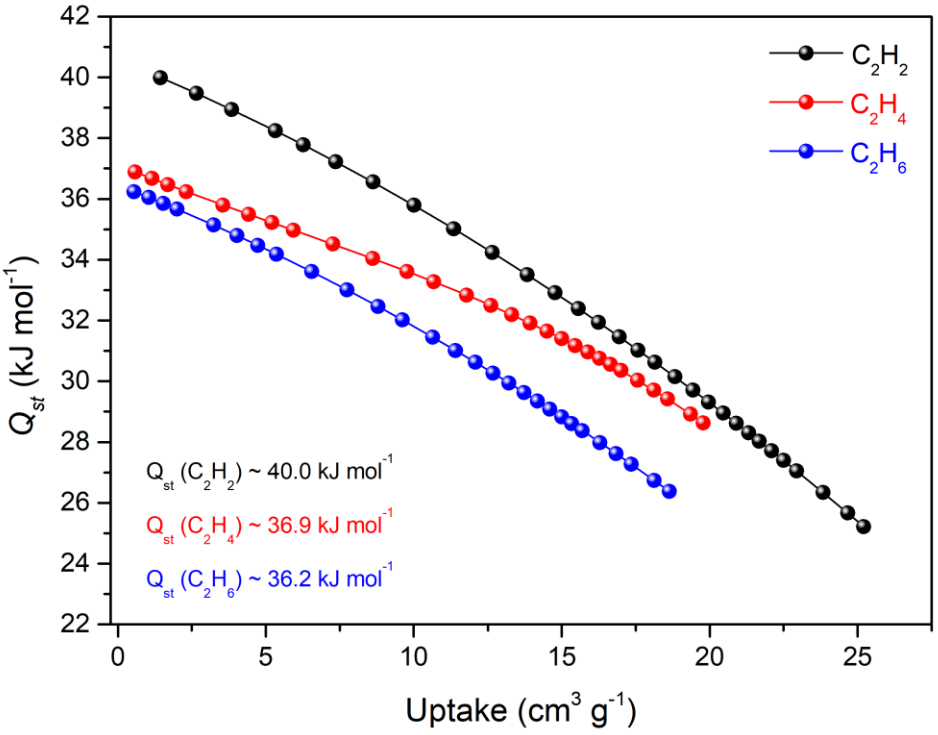

Figure S59. C_2H_2, C_2H_4 and C_2H_6 isosteric heats of adsorption for **[Fe(H₂mdp)(Ni(CN)₄)]**.

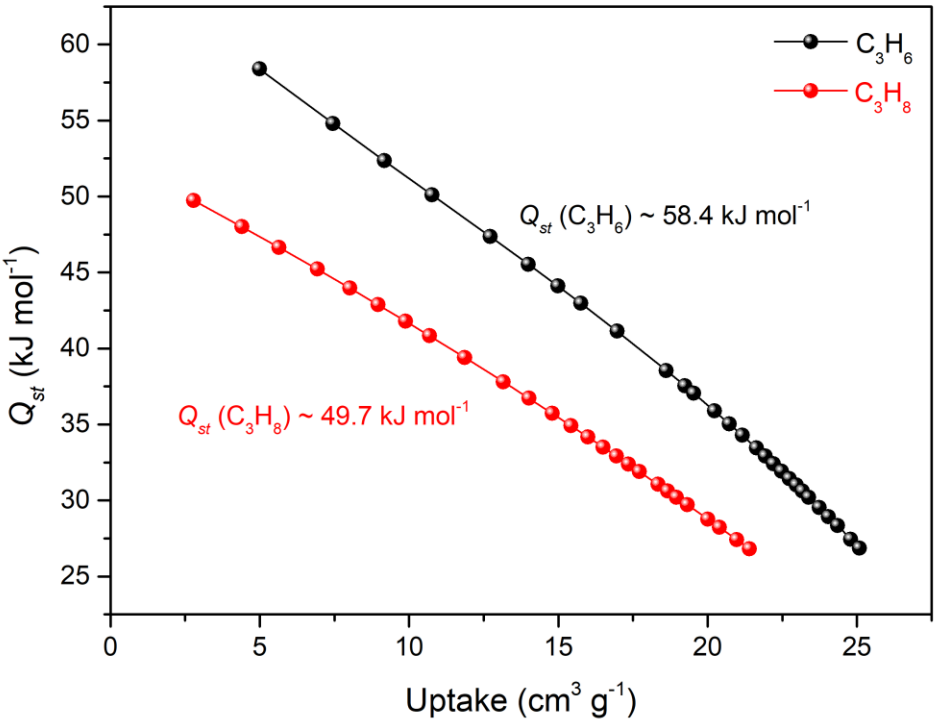

Figure S60. Isosteric heats of adsorption for C_3H_6, and C_3H_8 for **[Fe(H₂mdp)(Ni(CN)₄)]**.

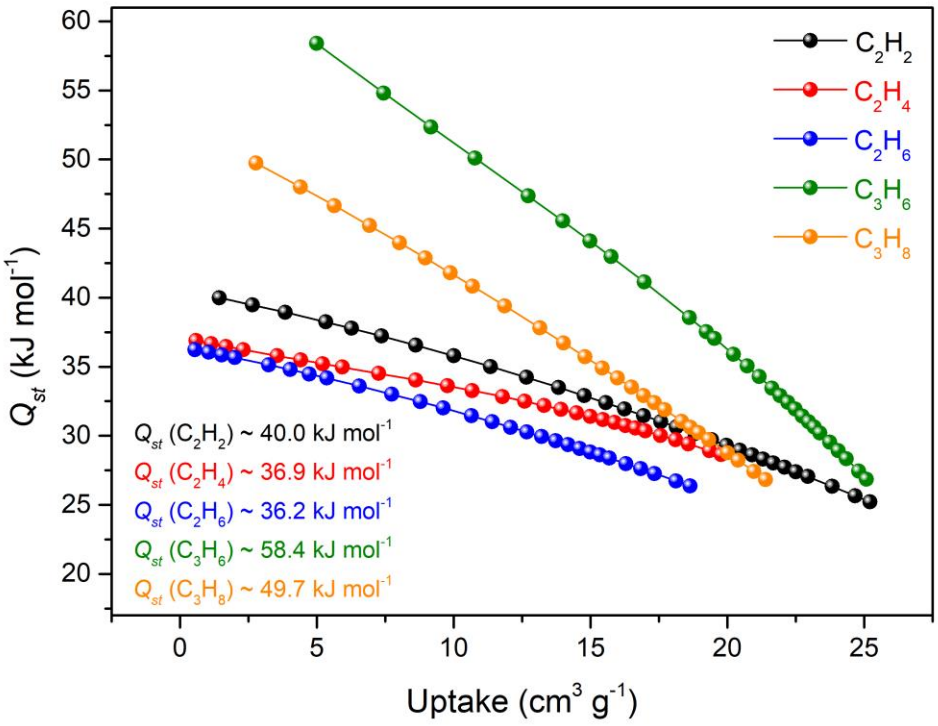

Figure S61. Isosteric heats of adsorption for C2 and C3 gases for **[Fe(H₂mdp)(Ni(CN)₄)]**.

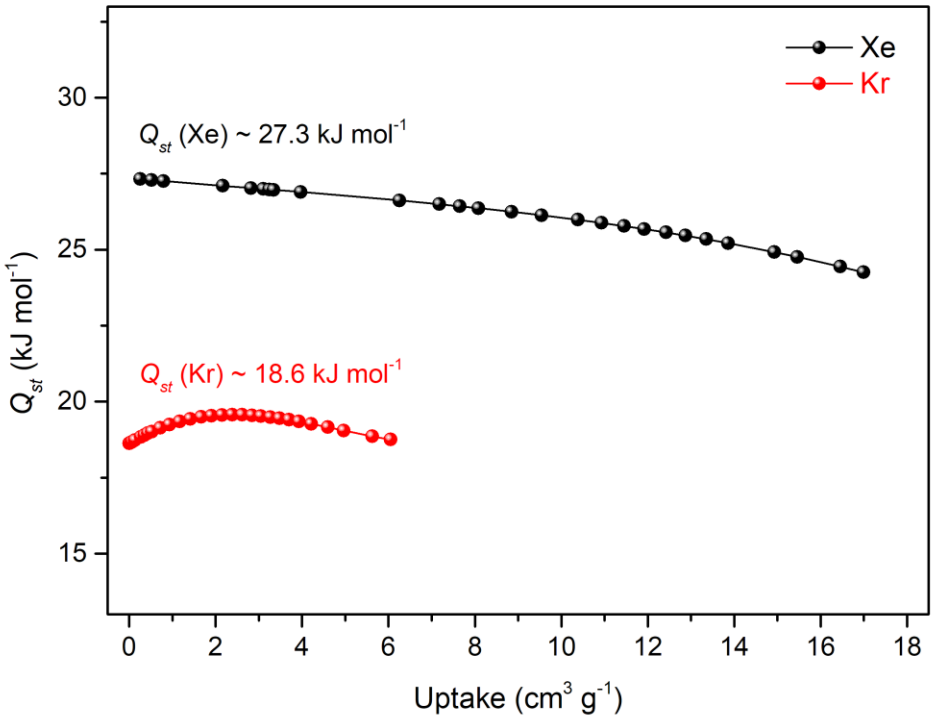

Figure S62. Isosteric heats of adsorption for Xe and Kr for **[Fe(H₂mdp)(Ni(CN)₄)]**.

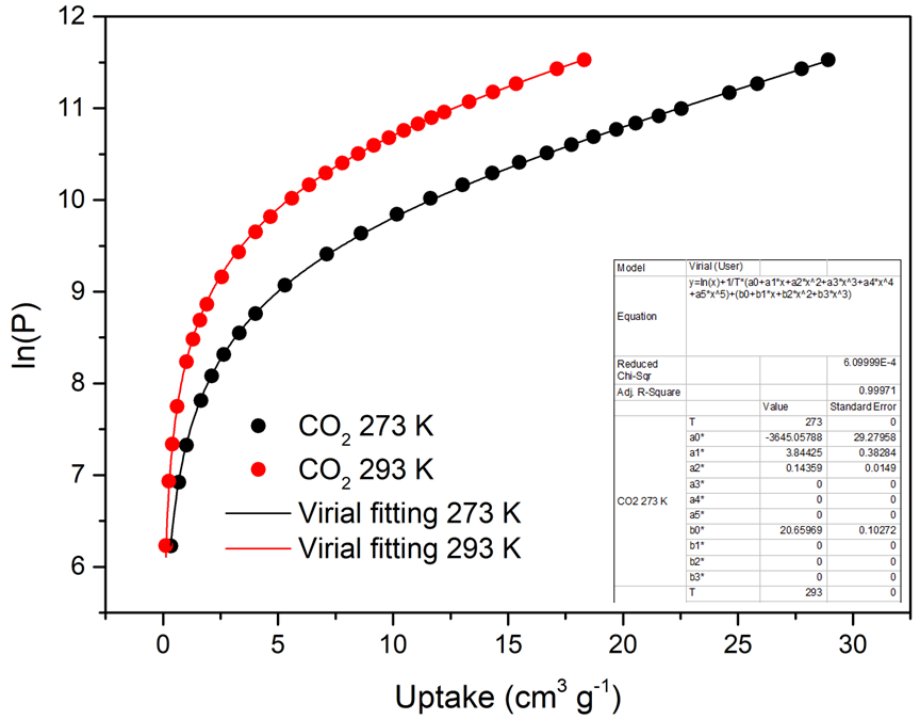

Figure S63. Virial fitting of the CO_2 adsorption isotherms for **[Fe(H₂mdp)(Ni(CN)₄)]**.

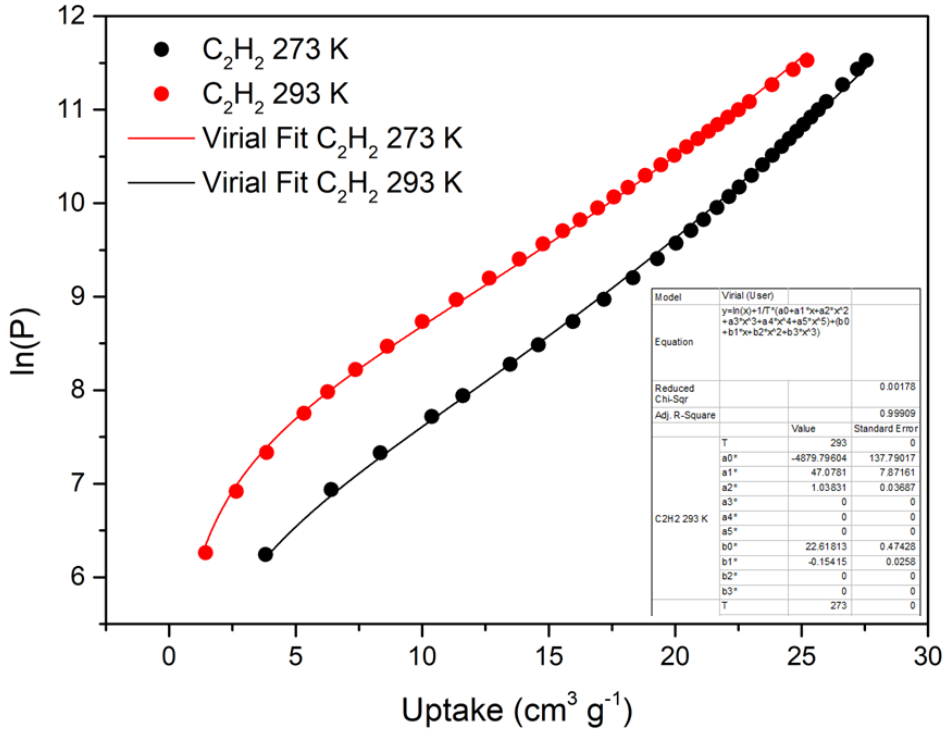

Figure S64. Virial fitting of the C_2H_2 adsorption isotherms for **[Fe(H₂mdp)(Ni(CN)₄)]**.

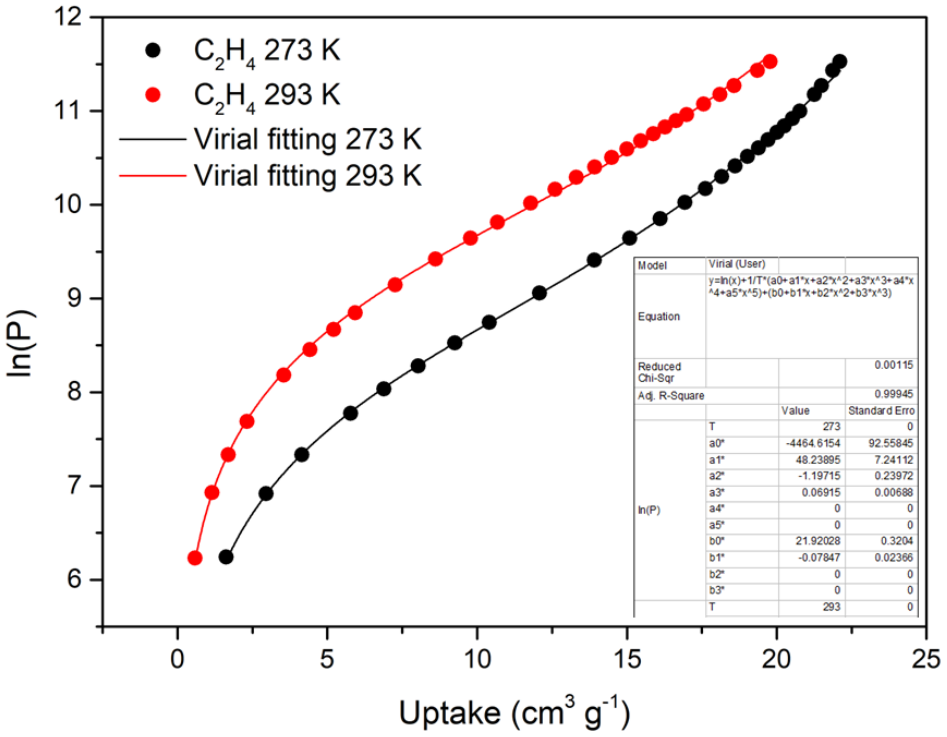

Figure S65. Virial fitting of the C_2H_4 adsorption isotherms for **[Fe(H₂mdp)(Ni(CN)₄)]**.

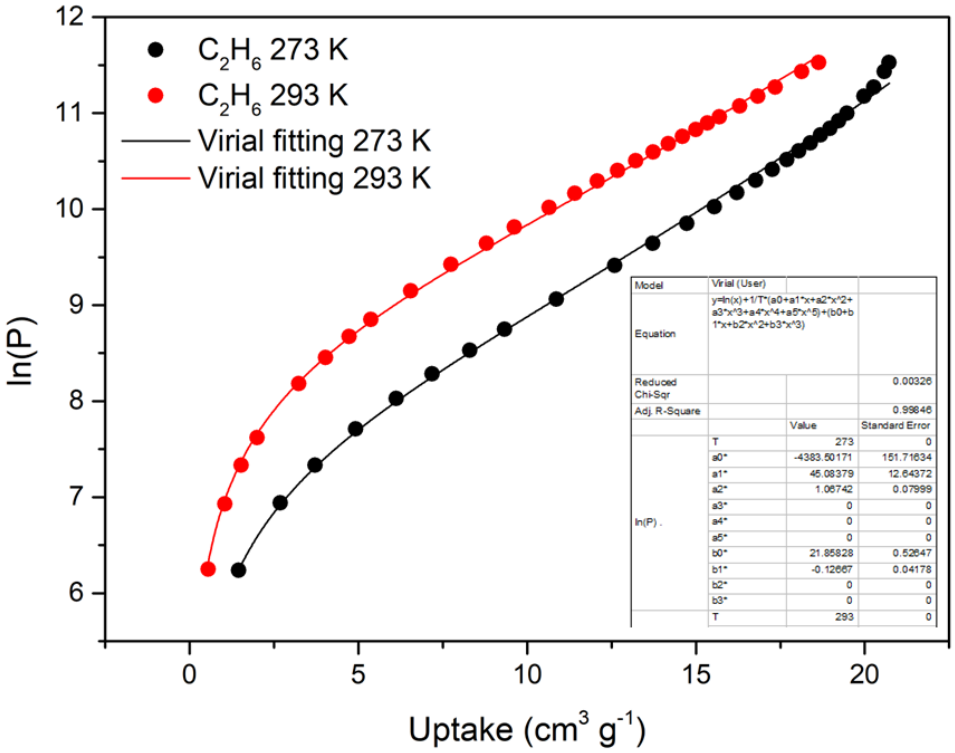

Figure S66. Virial fitting of the C_2H_6 adsorption isotherms for **[Fe(H₂mdp)(Ni(CN)₄)]**.

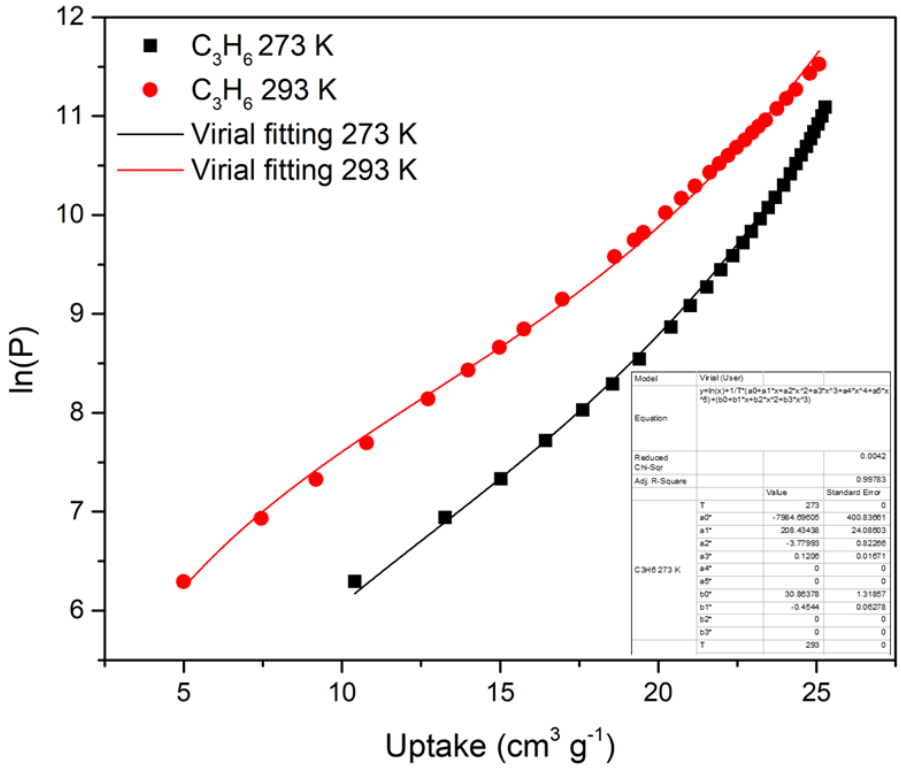

Figure S67. Virial fitting of the C_3H_6 adsorption isotherms for **[Fe(H₂mdp)(Ni(CN)₄)]**.

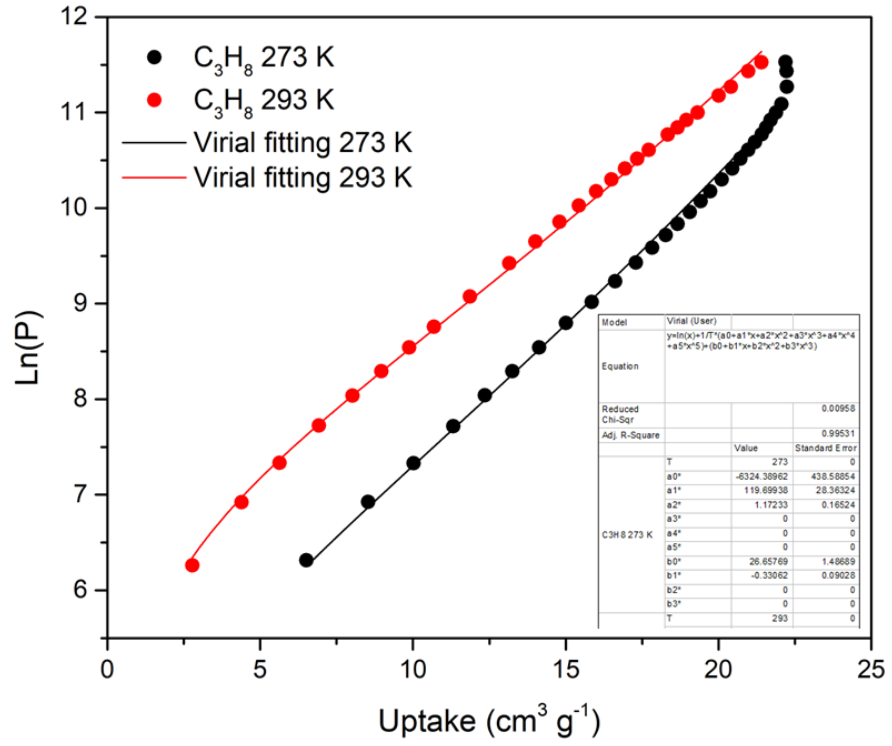

Figure S68. Virial fitting of the C_3H_8 adsorption isotherms for **[Fe(H₂mdp)(Ni(CN)₄)]**.

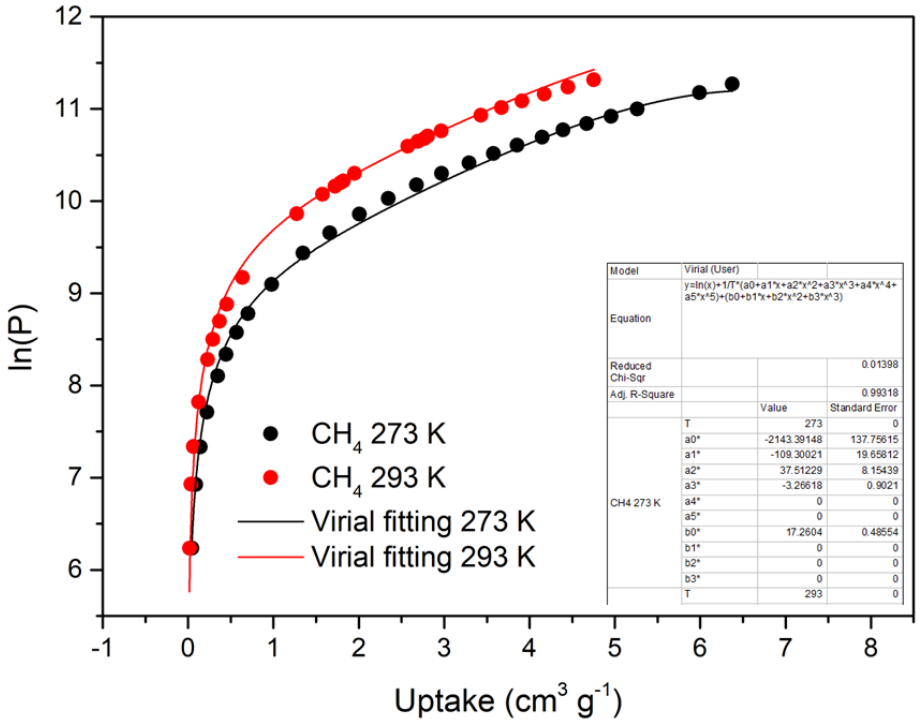

Figure S69. Virial fitting of the CH_4 adsorption isotherms for **[Fe(H₂mdp)(Ni(CN)₄)]**.

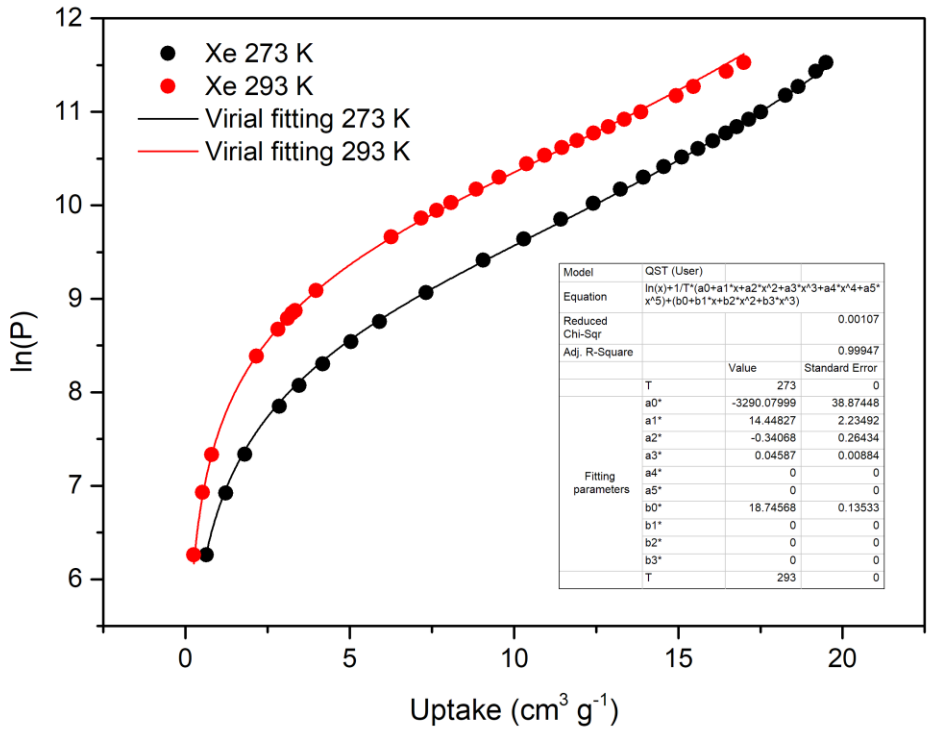

Figure S70. Virial fitting of the Xe adsorption isotherms for **[Fe(H₂mdp)(Ni(CN)₄)]**.

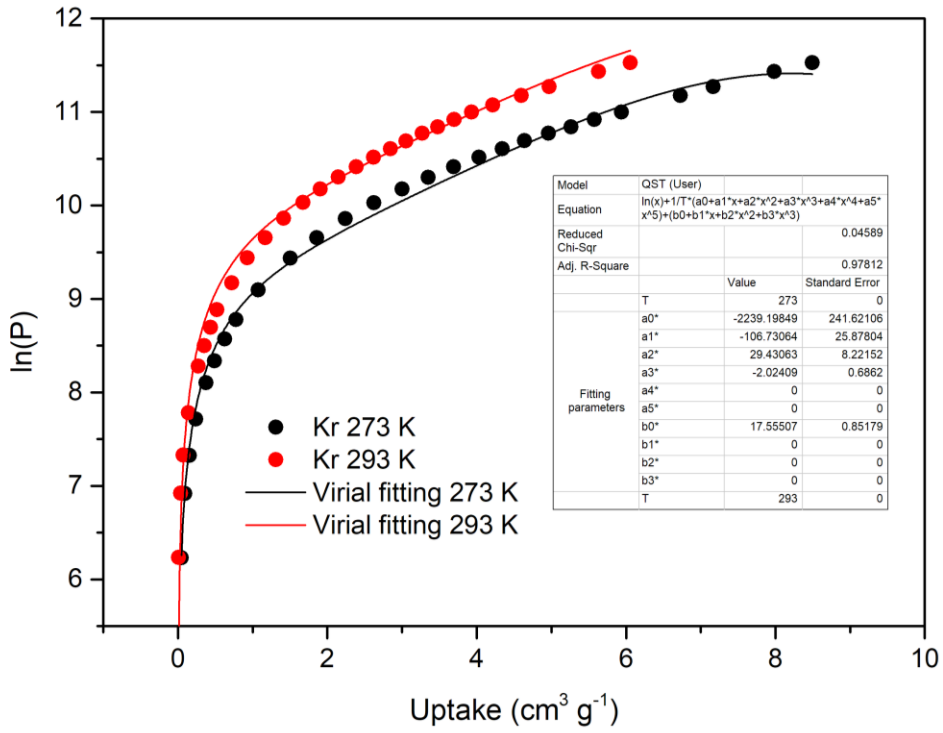

Figure S71. Virial fitting of the Kr adsorption isotherms for **[Fe(H$_2$mdp)(Ni(CN)$_4$)]**.

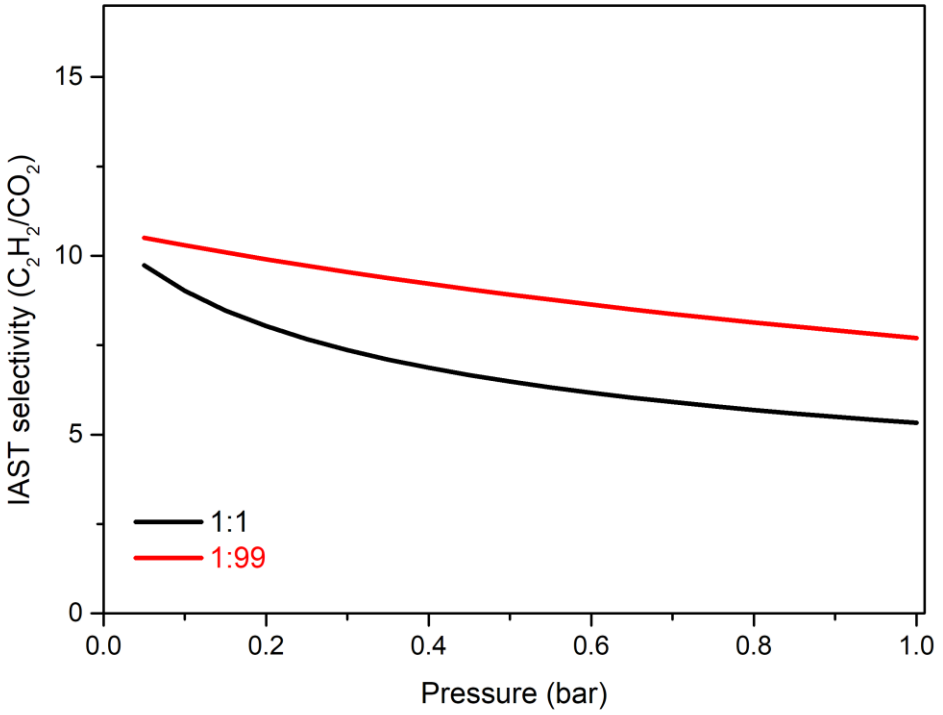

Figure S72. IAST selectivity of C_2H_2 and CO_2 (1:1 and 1:99 gas mixtures), calculated at 1 bar and 293K for **[Fe(H$_2$mdp)(Ni(CN)$_4$)]**.

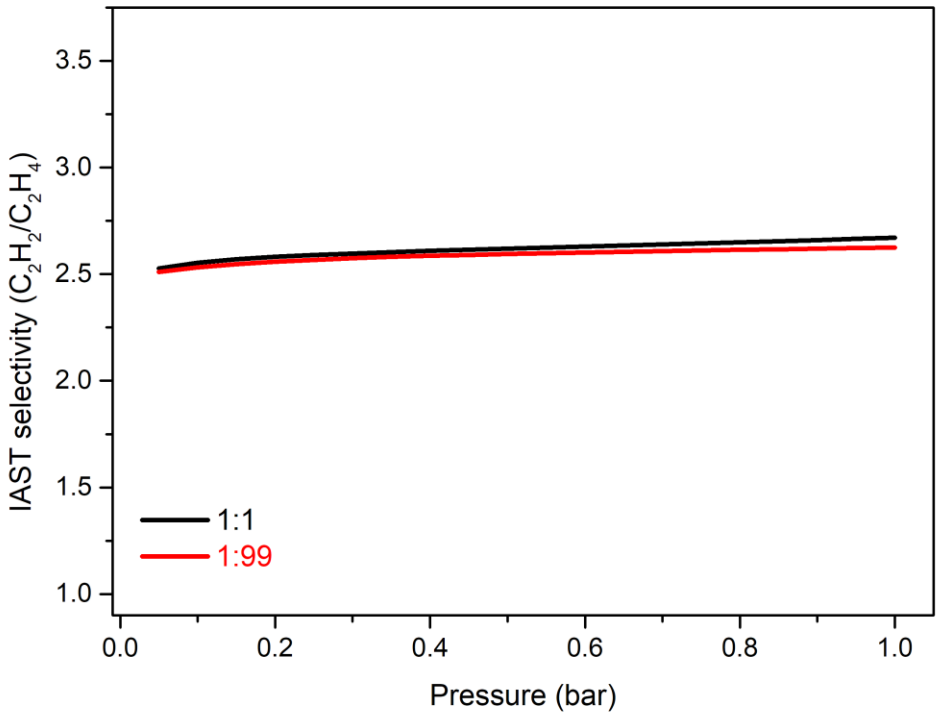

Figure S73. IAST selectivity of C_2H_2 and C_2H_4 (1:1 and 1:99 gas mixtures), calculated at 1 bar and 293K for **[Fe(H₂mdp)(Ni(CN)₄)]**.

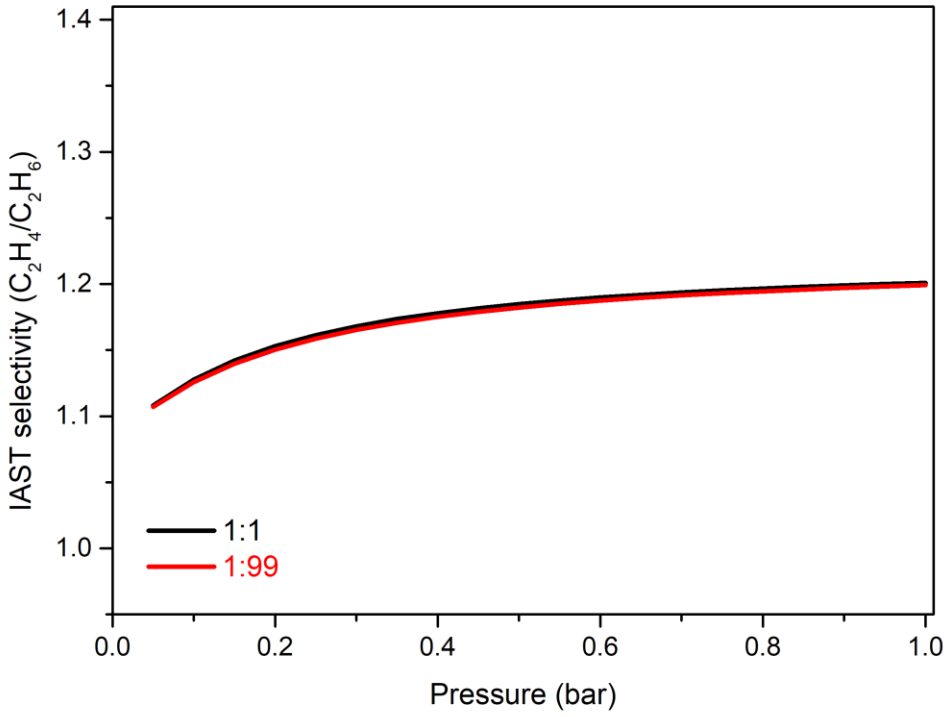

Figure S74. IAST selectivity of C_2H_4 and C_2H_6 (1:1 and 1:99 gas mixtures), calculated at 1 bar and 293K for **[Fe(H₂mdp)(Ni(CN)₄)]**.

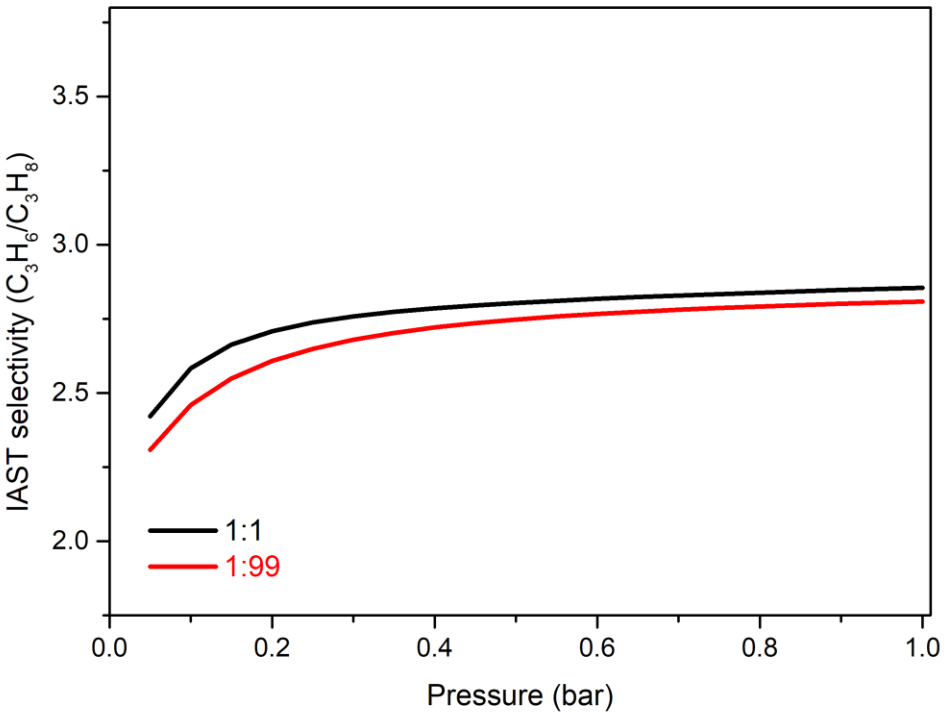

Figure S75. IAST selectivity of C_3H_6 and C_3H_8 (1:1 and 1:99 gas mixtures), calculated at 1 bar and 293K for **[Fe(H₂mdp)(Ni(CN)₄)]**.

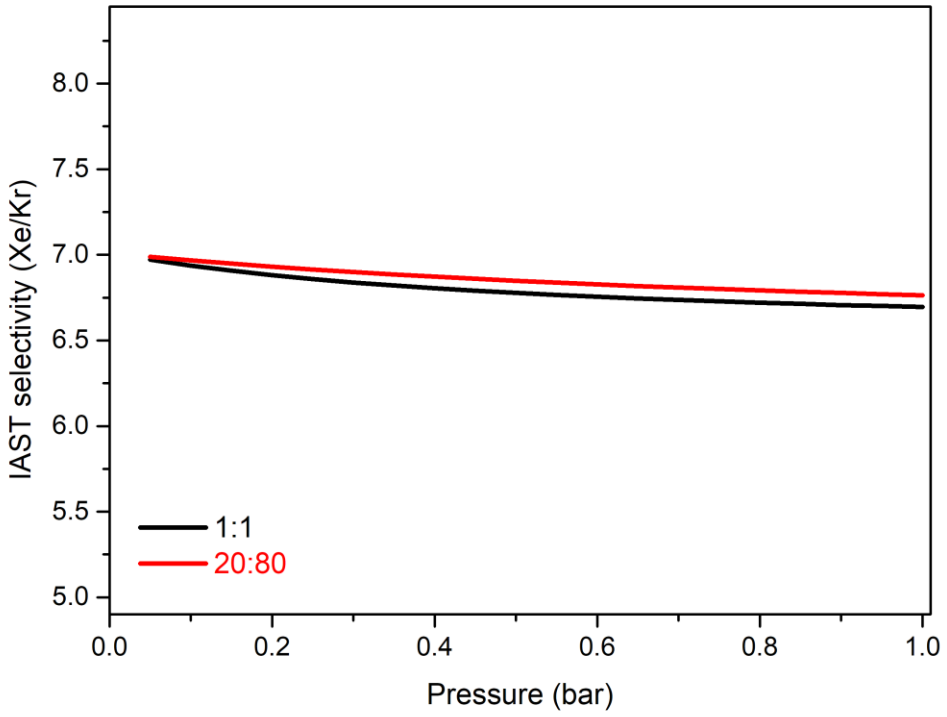

Figure S76. IAST selectivity of Xe and Kr (1:1 and 20:80 gas mixtures), calculated at 1 bar and 293K for **[Fe(H₂mdp)(Ni(CN)₄)]**.

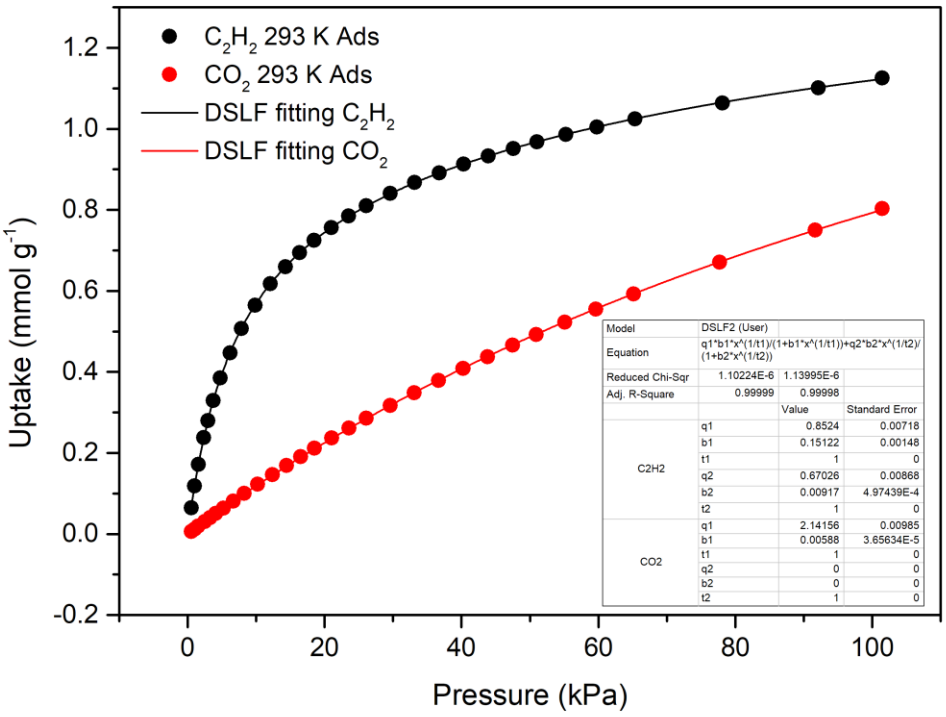

Model	DSLF2 (User)		
Equation	q1*b1*x^(1/t1)/(1+b1*x^(1/t1))+q2*b2*x^(1/t2)/(1+b2*x^(1/t2))		
Reduced Chi-Sqr	1.10224E-6	1.13995E-6	
Adj. R-Square	0.99999	0.99998	
		Value	Standard Error
C2H2	q1	0.8524	0.00718
	b1	0.15122	0.00148
	t1	1	0
	q2	0.67026	0.00868
	b2	0.00917	4.97439E-4
	t2	1	0
CO2	q1	2.14156	0.00985
	b1	0.00588	3.65634E-5
	t1	1	0
	q2	0	0
	b2	0	0
	t2	1	0

Figure S77. Langmuir fitting parameters of C_2H_2 and CO_2 for **[Fe(H₂mdp)(Ni(CN)₄)]**.

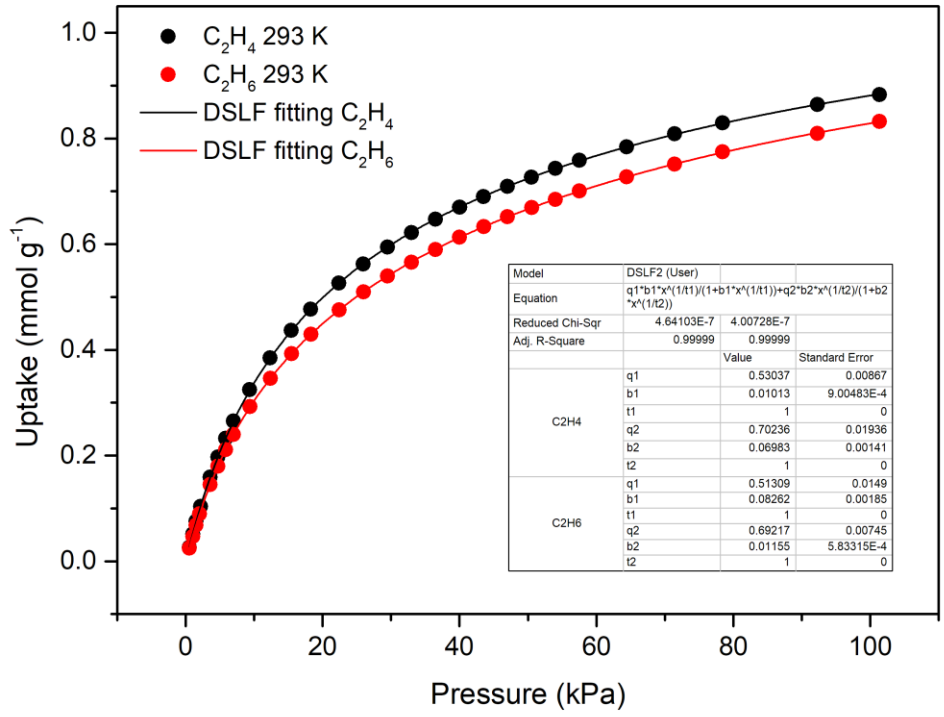

Model	DSLF2 (User)		
Equation	q1*b1*x^(1/t1)/(1+b1*x^(1/t1))+q2*b2*x^(1/t2)/(1+b2*x^(1/t2))		
Reduced Chi-Sqr	4.64103E-7	4.00728E-7	
Adj. R-Square	0.99999	0.99999	
		Value	Standard Error
C2H4	q1	0.53037	0.00867
	b1	0.01013	9.00483E-4
	t1	1	0
	q2	0.70236	0.01936
	b2	0.06983	0.00141
	t2	1	0
C2H6	q1	0.51309	0.0149
	b1	0.08262	0.00185
	t1	1	0
	q2	0.69217	0.00745
	b2	0.01155	5.83315E-4
	t2	1	0

Figure S78. Langmuir fitting parameters of C_2H_4 and C_2H_6 for **[Fe(H₂mdp)(Ni(CN)₄)]**.

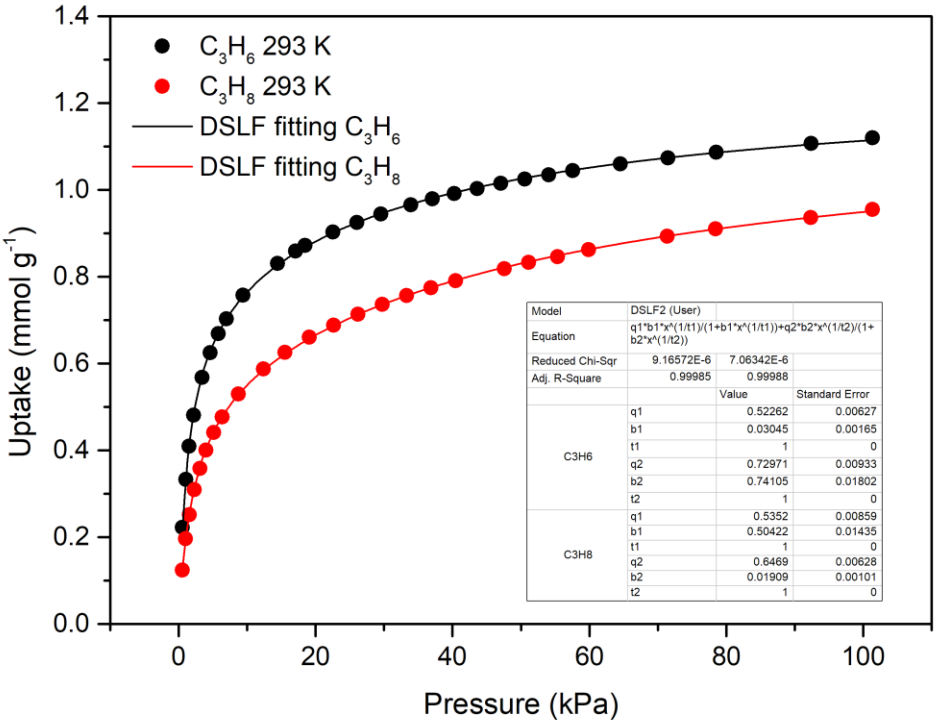

Model	DSLF2 (User)		
Equation	q1*b1*x^(1/t1)/(1+b1*x^(1/t1))+q2*b2*x^(1/t2)/(1+b2*x^(1/t2))		
Reduced Chi-Sqr	9.16572E-6	7.06342E-6	
Adj. R-Square	0.99985	0.99988	
		Value	Standard Error
C3H6	q1	0.52262	0.00627
	b1	0.03045	0.00165
	t1	1	0
	q2	0.72971	0.00933
	b2	0.74105	0.01802
	t2	1	0
C3H8	q1	0.5352	0.00859
	b1	0.50422	0.01435
	t1	1	0
	q2	0.6469	0.00628
	b2	0.01909	0.00101
	t2	1	0

Figure S79. Langmuir fitting parameters of C_3H_6 and C_3H_8 for **[Fe(H₂mdp)(Ni(CN)₄)]**.

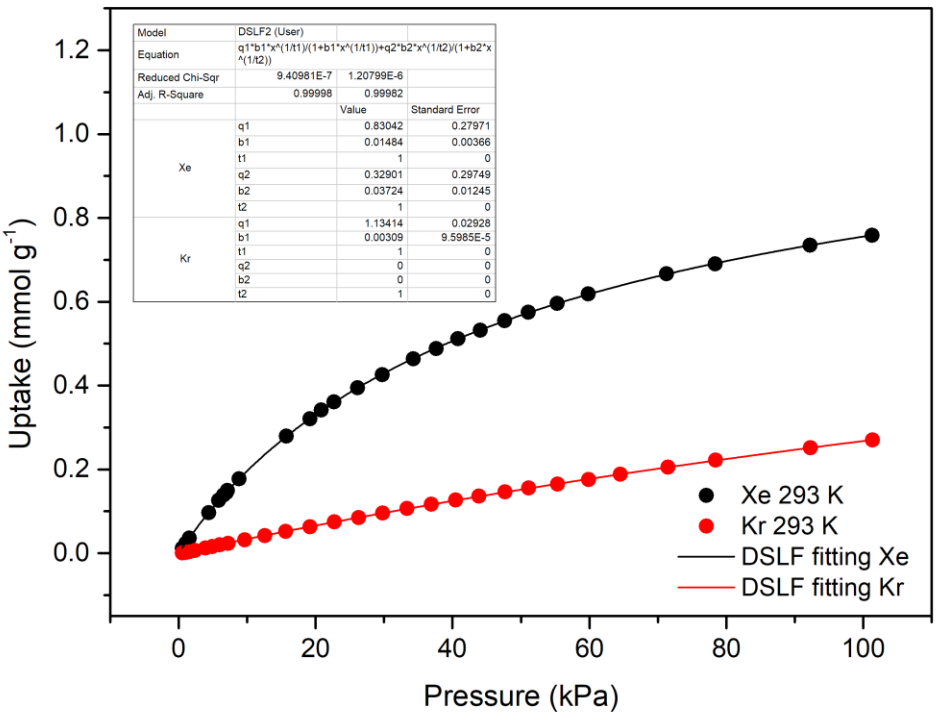

Model	DSLF2 (User)		
Equation	q1*b1*x^(1/t1)/(1+b1*x^(1/t1))+q2*b2*x^(1/t2)/(1+b2*x^(1/t2))		
Reduced Chi-Sqr	9.40981E-7	1.20799E-6	
Adj. R-Square	0.99998	0.99982	
		Value	Standard Error
Xe	q1	0.83042	0.27971
	b1	0.01484	0.00366
	t1	1	0
	q2	0.32901	0.29749
	b2	0.03724	0.01245
	t2	1	0
Kr	q1	1.13414	0.02928
	b1	0.00309	9.5985E-5
	t1	1	0
	q2	0	0
	b2	0	0
	t2	1	0

Figure S80. Langmuir fitting parameters of Xe and Kr for **[Fe(H₂mdp)(Ni(CN)₄)]**.

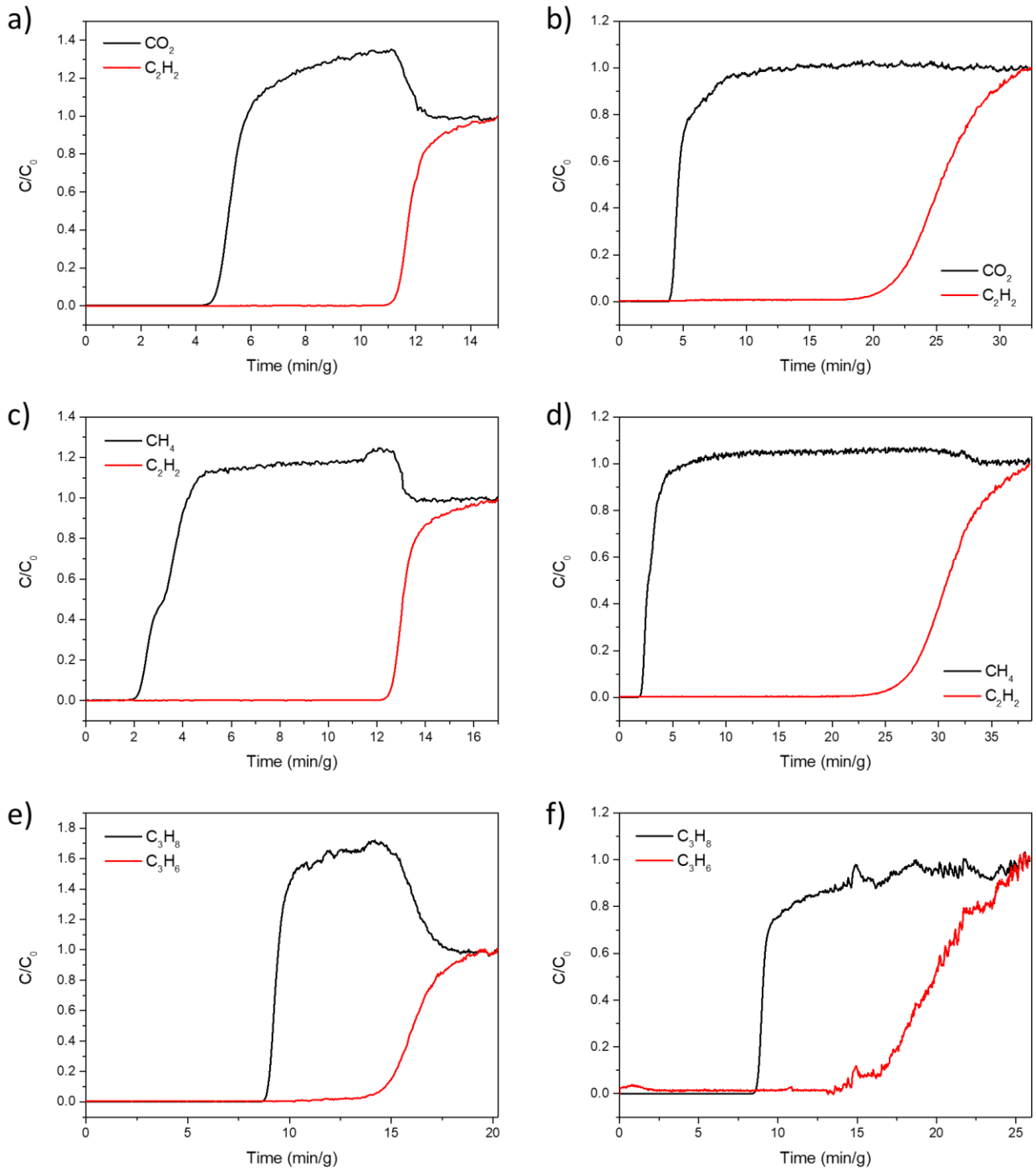

Figure S81. Dynamic column breakthrough curves for **[Co(H$_2$mdp)(Ni(CN)$_4$)]** of binary gas mixtures. a) C_2H_2/CO_2 (50/50), b) C_2H_2/CO_2 (10/90), c) C_2H_2/CH_4 (50/50), d) C_2H_2/CH_4 (10/90), e) C_3H_6/C_3H_8 (50/50) and f) C_3H_6/C_3H_8 (90/10).

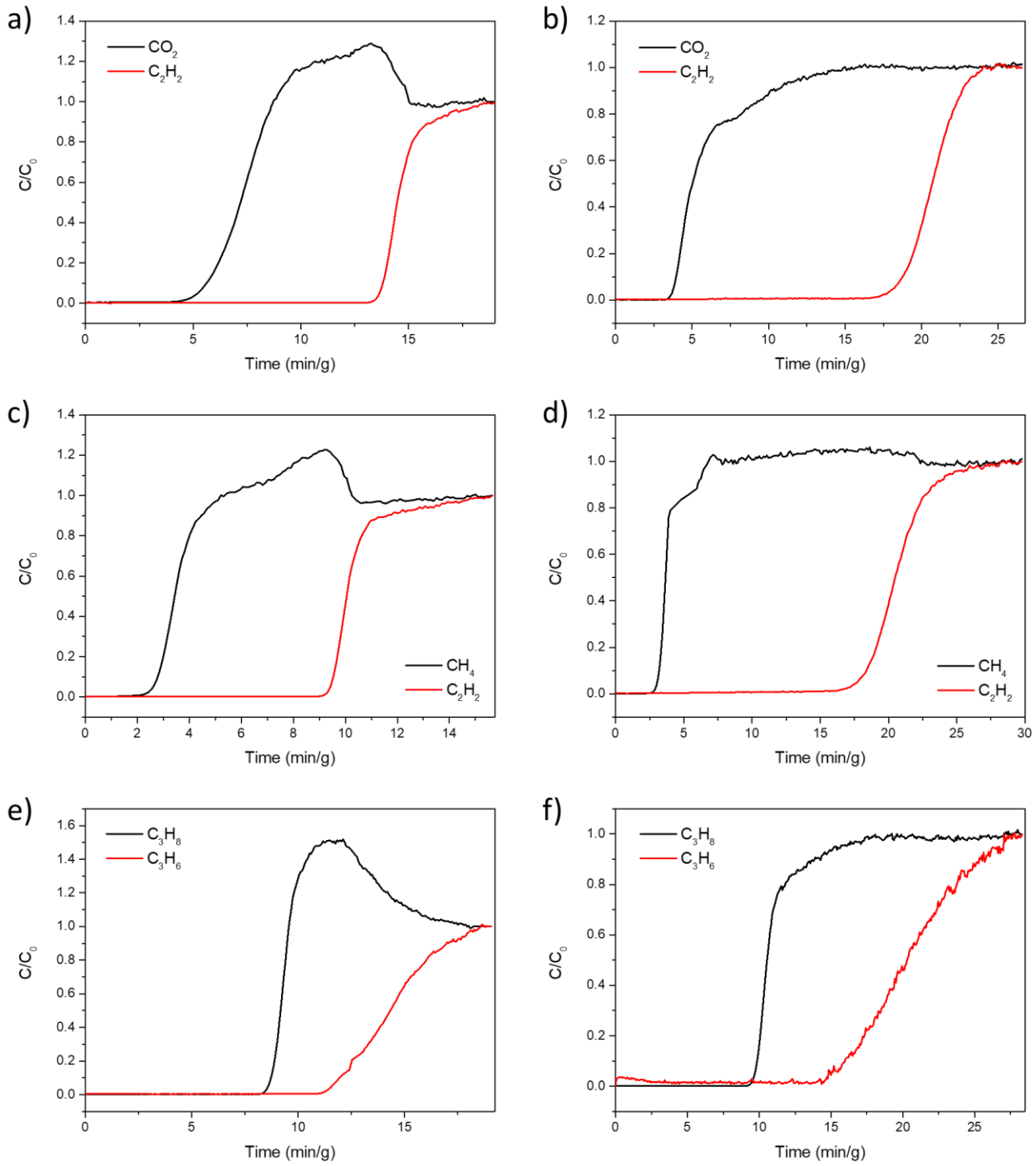

Figure S82. Dynamic column breakthrough curves for **[Fe(H₂mdp)(Ni(CN)₄)]** of binary gas mixtures. a) C_2H_2/CO_2 (50/50), b) C_2H_2/CO_2 (10/90), c) C_2H_2/CH_4 (50/50), d) C_2H_2/CH_4 (10/90), e) C_3H_6/C_3H_8 (50/50) and f) C_3H_6/C_3H_8 (90/10).

Kinetic studies

To further investigate how for the **[M(H₂mdp)(Ni(CN)₄)]** HUMs could be used to separate gas pairs, kinetic studies were carried out for the C_3 gas pairings using both due to their fast uptake kinetics. Kinetic experiments are useful as they allow an understanding of the rate of the adsorption process and how long it takes the gas to achieve equilibrium. This gives an indication of whether separation of gases could be achieved using a fast-cycling approach as a work-around for the smaller uptake capacity of the **[M(H₂mdp)(Ni(CN)₄)]** materials. Beginning with **[Co(H₂mdp)(Ni(CN)₄)]**, for both C_3H_6 and C_3H_8 equilibrium was achieved at *ca.* 30 seconds. The kinetic profile of **[Fe(H₂mdp)(Ni(CN)₄)]** was different for the two gases. For C_3H_6, equilibrium was achieved by around 15 seconds, with C_3H_8 showing a more laboured uptake, with equilibrium achieved much later between 35 and 80 seconds, (Fig. S83). These results indicate that these materials, in particular **[Fe(H₂mdp)(Ni(CN)₄)]**, are kinetically selective for C_3H_6 over C_3H_8.

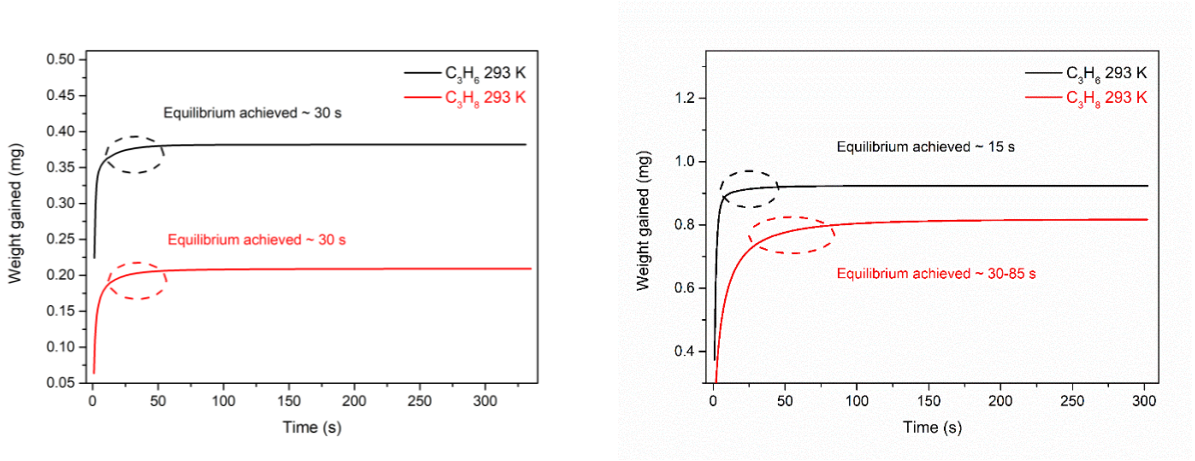

Figure S83. Kinetic profiles of C_3H_6 and C_3H_8 adsorption for **[Co(H₂mdp)(Ni(CN)₄)]** (left) and **[Fe(H₂mdp)(Ni(CN)₄)]** (right).

Different diffusional models can be utilized to further investigate the adsorption kinetics of gases. We used Fick's law to estimate diffusion in these MOFs. Fick's law for isothermal diffusion into a homogeneous spherical particle is described by the following equation:

$$\frac{m_t}{m_e} = 1 - \frac{6}{\pi^2}\sum_{n=1}^{\infty}\frac{1}{n^2}\,exp\left(-\frac{n^2\pi^2 Dt}{r^2}\right) \qquad s5$$

Where m_t is mass uptake at each time, m_e is mass uptake at equilibrium, r is the particle radius and D is the diffusion coefficient.

In the long-time region ($m_t/m_e > 0.7$), where the fractional uptake approaches equilibrium, Eq. S5 converges to:[13]

$$\frac{m_t}{m_e} \approx 1 - \frac{6}{\pi^2} exp\left(-\frac{\pi^2 Dt}{r^2}\right) \qquad s6$$

So, only data points with $(\frac{m_t}{m_e})$ greater than 70% and less than 99% were employed for estimating the diffusion time constants. The kinetic selectivity for the adsorption of propene over propane by a solid can be defined as the ratio of the two gases' diffusional time constants' (given by D/r^2).[14]

Table S2 Kinetic Selectivities for the Uptake of Propene over Propane in the MOFs, Expressed as the ratio of the two Relevant Diffusion Time Constants (D/r^2).

Material	gas	D/r^2 (s^{-1})	R^2	Kinetic selectivity
[Co(H_2mdp)(Ni(CN)$_4$)]	C_3H_6	1.53e-02	0.87	1.51
	C_3H_8	1.01e-02	0.92	
[Fe(H_2mdp)(Ni(CN)$_4$)]	C_3H_6	2.91e-02	0.91	4.95
	C_3H_8	5.88e-03	0.98	

Table S3 Computationally derived static binding energy of the gases with the MOF structures in kJ/mol.

Binding energy (kJ/mol)	**[Co(H_2mdp)(Ni(CN)$_4$)]**	**[Fe(H_2mdp)(Ni(CN)$_4$)]**
CO_2	-32.50	-35.47
C_2H_2	-45.41	-47.89
C_2H_4	-44.07	-44.71
C_2H_6	-42.79	-44.67
C_3H_6	-57.00 (-47.87)	-59.05(-50.89)
C_3H_8	-59.61 (-42.81)	-64.70 (-47.62)

Table S4 Comparison of uptake capacity, C_2H_2 heat of adsorption and C_2H_2/CO_2 and C_2H_2/CH_4 selectivity values of **[Co(H_2mdp)(Ni(CN)$_4$)]** and **[Fe(H_2mdp)(Ni(CN)$_4$)]** with other top performing sorbents at 298 K and 1 bar.

Adsorbent	C_2H_2 uptake @ 1 bar (mmol g^{-1})	Q_{st} C_2H_2 @ zero loading (kJ mol^{-1})	IAST selectivity C_2H_2/CO_2 (1:1)	IAST selectivity C_2H_2/CH_4 (1:1)	References
FJU-83a	5.5[a]	26.9	2.9	24	15
SNNU-328	1.5	37.1	-	16	16
UTSA-85a	3.1[b]	26	4	19	17
ZJU-198	3.3	26.1	-	391.1	18
Cu-TDPAH	7.9	42.5		127.1	19
ZJU-74a	3.8	45	36.5	1313	20
Cu(bpy)NP	2.3	40.8	47.2	-	21
FeNi-M'MOF	4.3	33.4	24	199	22, 23
PCM-48	1.1	23.6	4.3	23.3	24
$[Cu_3(fbptc)_2]$	5.3	27.2	3.6	14.4	25
ZJU-195a	9.6	29.9	4.7	43.4	26
$[Co_2(F\text{-}PyIP)_2]$	2.8	33	6.3	65.9	27
MUF-17	3.1[c]	49.5	6	-	28
HOF-3a	2.1	19.5	21.5	-	29
HOF-16a	2.7	23	-	107	30
TIFSIX-2-Cu-i	4.1	46.3	10.7	24	31
NKMOF-1-Ni	2.7	60.3	22	6409	32
[Co(H_2mdp)(Ni(CN)$_4$)]	**1.2[c]**	**40.5**	**5**	**19.7**	**This work**
[Fe(H_2mdp)(Ni(CN)$_4$)]	**1.1[c]**	**40**	**5.3**	**37.6**	**This work**

[a] Recorded at 273 K

[b] Recorded at 296 K

[c] Recorded at 293 K

References

1. P. E. Kruger, B. Moubaraki, G. D. Fallon and K. S. Murray, *J. Chem. Soc., Dalton Trans.*, 2000, 713.
2. G. M. Sheldrick, *Acta Cryst. A71* **2015**, 3–8.
3. G. M. Sheldrick, *Acta Cryst. C71* **2015**, 3–8.
4. O. V Dolomanov, L. J. Bourhis, R. J. Gildea, J. A. K. Howard, H. Puschmann, *J. Appl. Cryst.* **2009**, 42, 339–341.
5. C. F. Macrae, I. Sovago, S. J. Cottrell, P. T. A. Galek, P. McCabe, E. Pidcock, M. Platings, G. P. Shields, J. S. Stevens, M. Towler and P. A. Wood, *J. Appl. Cryst.*, **53**, 226-235, 2020
6. A. L. Myers and J. M. Prausnitz, *AIChE J.*, 1965, **11**, 121–127
7. BIOVIA, Dassault Systèmes, Material Studio, San Diego: Dassault Systèmes, **2019**.
8. A.K. Rappe, C.J. Casewit, K.S. Colwell, W.A. Goddard, W.M. Skiff, *J. Am. Chem. Soc.*, **1992**, *114*, 10024-10035.
9. G. Kresse, J. Hafner, *Phys. Rev. B,* **1993**, *48*, 13115-13118.
10. S. Grimme, S. Ehrlich, L. Goerigk, *J. Comp. Chem.,* **2011**, *32*, 1456-1465.
11. J.P. Perdew, K. Burke, M. Ernzerhof, *Phys. Rev. Lett.,* **1996**, *77*, 3865-3868.
12. G. Kresse, D. Joubert, *Phys. Rev. B*, **1999**, *59*, 1758-1775.
13. Åhlén, M.; Kapaca, E.; Hedbom, D.; Willhammar, T.; Strømme, M.; Cheung, O., *Microporous Mesoporous Mater.* **2022**, *329*, 111548.
14. Lee, C. Y.; Bae, Y.-S.; Jeong, N. C.; Farha, O. K.; Sarjeant, A. A.; Stern, C. L.; Nickias, P.; Snurr, R. Q.; Hupp, J. T.; Nguyen, S. T., *J. Am. Chem. Soc.* **2011**, *133 (14),* 5228-5231.
15. X. B. Xu, Y. Yang, Z. Yuan, F. Zheng, F. Xiang, Z. Bao, Z. Zhang and S. Xiang, Sep. Purif. Technol., 2023, **325**, 124654.
16. J. Lei, W. Yuan, J. Shang, J. Xu, P. Zhang, Y. Wang, Y.-P. Li and Q. -G. Zhai, *Inorg. Chem.* 2023, **62**, 37, 15195–15205.
17. O. Alduhaish, H. Wang, B. Li, H. D. Arman, V. Nesterov, K. Alfooty and B. Chen, *ChemPlusChem*, 2016, **81**, 764.
18. L. Zhang, X. L. Cui, H. B. Xing, Y. Yang, Y. J. Cui, B. L. Chen and G. D. Qian, *RSC Adv.*, 2017, **7**, 20795–20800.
19. K. Liu, D. Ma, B. Li, Y. Li, K. Yao, Z. Zhang, Y. Han and Z. Shi, *J. Mater. Chem. A*, 2014, **2**, 15823.
20. J. Pei, K. Shao, J. X. Wang, H. M. Wen, Y. Yang, Y. Cui, R. Krishna, B. Li and G. Qian, *Adv. Mater.*, 2020, **32**, 1908275.
21. Y. Liu, J. Liu, H. Xiong, J. Chen, S. Chen, Z. Zeng, S. Deng and J. Wang, *Nat. Commun.*, 2022, **13**, 5515.
22. J. Gao, X. Qian, R.-B. Lin, R. Krishna, H. Wu, W. Zhou and B. Chen, *Angew. Chem., Int. Ed.*, 2020, **59**, 4396–4400.

23. Y. Zheng, J. Yong, Z. Zhi, J. Chen, Z. Song and J. Gao, *J. Solid State Chem.* 2021, **304,** 122554.

24. J. E. Reynolds III, K. M. Walsh, B. Li, P. Kunal, B. Chen and S. M. Humphrey, *Chem. Commun.*, 2018, **54**, 9937–9940.

25. R. H. Su, W. J. Shi, X. Y. Zhang, L. Hou and Y. Y. Wang, *Inorg. Chem.*, 2023, **62**, 11869–11875.

26. L. Zhang, K. Jiang, Y. P. Li, D. Zhao, Y. Yang, Y. J. Cui, B. Chen and G. D. Qian, *Cryst. Growth Des.*, 2017, **17**, 2319–2322.

27. X.-Y. Zhang, W.-J. Shi, G.-D. Wang, L. Hou and Y.-Y. Wang, *Inorg. Chem.* 2023, **62**, 40, 16574–16581.

28. O. T. Qazvini, R. Babarao and S. G. Telfer, *Chem. Mater.*, 2019, **31**, 4919–4926.

29. P. Li, Y. He, Y. Zhao, L. Weng, H. Wang, R. Krishna, H. Wu, W. Zhou, M. O'Keeffe, Y. Han and B. Chen, *Angew. Chem., Int. Ed.*, 2014, **54**, 574–577.

30. Y. Cai, H. Chen, P. Liu, J. Chen, H. Xu, T. Alshahrani, L. Li, B. Chen and J. Gao, *Microporous Mesoporous Mater.* 2023, **352**, 112495.

31. K.-J. Chen, H. S. Scott, D. G. Madden, T. Pham, A. Kumar, A. Bajpai, M. Lusi, K. A. Forrest, B. Space, J. J. Perry and M. J. Zaworotko, *Chem*, 2016, **1**, 753–765.

32. Y.-L. Peng, T. Pham, P. Li, T. Wang, Y. Chen, K.-J. Chen, K. A. Forrest, B. Space, P. Cheng, M. J. Zaworotko and Z. Zhang, *Angew. Chem., Int. Ed.,* 2018, **57**, 10971-10975.